Master-thesis

Tuning the physical properties of $La_{0.7}Sr_{0.3}MnO_{3-\delta}$ thin films and powder via oxygen off-stoichiometry

May 2022

In JCNS-2, Forschungszentrum Jülich

By Chenyang Yin from RWTH Aachen

Supervised by

Prof. Dr. Thomas Brückel

Prof. Dr. Regina Dittmann

PD Dr. Oleg Petracic

Zusammenfassung

In komplexen Oxiden können ihre physikalischen Eigenschaften, z.B. Kristallstruktur, magnetische und elektrische Transporteigenschaften leicht über die Sauerstoff-Fehlstöchiometrie kontrolliert werden. Diese Möglichkeit ermöglicht verschiedene Anwendungen, z.B. als Memristoren, Gassensoren und Katalysatoren. Daher ist die Untersuchung der Rolle von Sauerstoffleerstellen von entscheidender Bedeutung um so komplexe Oxide letzlich für Anwendungen nutzen zu können. In vorangehenden Arbeiten wurde in $La_{0.7}Sr_{0.3}MnO_{3-\delta}$ (LSMO)-Dünnschichten durch thermisches Tempern im Vakuum eine Sauerstoff-Fehlstöchiometrie eingeführt, wodurch ein topotaktischer Phasenübergang von der ursprünglichen Perowskit (PV)-Phase zur Brownmillerit (BM)-Phase ausgelöst wurde. Die Transformationseffizienz war jedoch sehr begrenzt und schwer zu wiederholen. In dieser Arbeit wurden LSMO-Dünnschichten durch „High Oxygen Pressure Sputter Deposition" hergestellt. Aluminium wurde als Sauerstoff-Getter verwendet, um einen effizienten und leicht wiederholbaren PV-BM-Phasenübergang zu realisieren. Der erfolgreiche PV-BM-Übergang ist durch Röntgenbeugung (XRD) bestätigt. Dies erhöht die Möglichkeit zukünftiger Studien, z.B. In-Operando-Neutronenbeugung. Zusätzlich wird die Umwandlung der PV-Phase in eine Zwischenphase durch XRD klar demonstriert. Darüber hinaus werden Antiferromagnetismus und gleichzeitig elektrisch isolierendes Verhalten gefunden, wenn sich der LSMO-Film in einer „expandierten Perowskit-Phase" (E-PV) befindet. Röntgenabsorptionsspektroskopie deutet auf die Annahme hin, dass die unterschiedlichen Néel-Temperaturen von der 200-nm-Mischzustandsschicht und der 40-nm-E-PV-Schicht mit unterschiedlichen Mn-Oxidationszuständen zusammenhängen. Überraschenderweise impliziert die SQUID-Magnetometrie, dass die erhaltenen BM-LSMO-Schichten eine neuartige magnetische Struktur aufweisen. Neutronenbeugung wurde daher benutzt um die Spinstruktur einer 200 nm dicken BM-LSMO-Schicht zu untersuchen. Es konnten jedoch keine magnetischen Bragg-Peaks beobachtet werden. Um den Einfluss der durch das Substrat induzierten Verspannung zu untersuchen, wird in einem zweiten Teil meiner Arbeit bulk-ähnliches LSMO-Pulver durch Kugelmahlen hergestellt und hinsichtlich seiner strukturellen und magnetischen Eigenschaften

untersucht. Al-unterstütztes Vakuumglühen löste auch im Pulversystem erfolgreich den PV-BM-Phasenübergang aus. Das BM-LSMO-Pulver zeigt ein typisches antiferromagnetisches Verhalten, das sich von dem des verspannten Dünnschichtsystems unterscheidet. In einem dritten Teil wurde „Ionic Liquid Gating" (ILG) mit einer selbst entworfenen Reaktionszelle eingesetzt, um den PV-BM-Phasenübergang effizienter auszulösen. Es zeigt sich eine kontinuierliche strukturelle Veränderung aber auch eine Filmzersetzung. Darüber hinaus wurde für ILG-behandelte Filme ein Übergang von ferromagnetischem zu antiferromagnetischem Verhalten gezeigt.

Abstract

In complex oxides its physical properties e.g. crystal structure, magnetic and electric transport properties can easily be tuned via the oxygen off-stoichiometry. This possibility enables various applications, e.g. as memristors, gas sensors, and catalysts. Hence, the study of the role of oxygen vacancies is of vital importance to be able to utilize complex oxides for applications. In previous studies, an oxygen off-stoichiometry was introduced in $La_{0.7}Sr_{0.3}MnO_{3-\delta}$ (LSMO) thin films via vacuum thermal annealing thus triggering a topotactic phase transition from the original perovskite (PV) phase to the brownmillerite (BM) phase. However, the transition efficiency was very limited and hard to repeat. In this thesis, LSMO thin films are prepared by High Oxygen Pressure Sputter Deposition. Aluminum is employed as an oxygen getter to realize an efficient and easily repeatable PV-BM phase transition. The successful PV-BM transition is confirmed by X-ray Diffraction (XRD). This greatly increases the possibility of future studies involving e.g. in-operando neutron diffraction. Additionally, the transformation of the PV phase to an intermediate phase is clearly demonstrated via XRD. Moreover, antiferromagnetism and at the same time electrically insulating behavior are found when the LSMO film is in an "expanded perovskite phase" (E-PV). X-ray Absorption Spectroscopy hints toward the assumption that the different Néel-temperatures of 200nm mixed state film and 40nm E-PV film are related to different Mn oxidation states. Surprisingly, SQUID magnetometry implies that the obtained BM-LSMO films exhibit a novel magnetic structure. Neutron diffraction was thus attempted to probe the spin structure of a 200nm thick BM-LSMO film. However, magnetic peaks could not be observed. To study the influence of strain induced by substrate, bulk-like LSMO powder is produced by ball milling and investigated regarding its structural and magnetic properties as a second part of my thesis. Al-assisted vacuum annealing triggered also in the powder system successfully the PV-BM phase transition. The BM-LSMO powder exhibits typical antiferromagnetic behavior which differs from that of the strained thin film system. In a third part, Ionic Liquid Gating (ILG) with a self-designed reaction cell is employed to trigger the PV-BM phase transition more efficiently. However, a continuous structural variation and also a film decomposition are evidenced. Moreover, a ferromagnetic to antiferromagnetic transition is demonstrated for ILG treated films.

Content

1. Introduction

In complex oxides, oxygen vacancies are of huge importance in determining the physical properties. The ability to control these properties enables various applications. E.g. in the field of memristors the migration and diffusion of oxygen vacancies provide a resistive switching mechanism [1]. Moreover, oxygen vacancies can enhance the charge transfer as well as introduce sites for adsorption and surface reactions, thus facilitating applications such as gas sensors, energy storage systems, and catalysts [2,3,4]. Furthermore, the crucial role of oxygen vacancies for oxygen transport in solid fuel cell electrolytes and electrodes has been demonstrated [5,6]. Especially, in a multivalent system e.g. with transition metal ions, the oxidation state of the metal ions can be tuned via an oxygen off-stoichiometry in the crystal lattice thus resulting in changes of several other physical properties e.g. electronic transport and magnetic properties [7,8,9]. Hence, the study of oxygen off-stoichiometry by the generation of oxygen vacancies via a post-treatment has attracted great interest. Possible routes are thermal vacuum annealing [10,11,12], voltage control [13], Ionic Liquid Gating (ILG) [14].

The perovskite type system $La_{1-x}Sr_xMnO_3$ (LSMO) displays sponge-like behavior upon oxygen unloading and loading and thus can be employed to study the coupling between oxygen vacancies and physical properties. In the work of Dr. Lei Cao and Hengbo Zhang, oxygen vacancies have been demonstrated to induce a topotactic phase transition of LSMO film from the initial perovskite phase (PV) to the layered oxygen vacancy ordered brownmillerite (BM) phase via post vacuum annealing. This transition is accompanied by a switching from ferromagnetic (FM) to antiferromagnetic (AFM) and from metallic (M) to insulating (I) behavior [10,11,12]. However, the annealing requires either high temperatures i.e 750°C, or long annealing times, i.e. 62h. This limits further in-situ studies e.g. in-situ neutron diffraction. Moreover, the spin structure of the final BM-LSMO film is unclear and left as an open question.

In this thesis, $La_{0.7}Sr_{0.3}MnO_{3-\delta}$ films were prepared by High Oxygen Pressure Sputter Deposition. This stoichiometry is chosen due to its room temperature ferromagnetic and metallic behavior and its relatively large Curie temperature of 365K. The δ represents the potential deviation of oxygen stoichiometry during sample growth or after post-treatment.

Assisted thermal vacuum annealing employing Aluminum as an oxygen getter is used to realize a fast and easily controllable PV-BM phase transition on LSMO thin films with two different thickness i.e. 40nm and 200nm. The successful phase transition at improved annealing conditions is confirmed by X-ray diffraction. I.e. the PV to BM transition could be achieved at 400-450°C after 12h annealing.

Films after annealing show a reduction of the Mn oxidation state. This leads to antiferromagnetism and an insulating behavior. However, a hint for a potentially novel magnetic structure of the final BM phase in LSMO films is found via SQUID magnetometry. In addition, neutron diffraction was employed to investigate the spin structure of BM-LSMO film, but only nuclear peaks could be observed.

To study the influence of substrate-induced strain onto the PV-BM phase transition, an old LSMO target with the same stoichiometry is used to prepare strain-free bulk-like powder via ball milling. We demonstrate that the powder system can be successfully transformed by Al-assisted vacuum annealing from PV phase via an intermediate phase to the antiferromagnetic BM phase.

Additionally, ILG was reported to exhibit a good efficiency on tuning the physical properties of LSMO films, e.g. electric conduction switching [14,15]. In particular, a triple-state phase transformation between PV, BM and a hydrogenated brownmillerite was demonstrated via ILG on $SrCoO_{3-\delta}$ films [16]. This implies that the PV-BM phase transition of LSMO film can be triggered by ILG. Previously, ILG was investigated on LSMO films grown on insulating $SrTiO_3$ substrates. However, ILG is terminated by a self-passivation effect. In this thesis, the conductive Nb doped $SrTiO_3$ is employed as substrate and a continuous structural transformation can thus be triggered. Moreover, a ferromagnetic to antiferromagnetic phase transition is realized.

Iron oxides also show a topotactic relation between magnetite (Fe_3O_4), wüstite ($Fe_{1-x}O$), and maghemite ($\gamma - Fe_2O_3$). This relation provides a hint that they also can be topotactic transformed after preparation similar to the LSMO PV-BM system. In this thesis, as a side study, magnetite Fe_3O_4 thin film samples are grown by Pulsed Laser Deposition by another Master

student, Yifan Xu. ILG with different voltage polarities has been used to alter the physical properties of Fe_3O_4 films.

Outline of this thesis

The theoretical background is introduced in **Chapter 2**. First, the lattice structure of perovskites as well as transition metal oxides is described. Then, the basics of magnetism in transition metal oxides is highlighted. Considering the sample preparation and structural characterization, typical thin film growth methods as well as the scattering theory is shortly discussed. In **Chapter 3** the corresponding experimental methods and instruments are shown. **Chapter 4** focuses on the LSMO thin film growth parameter investigation and optimization. The topotactic phase transition triggered by Al-assisted vacuum annealing based on the LSMO thin film and powder samples is presented in **Chapter 5**. The ionic liquid gating method for LSMO and Fe_3O_4 thin film samples are explained in **Chapter 6**.

2. Theoretical Background

In this chapter, the theoretical background involved in this thesis is discussed. First, the perovskite structure and its derivatives (e.g. brownmillerite) are introduced, followed by a description of transition metal oxides e.g. LSMO and iron oxides. Then the magnetism of transition metal oxides is discussed, in particular crystal field splitting and exchange interactions. Finally, thin-film growth methods as well as the scattering theory for X-rays and neutrons are described.

2.1 Perovskite structure and its derivatives

The perovskite is a mineral with the formula of $CaTiO_3$, which was found in the 19th century by the Prussian mineralogist Gustav Rose and named after the mineralogist Count Lev Aleksvich von Petrovski [17]. The name "perovskite" is adopted by the compounds which exhibit or are close to the chemical stichometry ABX_3. Due to the flexible possible substitutions at the A- and B-sites and their rich physical properties, perovskites are intensively studied. Here, the basic ABO_3 structure as well as the anion/cation-deficient derivatives are introduced. Among these derivatives in particular the brownmillerite structure is highlighted.

2.1.1 ABO₃ Perovskites

In 1940s, with the discovery of ferroelectric properties of $BaTiO_3$ the importance of perovskites become evident. It triggered intense research interests in the structure-property relationship of overall compositions ABO_3. Typically, the idealized cubic ABO_3 perovskite structure with space group $Pm\bar{3}m$ is adopted, as an example by $SrTiO_3$ at room temperature. When assuming perovskites to be ionic compounds, the eight corners of the unit cell (A-site) are occupied by alkaline earth metal cations (here Sr^{2+} ions) or rare earth cations with large ionic radii. Having a medium-size radius, transition metal cations (here Ti^{4+} ions) are located at the center of the unit cell (B-site) and coordinated by a regular $6O^{2-}$ octahedron, illustrated in **Figure 2.1(a)**. In addition, the unit cell can be depicted in such a way to show the coordination of Sr^{2+} ions. The $12O^{2-}$ cuboctahedral cage around Sr^{2+} ions are shown in **Figure 2.1(b)**.
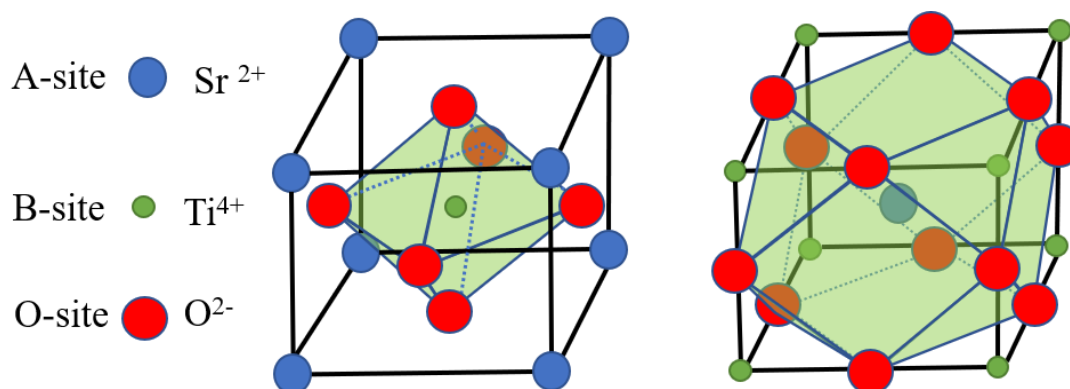
Figure 2.1 Crystal structure of $SrTiO_3$. (a) TiO_6 octahedron, with Ti at the unit cell center. (b) SrO_{12} cuboctahedral cage, with Sr at the unit cell center.

2.1.2 Anion/Cation-deficient derivatives

For ABO_3 perovskites, the O^{2-} ions can partially or fully be substituted by other anions thus forming e.g. nitrides ($ThTaN_3$), oxynitrides ($NdTiO_2N$) and oxyfluorides ($SrFeO_2F$). An oxygen off-stoichiometry can lead to anion deficient derivatives, e.g. brownmillerite ($A_2B_2O_5$ or $ABO_{2.5}$). The mineral brownmillerite with an approximate chemical composition $Ca_2(Al, Fe)_2O_5$ was found in 1932. The brownmillerite structure can be described as an oxygen deficient perovskite with alternating stacking sheets of corner-linked oxygen tetrahedra (T) and octahedra (O) (OTOT stacking shown in **Figure 2.2(c)**). For each alternating sheet of BO_6 octahedra of the original perovskite structure, rows of oxygen vacancies are then formed in the

[110] direction, shown in **Figure 2.2(b)**, introducing equivalently a loss of two O^{2-} anions for each octahedron, thus resulting in apex-linked chains of BO_4 tetrahedra alone the [110] direction. Consequently, the original perovskite structure can be transformed to brownmillerite by a deoxygenating topotactic phase transition.
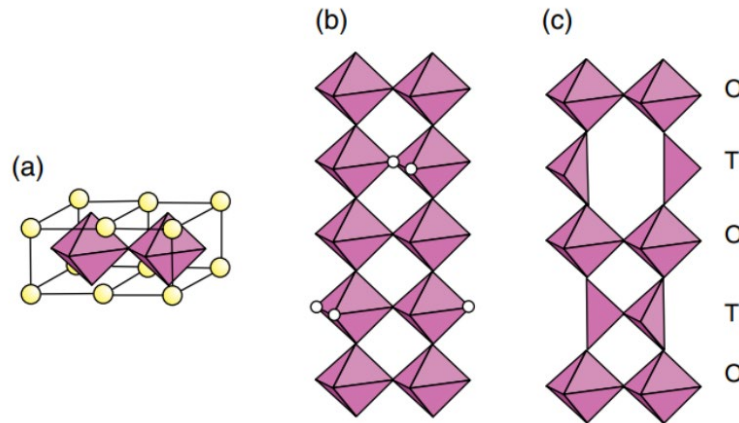
Figure 2.2 The crystal structure of $ABO_{2.5}$ brownmillerite, figure taken from [17]. (a) The original perovskite structure. (b) Oxygen vacancies (white circles) are formed along the [110] direction. (c) The brownmillerite structure with alternating oxygen octahedra (O) and tetrahedra (T).

Furthermore, the A-site cations of perovskites can also be deficient in many cases, leading to higher oxidation states of the B-site cations. When all B-site cations exhibit an oxidation state of +6, the A-site is left empty and turning the structure to an apex-sharing array of octahedra e.g. ReO_3.

2.2 Transition metal oxides

Complex oxides have been intensively investigated due to their rich physical properties with a multitude of existing and potential applications. Among complex oxides, transition metal oxides with a multivalent magnetic element (e.g. Mn, Fe) show unique electronic, magnetic, and spintronic properties. This enables various functionalities in many fields [18, 19, 20].

Recently, the multivalent transition metal oxide $La_{1-x}Sr_xMnO_3$ (LSMO), an ABO_3 type perovskite, has attracted intense attention due to its tunable physical properties by various Sr doping concentrations. When tuning the Mn oxidation state via Sr doping, LSMO can show various magnetic ordering phenomena, in particular ferromagnetic (FM) and antiferromagnetic

(AFM) ordering (**Figure 2.3 (a)**). In **Figure 2.3 (b)**, the phase diagram is depicted for various Sr doping [21]. When zero doped, i.e. for $LaMnO_3$ one finds A-type AFM spin ordering at low temperatures accompanied with an insulating behavior. Here, Mn ions only exist in the state Mn^{3+} (octahedral sites, $t_{2g}^3 e_g^1$). Upon increasing the Sr content, the Mn^{3+} is gradually replaced by Mn^{4+} (octahedral sites, $t_{2g}^3 e_g^0$). The La to Sr ratio corresponds to the ratio of Mn^{3+} to Mn^{4+}. In the range of $0.1 < x < 0.5$, a FM phase emerges. For x ca. 0.17, with the vanishing of a Jahn-Teller distortion and the appearing of a rhombohedral structure, the system is transformed from insulating to metallic behavior [21, 22, 23]. For $0.5 < x < 0.6$, the system returns to A-type AFM ordering and behaves metallic at lower temperatures and displays FM and metallic behavior at higher temperatures [24]. With larger Sr doping ($0.7 < x < 0.85$) C-type AFM ordering and insulating behavior emerges [21]. In addition to A-site doping, oxygen can be off-stoichiometric which yields a variable concentration of $V_O^{\cdot\cdot}$ vacancies. This provides a second handle to manipulate the oxidation state of Mn. Besides stoichiometry, strain caused by the substrate in an epitaxial thin film system can also introduce large influences onto the physical properties.
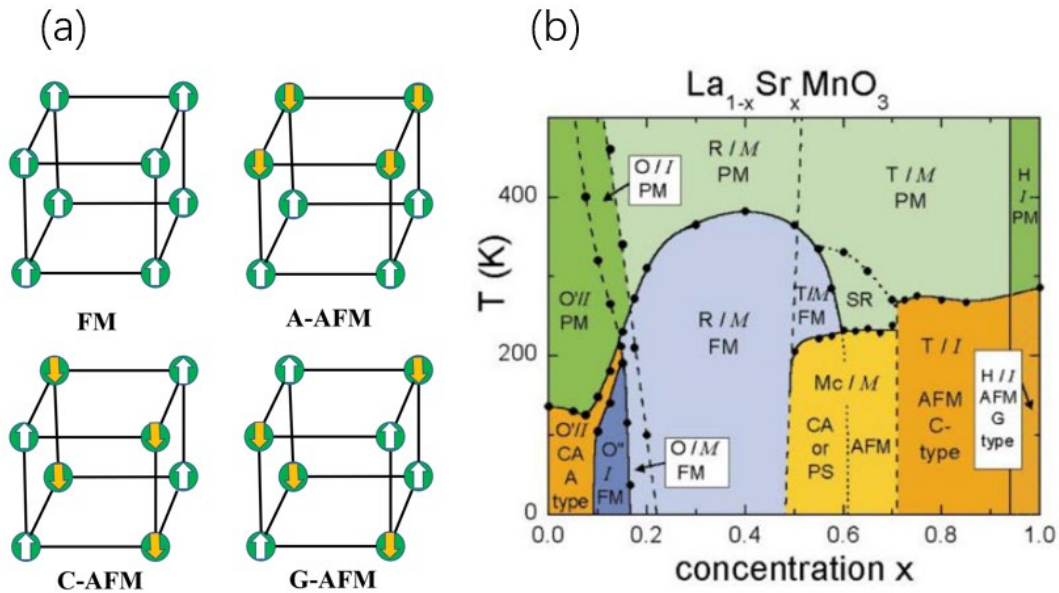
Figure 2.3 (a) Schematic AFM and FM spin ordering types. (b) The phase diagram of $La_{1-x}Sr_xMnO_3$. Symbols O, O', O", R, T, H, and M_C are used to represent orthorhombic, Jahn-Teller distorted orthorhombic, orbital-ordered orthorhombic, rhombohedral, tetragonal, hexagonal, and monoclinic, respectively. Regarding the magnetic and electric transport property the abbreviations mean PA: paramagnetic, FM: ferromagnetic, AFM: antiferromagnetic, M: metallic, and I: insulating. Figure taken from Ref [21].

In this thesis, we choose to study the $La_{0.7}Sr_{0.3}MnO_3$ system ($x = 0.3$). In this stoichiometry, the Mn^{3+} and Mn^{4+} ions coexist at the ratio of 0.7 : 0.3. This system shows a perovskite type rhombohedral structure ($R\bar{3}c$). It is ferromagnetic and metallic at room temperature with a bulk Curie temperature of 365 K. The basic crystal structure of $La_{0.7}Sr_{0.3}MnO_3$ is shown in **Figure 2.4**. The $Mn^{3+/4+}$ ions are located at the center of the unit cell and are surrounded by an oxygen octahedron. The eight corners of the unit cell are occupied by La^{3+}(70%) and Sr^{2+}(30%).
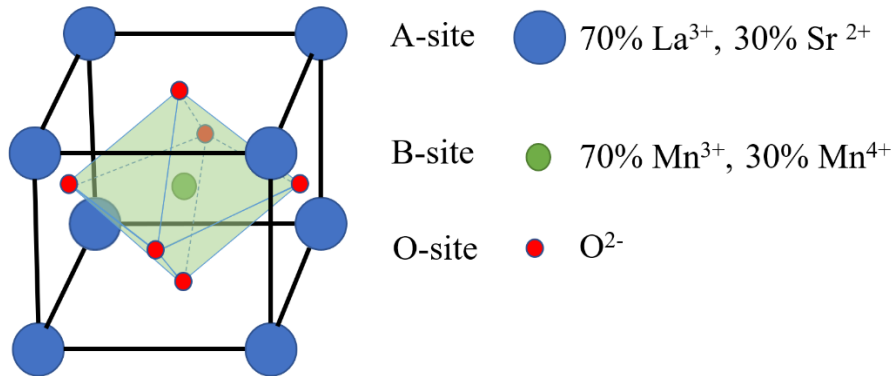
Figure 2.4 Lattice structure of $La_{0.7}Sr_{0.3}MnO_3$. Perovskite type pseudocubic structure with space group $R\bar{3}c$. The A-sites are occupied by lanthanum and strontium. The B, and C sites are occupied by manganese and oxygen, respectively.

Additionally, iron oxides with Fe ion as the magnetic element likewise exhibit tunability regarding their electric and magnetic properties. Magnetite Fe_3O_4 (cubic structure, space group $Fd\bar{3}m$), which is ferrimagnetic and half-metallic, shows high a Curie temperature of 860K as well as a metal-insulator transition (Verwey transition) at 120K. For magnetite, the structure can be described as $[Fe^{3+}]_{T_d}[Fe^{2+}Fe^{3+}]_{O_h}O_4$, shown in **Figure 2.5**. The tetrahedral (T_d) sites are occupied by Fe^{3+}, the octahedral(O_h) sites are shared by Fe^{2+} and Fe^{3+}. Moreover, magnetite can be deoxygenated to antiferromagnetic wüstite $Fe_{1-x}O$ (rocksalt structure, space group Fm3m) phase with Néel temperature at 200K, or oxygenated to ferrimagnetic insulating maghemite $\gamma - Fe_2O_3$ (inverse spinel structure, $Fd\bar{3}m$). Maghemite can be considered as Fe-deficient magnetite with a structure formula of $[Fe^{3+}]_{T_d}\left[\frac{5}{3}Fe^{3+}\frac{1}{3}V_{Fe}\right]_{O_h}O_4$ [25].
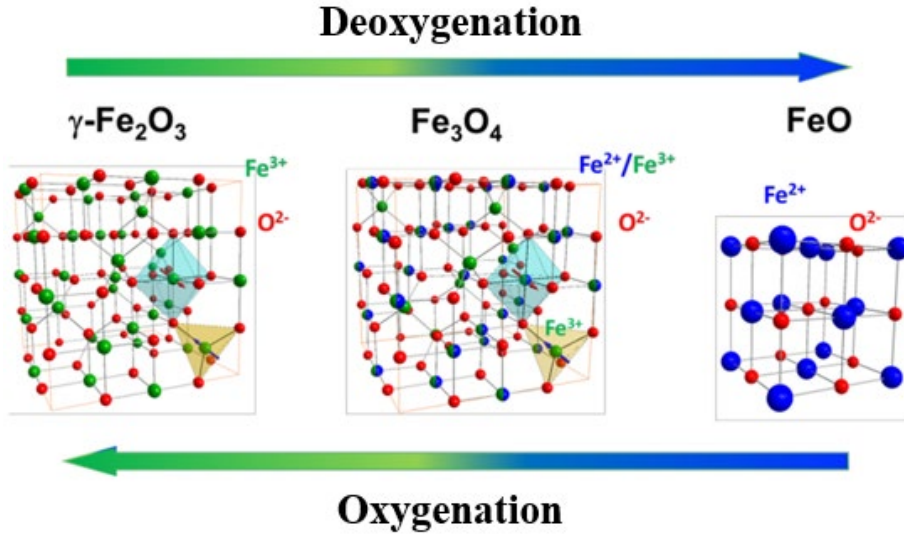
Figure 2.5 Crystal structure of maghemite $\gamma - Fe_2O_3$, magnetite Fe_3O_4 and wüstite $Fe_{1-x}O$. Figure partially taken from Ref [25].

2.3 Magnetism in transition metal oxides

For transition metal oxides, the electronic and magnetic properties are mainly influenced by the d-electrons of the transition metal. In this subsection, firstly the basics of condensed matter magnetism is briefly introduced, then followed by typical interactions. The final part discusses collective behavior. Here ferromagnetism as well as antiferromagnetism is described.

2.3.1 Basics of condensed matter magnetism

In an atom, an orbiting electron introduces an orbital angular momentum $\vec{L}$ [26]. The magnitude $|\vec{L}|$ is described in **Equation 2-1**. L, n and $\hbar$ refer to the orbital quantum number, the principal quantum number and the reduced Planck constant, respectively.

$$\begin{cases} |\vec{L}| = \sqrt{L(L+1)}\hbar \\ L = 0, \dots, n-1 \end{cases} \quad (2-1)$$

In addition, electrons carry an intrinsic spin angular momentum $\vec{S}$, the magnitude is shown in **Equation 2-2**. The S is the spin quantum number. For electrons S equals to $1/2$. The total angular momentum $\vec{J}$ is described in **Equation 2-3**. The J denotes the total angular momentum quantum number and takes values from $|L - S|$ to $|L + S|$ in half-integer steps.

$$\begin{cases} |\vec{S}| = \sqrt{S(S+1)}\hbar \\ S = \dfrac{1}{2} \end{cases} \tag{2-2}$$

$$\begin{cases} \vec{J} = \vec{L} + \vec{S} \\ |\vec{J}| = \sqrt{J(J+1)}\hbar \\ |L-S| \le J \le |L+S| \end{cases} \tag{2-3}$$

The corresponding magnetic moment $\vec{\mu}$ i.e. $\vec{\mu}_L$, $\vec{\mu}_S$ and $\vec{\mu}_J$ follows from its angular momentum and is described in **Equation 2-4**. The g and μ_B refer to the dimensionless g-factor and the Bohr magneton, respectively. The g_L equals to 1. For electrons, the g_S is approximately 2. The g_J is known as the Landé g-value, as shown in **Equation 2-5**. In the following text, the angular momentum is presented in the unit of $\hbar$ for simplicity.

$$\begin{cases} \vec{\mu}_L = -g_L \mu_B \dfrac{\vec{L}}{\hbar} \\ \vec{\mu}_S = -g_S \mu_B \dfrac{\vec{S}}{\hbar} \\ \vec{\mu}_J = -g_J \mu_B \dfrac{\vec{J}}{\hbar} \end{cases} \tag{2-4}$$

$$g_J = \frac{3}{2} + \frac{S(S+1) - L(L+1)}{2J(J+1)} \tag{2-5}$$

When assuming that the magnetic moments are isolated, i.e. no interactions with magnetic moments to other atoms or with the environment, then only the interaction between the isolated moments with the applied magnetic field needs to be considered. This case can be applied to diamagnetism and to paramagnetism. **Equation 2-6** demonstrates the perturbed Hamiltonian $\hat{H}$ of an isolated atom in the magnetic field $\vec{B}$ [26]. The m_e and $\vec{r}_i$ denote the electron mass and the position of ith electron in the atom, respectively. The first term $\hat{H}_0$ refers to the unperturbed case when $\vec{B}$ is not applied, the second term describes the paramagnetic contribution, and the third term describes diamagnetism. Moreover, when the atom exhibits filled electronic shells, the paramagnetic term vanishes since $\vec{L} + g\vec{S} = 0$. The diamagnetic term shows a sum over square values, which implies that diamagnetism is always present.

$$\hat{H} = \hat{H}_0 + \mu_B(\vec{L} + g_S\vec{S}) \cdot \vec{B} + \frac{e^2}{8m_e} \sum_i (\vec{B} \times \vec{r}_i)^2 \tag{2-6}$$

For atoms with unfilled electronic shells, the atomic magnetic moments originate from unpaired

electrons. The orientations of magnetic moments are randomized by thermal fluctuations thus leading to zero net-magnetization in zero applied field. At an external applied magnetic field, the magnetic moments can be aligned and contribute to a net magnetization $\vec{M}$. The net-magnetization can be calculated considering the alignment effect of the external field and the randomization effect via thermal fluctuations described by the Boltzmann distribution. As a result, M depends on the ratio between B and temperature T, which is described in detail by the Brillouin function $B_J(y)$, as illustrated in **Equation 2-7** [26].

$$\frac{M}{M_S} = B_J(y) = \frac{2J+1}{2J} \coth\left(\frac{2J+1}{2J}y\right) - \frac{1}{2J} \coth\frac{y}{2J} \qquad (2-7)$$

The y is $g_J \mu_B J B / k_B T$. The k_B refers to the Boltzmann constant. When $J = \infty$, $B_{J=\infty}(y)$ equals the Langevin function $L(y) = \coth(y) - \frac{1}{y}$, which corresponds a semiclassical treatment, i.e. the orientations of magnetic moments correspond to classical vectorial quantities. When $J = 1/2$, $B_{J=1/2}(y)$ results in $\tanh(y)$.

Hund's rules are employed to determine the ground state configuration of an atom by the following principles: i) maximize S, and thus the Coulomb energy is minimized because electrons with parallel spins are spatially more separated, ii) maximize L, to reduce the Coulomb repulsion by arranging electrons into orbits with the same direction of rotation, iii) set J as $|L - S|$ or $|L + S|$ depending on if the shell is less than or more than half full filled, respectively, in order to reduce the spin-orbital energy. The third principle might not be obeyed due to e.g. the crystal field splitting in transition metal ions.

For transition metal oxides, the direct interaction of magnetic ions (e.g Mn, Fe) with their immediate surroundings is of significant importance. The crystal field theory describes the effect of local crystal environment (crystal field) on the energy levels of an atom. The crystal field is the electric field produced by the neighboring atoms and hence depends on the symmetry of the local environment. In the LSMO system, the field acts onto the Mn ion located at the center of the unit cell by the surrounding oxygen octahedron. The oxygen ions are modelled as negative point charges. Consequently, an energy splitting Δ is induced by the crystal field which depends on the Mn-O distance being ca. 2eV for LSMO [27]. Thus, the originally degenerated 3d orbitals (i.e. free ion in a spherical symmetric environment) split into e_g (d_{z^2}, $d_{x^2-y^2}$) and

t_{2g} (d_{xy}, d_{xz}, d_{yz}) orbitals [26,28]. As shown in **Figure 2.6**, the threefold t_{2g} orbitals lead to a lower overlap with the 2p orbital of oxygen, resulting in a reduced energy. In contrast, the e_g orbitals induce a larger overlap with oxygen 2p orbitals, and thus the energy is increased.

If this energy splitting is larger than the pairing energy, i.e. the coulomb energy needed for placing two electrons into the same orbital, the so-called "strong-field case" allows to first doubly occupy the t_{2g} orbitals leading to a low spin state. Conversely, the "weak-field case" allows electrons to occupy both e_g and t_{2g} orbitals according to Hund's rules resulting in a high spin state. The latter is the case for LSMO.

Moreover, for Mn^{3+} ($3d^4$), the surrounding oxygen octahedron is spontaneously distorted, which shows an elongation along the z-axis, as illustrated in the third column of **Figure 2.6**. This phenomenon is called Jahn-Teller distortion, which further lifts the degeneracy of the e_g and t_{2g} levels [26]. With 4 electrons being placed into these orbitals, the electronic energy is reduced after the distortion, which can not only compensate the increased lattice elastic energy but lead to a net reduction of the total energy as well. For Mn^{4+} ($3d^3$), the 3 electrons are all located in the t_{2g} orbitals with the same spin state. In this case there is no electronic energy difference due to a distortion, but an increase in the total energy attributed to the lattice distortion. Hence, no Jahn- Teller effect occurs. Especially, for 3d transition metal ions, when the crystal field is much stronger than the spin-orbital interaction, Hund's third rule may not apply due to orbital quenching, i.e. $L = 0$.
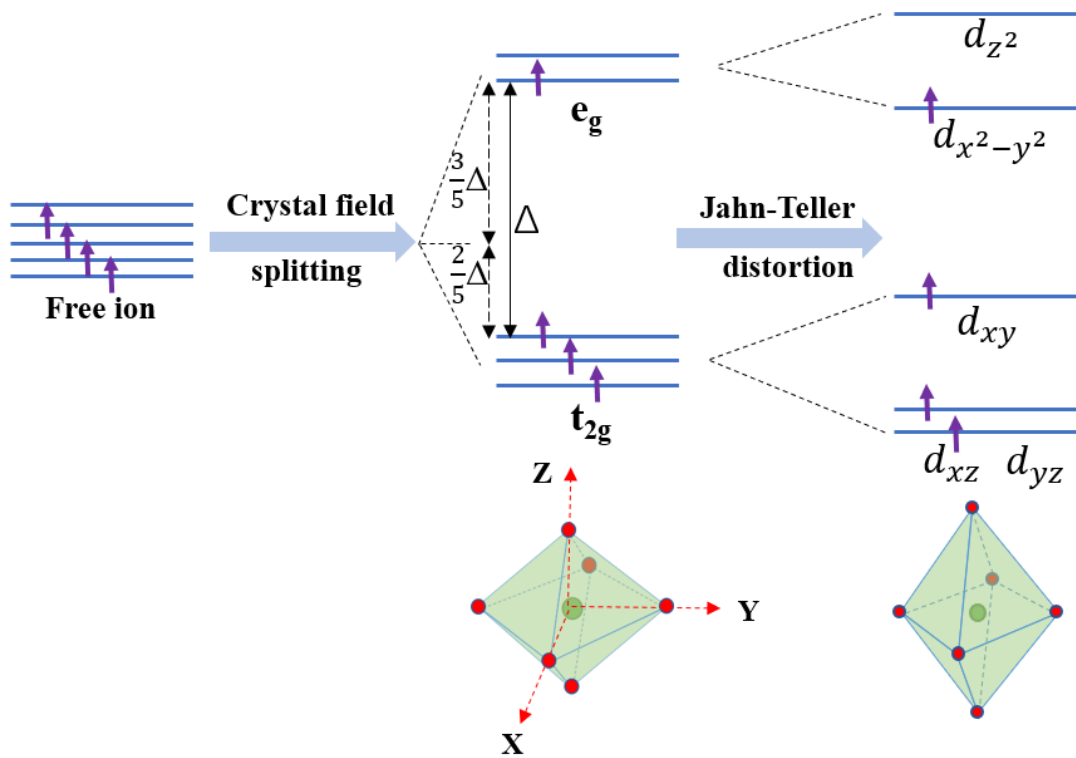
Figure 2.6 Schematical representation of the crystal field splitting and Jahn-Teller distortion of Mn^{3+} ion 3d orbitals. The first column represents the degenerated 3d orbitals of a free ion. The second column demonstrates the crystal field splitting due to the surrounding oxygen octahedron. The third column describes the Jahn-Teller distortion along the z-axis.

For the case of magnetite Fe_3O_4, the structure $[Fe^{3+}]_{T_d}[Fe^{2+}Fe^{3+}]_{O_h}O_4$ as well as the OTOT stacking of the BM-LSMO comprises two coexisting types of oxygen environments, i.e. both octahedral (O_h) and tetrahedral (T_d). For the tetrahedral oxygen environment, the crystal field exhibits an opposite effect compared with the octahedral one, as shown in **Figure 2.7** [25, 26].
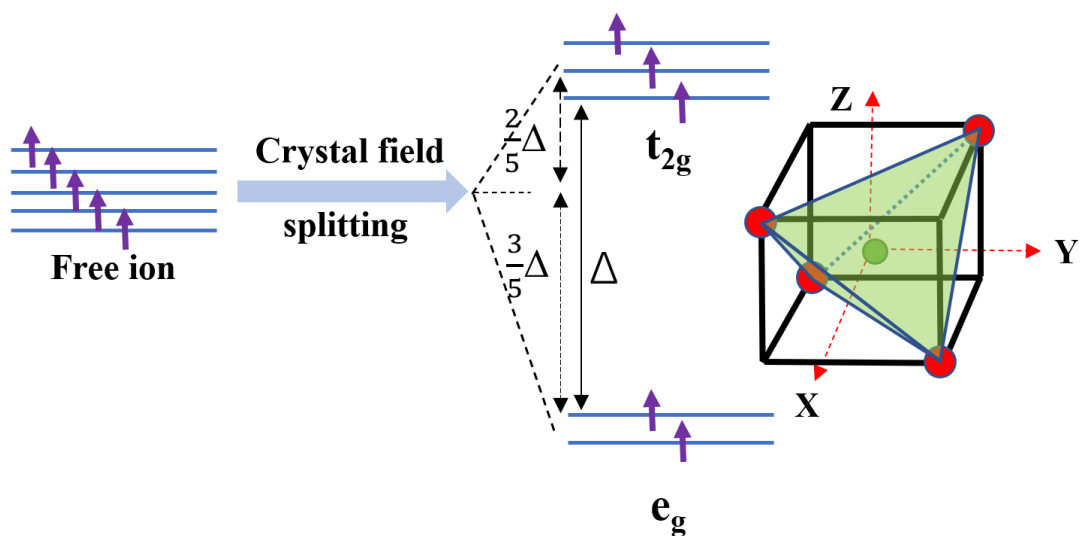

Figure 2.7 Schematical representation of the crystal field splitting of Fe^{3+} 3d orbitals. The first

column represents the degenerated 3d orbitals of a free ion. The second column demonstrates the crystal field splitting due to the surrounding oxygen tetrahedron.

2.3.2 Types of interactions

In solids, long-range magnetic order is a result of interactions between magnetic moments. In this part, magnetic dipolar interactions as well as exchange interactions are introduced.

An atomic magnetic moment can be described as a magnetic dipole analogous to an electric dipole. The energy of interactions between two magnetic moments $\vec{\mu}_1$ and $\vec{\mu}_2$ with a separation $\vec{r}$ is shown in **Equation 2-8** [26]. The μ_0 refers to the permeability of free space. Typical values of the dipolar energy are very weak compared to exchange interactions and can only exhibit an influence at the millikelvin range. However, the overall magnetic domain structure is strongly influenced by the dipolar energy together with the sample geometry.

$$E = \frac{\mu_0}{4\pi r^3}\left[\vec{\mu}_1 \cdot \vec{\mu}_2 - \frac{3}{r^3}(\vec{\mu}_1 \cdot \vec{r})(\vec{\mu}_2 \cdot \vec{r})\right] \qquad (2-8)$$

Exchange interactions play a key role in long range magnetic order. To explain the origin of exchange in a many-body system, the Heisenberg-Hamiltonian (**Equation 2-9**) is introduced. Exchange interactions are considered to exist between all neighboring atoms. The J_{ij} is the exchange integral between the ith and j^{th} spins, i.e. $\vec{S}_i$ and $\vec{S}_j$. When $\vec{S}_i$ and $\vec{S}_j$ belong to the same atom, a triplet state is more energetically favorable due to the reduced Coulomb repulsion. When $\vec{S}_i$ and $\vec{S}_j$ are from different atoms, one can model the overall exchange interaction energy by the Hamiltonian (Heisenberg model):

$$\hat{H} = -\sum_{ij} J_{ij}\vec{S}_i \cdot \vec{S}_j \qquad (2-9)$$

Exchange interactions can be divided into direct exchange and indirect exchange depending on if the exchange needs an intermediary. Direct exchange is relatively rarely encountered due to the insufficient direct magnetic orbital overlap. Contrarily, the indirect exchange, e.g. the superexchange and double-exchange, are more often found.

In transition metal oxides often superexchange interaction is encountered, which is an indirect exchange interaction. The superexchange is defined as the exchange interaction between non-

neighboring magnetic ions at the same oxidation state mediated by a non-magnetic ion, e.g. $Mn^{3+} - O^{2-} - Mn^{3+}$ configuration. Superexchange is derived from second-order perturbation theory and controlled by the hopping exchange integral [26]. When allowing the electrons in the outermost occupied states (oxygen 2p orbitals) to be delocalized to the neighboring Mn^{3+}, the kinetic energy is reduced resulting in an antiferromagnetic configuration. Moreover, this kind of delocalization is called "virtual hopping" and exhibits no net charge transfer. Additionally, the angle of $Mn^{3+} - O^{2-} - Mn^{3+}$ bonds can influence the degree of orbital overlap thus influencing the kinetic exchange term.

For simplicity, the $Mn^{3+} - O^{2-} - Mn^{3+}$ bonds with an angle of $180°$ are assumed. As illustrated in **Figure 2.8,** depending on different delocalization types of the oxygen 2p electrons, the 3d electrons of Mn^{3+} can be either aligned to an antiferromagnetic or to a ferromagnetic configuration via the superexchange interaction. According to the Goodenough–Kanamori–Anderson rules, an antiferromagnetic ordering is energetically preferred when the oxygen 2p electrons delocalize into two half-filled or into two empty Mn 3d orbitals (**Figure 2.8(a)** and **(b)**). However, a ferromagnetic ordering results when the oxygen 2p electrons interact with one half-filled and one unfilled Mn^{3+} 3d orbital (**Figure 2.8 (c)**).

Furthermore, when the Mn ions show different oxidation states, e.g. Mn^{3+} and Mn^{4+}, as shown in **Figure 2.8 (d)**), the hopping of Mn 3d electrons without spin-flip via the oxygen bridges enables an energetically more favorable ferromagnetic spin configuration as well as a metallic behavior i.e. hopping with net charge transfer. In this case, a so-called double-exchange interaction is present.
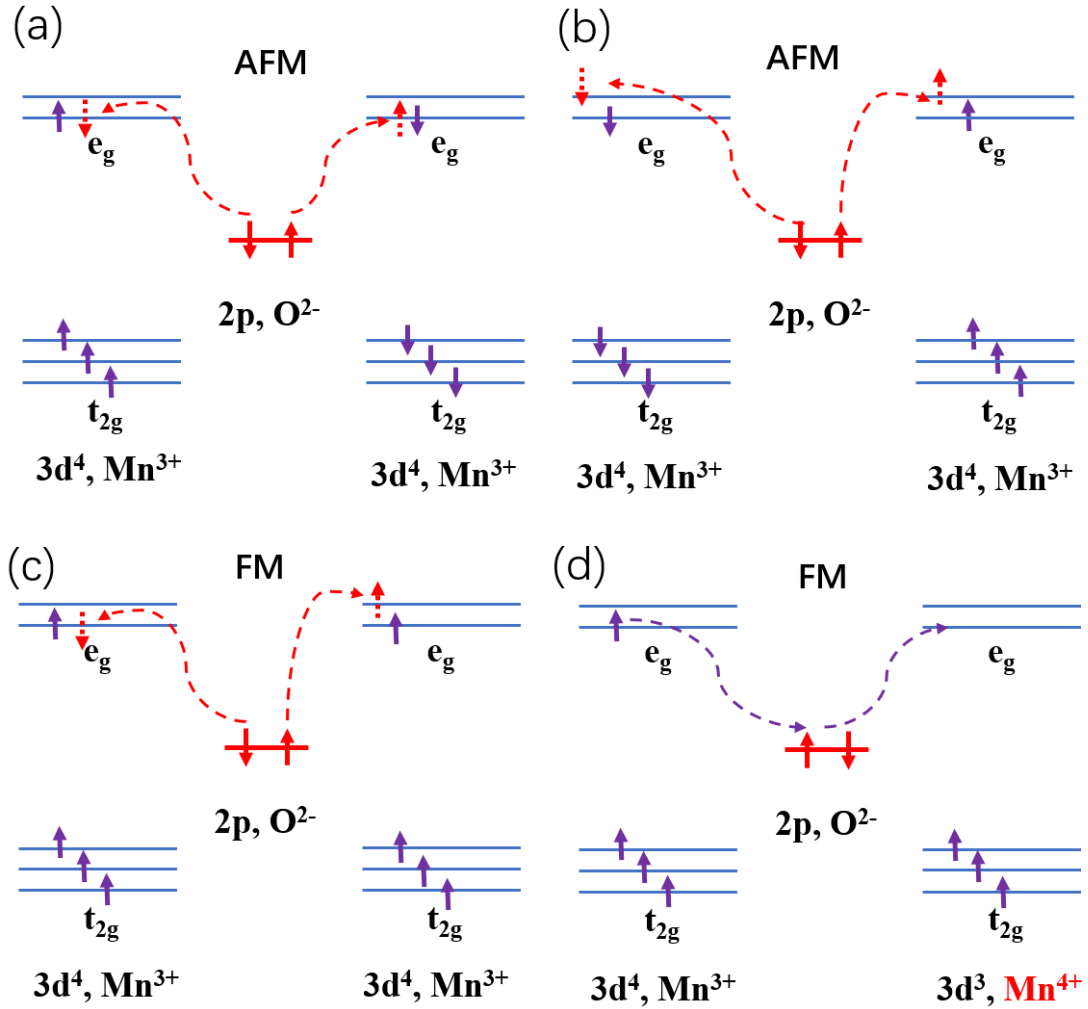
Figure 2.8 Superexchange and double-exchange interactions. (a) Superexchange interaction: antiferromagnetic (AFM) ordering when interacting with two half-filled Mn 3d e_g orbitals. (b) Superexchange interaction: AFM ordering when interacting with two unoccupied 3d e_g orbitals. (c) Superexchange interaction: ferromagnetic (FM) ordering with one half-filled and one empty Mn 3d e_g orbital. (d) Double-exchange interaction: FM ordering when Mn ions show mixed oxidation states.

For magnetite Fe_3O_4, as shown in **Figure 2.9**, the octahedral sites are occupied by both Fe^{2+} and Fe^{3+} ions thus enabling a double-exchange interaction leading to a ferromagnetic coupling. In contrast, the superexchange interaction being effective between the Fe^{3+} ions on tetrahedral and octahedral sites results in an antiferromagnetic spin coupling. Due to the simultaneous action of both double-exchange and superexchange interactions an overall ferrimagnetic behavior is found for magnetite [25].

3d⁶, Fe²⁺ — $3d^6$, Fe^{2+}

3d⁵, Fe³⁺ — $3d^5$, Fe^{3+}

3d⁵, Fe³⁺ — $3d^5$, Fe^{3+}
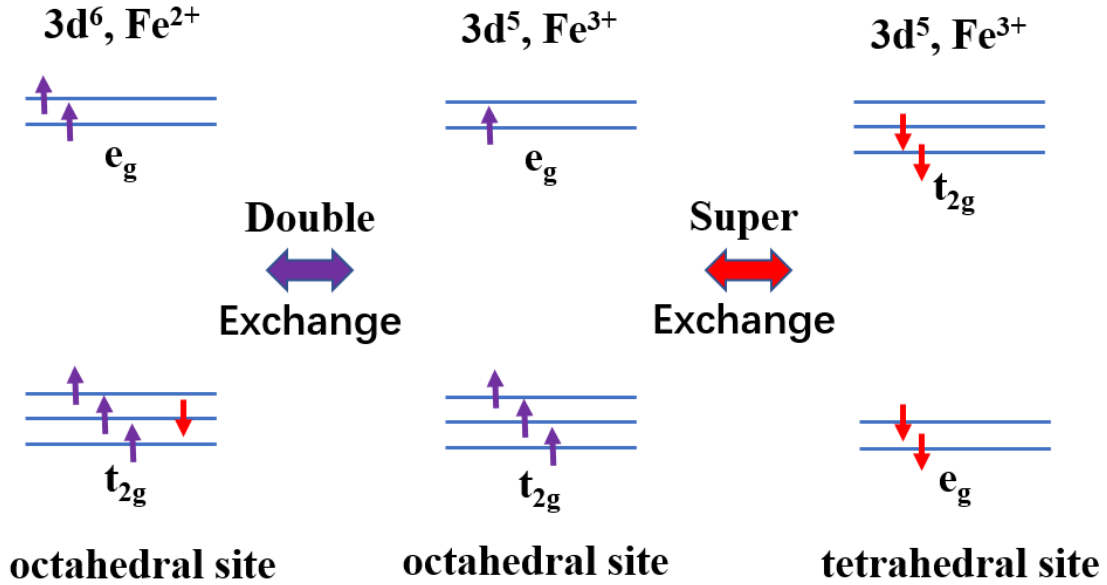
e_g **Double Exchange** e_g **Super Exchange** t_{2g}

t_{2g} t_{2g} e_g

octahedral site   **octahedral site**   **tetrahedral site**

Figure 2.9 Origins of ferrimagnetic behavior of magnetite: superexchange between Fe^{3+} ions on tetrahedral and octahedral sites, and double-exchange between Fe^{2+} and Fe^{3+} ions on octahedral sites.

2.3.3 Types of collective behavior

In this section, the magnetic ground states which are a consequence of the above-mentioned exchange interactions are discussed, e.g. ferromagnets and antiferromagnets. A ferromagnet exhibits a spontaneous magnetization due to a long-range order of magnetic moments. The Hamiltonian can be described by **Equation 2-10** [26]. The first term has previously been introduced in **Equation 2-9**, which is the exchange energy in the framework of the Heisenberg model. The second term refers to the Zeeman energy which originates from the interactions between magnetic moments and the applied magnetic field. The orbital angular momentum is assumed here to be zero for simplicity.

$$\hat{H} = -\sum_{ij} J_{ij} \vec{S}_i \cdot \vec{S}_j + g\mu_B \sum_j \vec{S}_j \cdot \vec{B} \qquad (2-10)$$

In order to model the temperature and field dependence of a ferromagnet the so-called 'mean field model' can be applied. Here, the exchange interaction is approximated by an effective mean field $\vec{B}_{mf}$ produced by the neighboring spins at the ith site (**Equation 2-11**). Moreover, it is assumed that all spins experience the same $\vec{B}_{mf}$. In particular, since $\vec{B}_{mf}$ represents the sum over all exchange interactions it reflects the degree of magnetic ordering of the system.

Hence, for ferromagnets, a linear relationship between $\vec{B}_{mf}$ and the total magnetization $\vec{M}$ with a positive constant λ can be assumed (**Equation 2-12**).

$$\vec{B}_{mf} = -\frac{2}{g\mu_B} \sum_j J_{ij} \vec{S}_j \qquad (2-11)$$

$$\vec{B}_{mf} = \lambda \vec{M} \qquad (2-12)$$

The Heisenberg exchange energy can be described using $\vec{B}_{mf}$ (**Equation 2-13**). Consequently, the Hamiltonian in **Equation 2-10** is rewritten as in **Equation 2-14** which is analogous to the form of a paramagnet, i.e. the second term in **Equation 2-6**. Hence, a ferromagnet can be considered as paramagnet in a modified field $\vec{B} + \vec{B}_{mf}$, as illustrated in **Figure 2.10 (a)**. Thus, the Brillouin function $B_J(y)$ (**Equation 2-7**) can be applied in ferromagnets by replacing $\vec{B}$ with $\vec{B} + \vec{B}_{mf}$. When assuming $B = 0$, i.e. no external field, a non-zero magnetization solution is found when a ferromagnet is below a critical temperature. This is called spontaneous magnetization, and the critical temperature is known as the Curie temperature T_C (**Equation 2-15**).

$$-2\sum_j J_{ij} \vec{S}_i \cdot \vec{S}_j = -g\mu_B \vec{S}_i \cdot \vec{B}_{mf} \qquad (2-13)$$

$$\hat{H} = g\mu_B \sum_i \vec{S}_i \cdot (\vec{B} + \vec{B}_{mf}) \qquad (2-14)$$

$$T_C = \frac{g_J \mu_B (J+1) \lambda M_s}{3k_B} \qquad (2-15)$$

For ferromagnets $J_{ij} > 0$. The case of $J_{ij} < 0$, i.e. negative exchange interaction, favors antiferromagnetism. Similarly, a mean field model can be employed but including two interpenetrating sublattices, which means two kinds of mean fields, as shown in **Figure 2.10 (b)**. Antiferromagnetism disappears when above a transition temperature which is the so-called "Néel-temperature" T_N, shown in **Equation 2-16**.

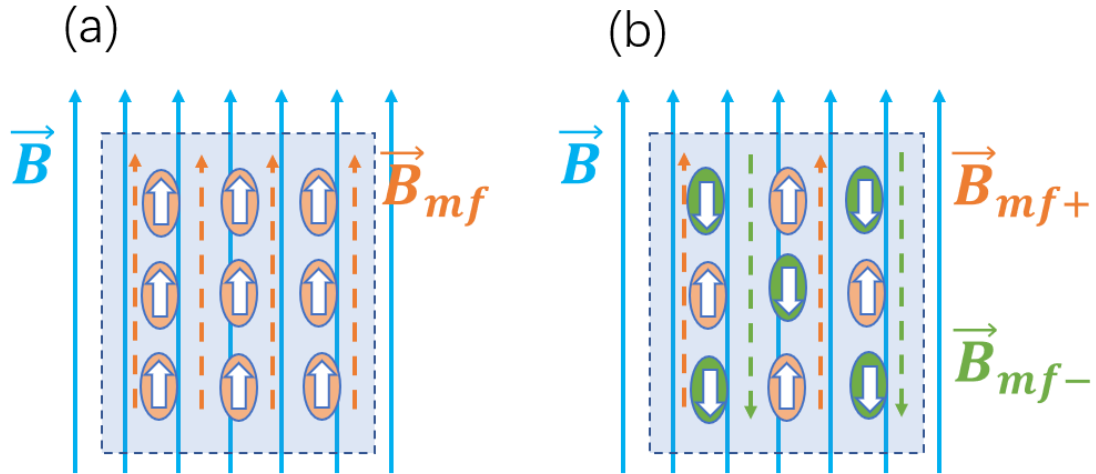$$T_N = \frac{g_J \mu_B (J+1) |\lambda| M_s}{3k_B} \qquad (2-16)$$

Figure 2.10 Schematic of mean fields in ferromagnets and in antiferromagnets. (a) $\vec{B}_{mf}$ produced by the exchange interactions of a ferromagnet.(b) Two kinds of mean fields produced by sublattices in an antiferromagnet, i.e. $\vec{B}_{mf+}$ and $\vec{B}_{mf-}$.

2.4 Thin film growth

2.4.1 CVD&PVD methods

The most often employed methods for thin film growth are presently Chemical Vapor Deposition (CVD) and Physical Vapor Deposition (PVD). In CVD, thin films are grown by chemical reactions of vapor precursors at the surface of the substrate. In PVD, atoms or molecules are evaporated from a condensed phase to a vapor phase and then re-condense back at the substrate surface. Typical evaporation methods are: i) evaporation via thermal or electron beam heating, e.g. in Molecular-Beam Epitaxy (MBE), ii) sputtering by ion bombardment, e.g. in High Oxygen Pressure Sputter Deposition (HOPSD), iii) evaporation by photon bombardment, e.g. in Pulsed Laser Deposition (PLD).

2.4.2 Deposition growth modes

The thin film growth process in PVD can be described as following. Firstly, atoms or molecules are ejected by various methods into the vapor phase. Then they become adsorbed by chemisorption (chemical bonding) or physisorption (e.g. van der Waals bonding) onto the substrate followed by surface diffusion to energetically more favorable sites. Nucleation and

growth can then lead to epitaxial thin films. Depending on the substrate, the thin film growth can be classified into: homoepitaxial growth i.e. the material of the thin film is the same as the material of the substrate or heteroepitaxial growth i.e. the material of thin film and of the substrate are different.

For homoepitaxial growth the modes are: i) step flow growth, ii) layer-by-layer growth iii) island growth. As illustrated in **Figure 2.11**, for heteroepitaxial growth, as also employed in this thesis, three typical growth modes exit. These can be distinguished from each other by relations between the various surface free energy terms: i) Frank-van-der-Merve mode, ii) Volmer-Weber mode, iii) Stranski-Krastanov mode [29,30].

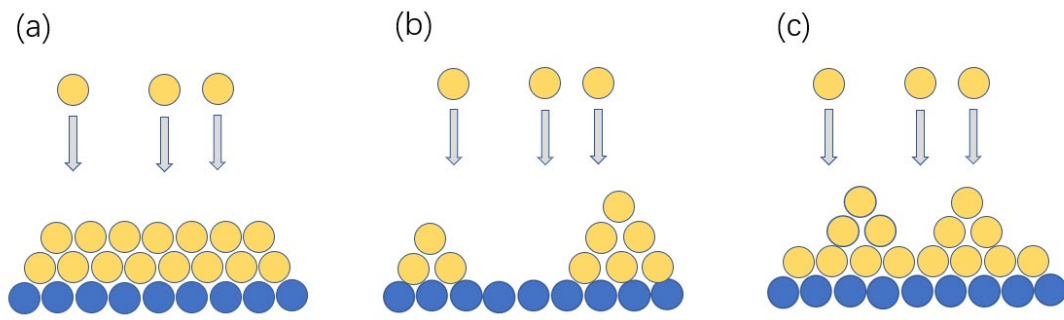**Figure 2.11** Growth modes of heteroepitaxial growth. (a) Frank-van-der-Merve mode, $\gamma_{film} + \gamma_{inter} < \gamma_{sub}$. (b) Volmer-Weber mode, $\gamma_{film} + \gamma_{inter} > \gamma_{sub}$. (c) Stranski-Krastanov mode, $\gamma_{film} + \gamma_{inter} + \gamma_{mis} > \gamma_{sub}$.

When the sum of the thin film surface free energy γ_{film} and the interface free energy γ_{inter} is smaller than the substrate free energy γ_{sub}, it is energetically more favorable for atoms to bond onto the substrate rather than to each other, thus a layer-by-layer growth called Frank-van-der-Merve mode and hence a smooth film surface is found. However, when $\gamma_{film} + \gamma_{inter} > \gamma_{sub}$, the Volmer-Weber mode is found leading to three-dimensional island growth with increased roughness. In between, the misfit free energy γ_{mis} can exhibit a strong influence, e.g. when reaching a critical thickness. Then the growth mode changes from layer-by-layer growth to island growth in order to relax the accumulated strain due to a lattice misfit. Such a mixed growth mode is called Stranski-Krastanov mode.

2.5 Scattering theory

Radiation can be scattered by an object from its original propagation direction. In this thesis, X-ray diffractometry and X-ray reflectometry is used to characterize the lattice structure and film thickness. Also, neutron diffractometry is employed to investigate the spin structure.

2.5.1 Basics of scattering

In the framework of quantum mechanics, radiation exhibits a wave-particle duality. Thus, scattering involves particle-particle collisions as well as reflection/refraction at surfaces/ interfaces and interference effects. When the sample size is far smaller than the source-to-sample and the sample-to-detector distance (**Figure 2.12**), Fraunhofer diffraction can be assumed (**Equation 2-17**), i.e. far-field diffraction with plane waves at the object and the observer.

$$R \gg \frac{D^2}{\lambda} \qquad (2-17)$$

$$|\vec{k}| = |\vec{k'}| = \frac{2\pi}{\lambda} \qquad (2-18)$$

$$Q = |\vec{Q}| = |\vec{k'} - \vec{k}| = \sqrt{\left(\vec{k'} - \vec{k}\right)^2} = \sqrt{k^2 + k'^2 - 2kk'\cos2\theta} = \frac{4\pi}{\lambda}\sin\theta \qquad (2-19)$$

The R refers to the distance between the diffracting object and the observation plane. The D and λ refer to the object diameter and the wavelength, respectively. The Fresnel diffraction in the near-field regime involves spherical waves. Additionally, elastic scattering is assumed. Thus, the incident and the scattered waves have the same wavelength as described in **Equation 2-18**, the $\vec{k}$ and $\vec{k'}$ represent the wave vector before and after scattering, respectively. Moreover, the corresponding relation between the scattering vector $\vec{Q}$ and the wave vector is shown in **Equation 2-19**. After scattering, the scattered wave exhibits a momentum difference of $\hbar\vec{Q}$ compared to the initial wave. The scattered intensity is proportional to the scattering cross section [31].
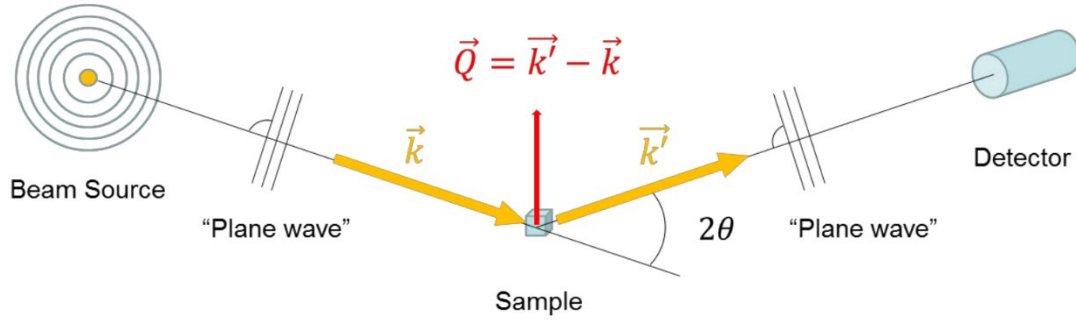
Figure 2.12 Scattering in the Fraunhofer diffraction approximation. Figure taken from Ref [32].

As illustrated in **Figure 2.13**, assuming the detector only covers a solid angle of $d\Omega$ with n particles per second scattered into $d\Omega$, the incident beam flux is J which refers to the number of particles per time and area. Then, the differential cross section is written as in **Equation 2-20**, where σ means the total scattering cross section. Additionally, the change of wave energy is ignored. Furthermore, the scattered intensity $I(\vec{Q})$ as well as the scattered amplitude $A(\vec{Q})$ is directly connected to the local wave-sample interaction potential $V(\vec{r})$ via the Fourier transformation, as seen in **Equation 2-21**. The $\vec{r}$ refers to the position of a scatterer inside a sample with volume V_s.

$$\frac{d\sigma}{d\Omega} = \frac{n}{jd\Omega} \qquad (2-20)$$

$$I(\vec{Q}) \sim |A(\vec{Q})|^2 \sim \left| \int_{V_s} V(\vec{r}) \cdot e^{i\vec{Q}\cdot\vec{r}} d^3r \right|^2 \qquad (2-21)$$
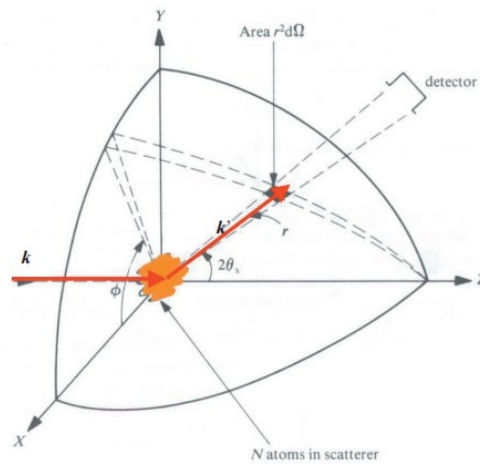

Figure 2.13 Definition of the scattering cross section. Figure adopted from Ref [31].

21

2.5.2 X-ray diffractometry

X-rays can be produced using an X-ray tube or a synchrotron and are highly useful in scientific research, e.g. for X-ray diffractometry, X-ray reflectometry and X-ray absorption spectroscopy. The scattering process of electromagnetic radiation with the electron orbitals of atoms is dominated by Thomson scattering, i.e. charge scattering. The scattering cross section for each atom is independent of $\vec{Q}$ due to the point-like approximation as described in **Equation 2-22** [31]. The r_0 is the classical electron radius and $P(\theta)$ describes the polarization dependence.

X-ray diffractometry can be employed to characterize periodic crystalline structures due to the similar length scale between the X-ray wavelength (ca. 0.1nm) and typical crystal lattice distances. The Bragg equation (**Equation 2-23**) describes the condition for constructive interference, i.e. the propagation distance difference (AB+BC) equals the integer number (*n*) of the incident wavelength (λ). The lattice spacing is d_{hkl} (*hkl* are the Miller indexes).

$$\frac{d\sigma}{d\Omega} = r_0^2 \cdot P(\theta) \qquad (2-22)$$

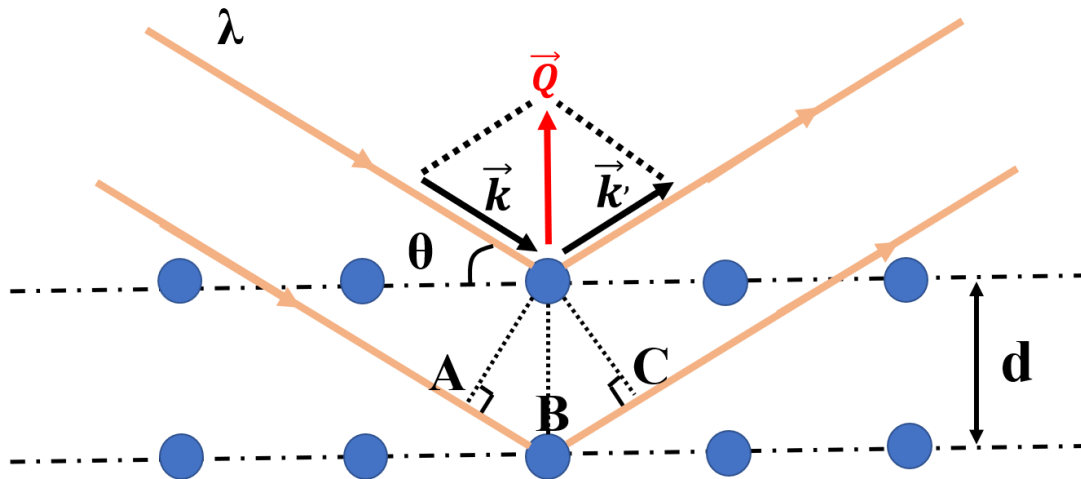$$2d_{hkl} \times sin\theta_{hkl} = n \times \lambda \qquad (2-23)$$

Figure 2.14 Sketch of X-ray scattering in a crystal lattice.

In a three-dimensional crystal lattice, the lattice primitive vectors are defined as $\vec{a}_1, \vec{a}_2$ and $\vec{a}_3$, while for reciprocal lattice, the primitive vectors $\vec{b}_1, \vec{b}_2$ and $\vec{b}_3$ are written in **Equation 2-24**.

$$\begin{cases} \vec{b}_1 = 2\pi \dfrac{\vec{a}_2 \times \vec{a}_3}{\vec{a}_1 \cdot (\vec{a}_2 \times \vec{a}_3)} \\[4mm] \vec{b}_2 = 2\pi \dfrac{\vec{a}_3 \times \vec{a}_1}{\vec{a}_2 \cdot (\vec{a}_3 \times \vec{a}_1)} \\[4mm] \vec{b}_3 = 2\pi \dfrac{\vec{a}_1 \times \vec{a}_2}{\vec{a}_3 \cdot (\vec{a}_1 \times \vec{a}_2)} \end{cases} \qquad (2-24)$$

In the Ewald sphere, the diffraction condition can be visualized as shown in **Figure 2.15 (a)**. Assuming elastic scattering, all reciprocal lattice points with indices *hkl* on the Ewald sphere, i.e. where its radius equals $|\vec{k}| = \frac{2\pi}{\lambda}$ corresponds to constructive interference. When written in vector notation this corresponds to the condition $\vec{Q} = n \times \vec{G}_{hkl}$, where $\vec{G}_{hkl}$ is the reciprocal lattice vector shown in **Equation 2-25** [32]. The Bragg equation can then be derived from **Equation 2-19** and **Equation 2-25** shown in **Figure2.15 (b)**.

$$|\vec{G}_{hkl}| = |h\vec{b}_1 + k\vec{b}_2 + l\vec{b}_3| = \frac{2\pi}{d_{hkl}} \qquad (2-25)$$

(a)   (b)
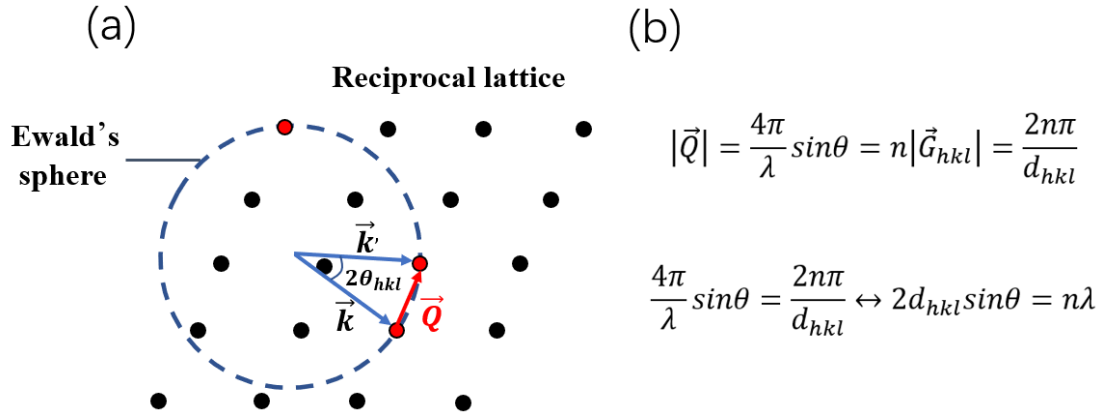
Figure 2.15 (a) Ewald construction in reciprocal lattice (Laue condition). (b) Bragg equation derivation from **Equation 2-19** and **Equation 2-25**.

2.5.3 X-ray reflectometry

X-ray reflectometry is widely used for thin film surface and interface characterization. At grazing incidence (incident angle $\theta \ll 5°$), the physical formalism can be described in terms of optical reflection and refraction. For angles below the critical angle θ_c, the incident X-ray beam

undergoes total reflection. The critical angle can be calculated using **Equation 2-26** (Snell's law) [31].

$$\theta_c = arcsin(1/n) \cong \lambda\sqrt{\frac{\rho}{\pi}} \qquad (2-26)$$

The ρ refers to the electron density of the material. When the incident angle is above θ_c, the incident beam can be partially transmitted toward the film. Assuming an ideally flat (sharp) film surface, the reflectivity R and transmissivity T are described by the Fresnel formulas (**Equation 2-27** and **2-28**), the k_{z0} and k_{z1} refer to the wave vector component in the out-of-plane direction (the z-direction) for vacuum (0) and for the material (1), respectively.

$$R = \left|\frac{k_{z0} - k_{z1}}{k_{z0} + k_{z1}}\right|^2 \qquad (2-27)$$

$$T = \left|\frac{{k_{z0}}^2}{k_{z0} + k_{z1}}\right|^2 \qquad (2-28)$$

The Fresnel formulas can also be described as a function of the magnitude of the scattering wave vector $\vec{Q}$ (**Equation 2-29**, reduced by a factor of Q^{-4}), the Q_c represents the reflection at the critical angle θ_c (**Equation 2-30**) [31].

$$R = \left|\frac{Q - \sqrt{Q^2 - Q_c^2}}{Q + \sqrt{Q^2 - Q_c^2}}\right|^2 \xRightarrow{Q \gg Q_c} \frac{Q_c^4}{16Q^4} \qquad (2-29)$$

$$Q_c = 2k_{z0,c} = \frac{4\pi sin\theta_c}{\lambda} \approx \frac{4\pi\theta_c}{\lambda} \qquad (2-30)$$

Moreover, interference can occur for the reflected beams from different surfaces/interfaces as shown in **Figure 2.16** resulting in a periodic oscillation with a period ΔQ described in **Equation 2-31** and **2-32**. This provides the possibility for the determination of the film thickness (t). In addition, considering a rough surface in the nanometer range, diffuse scattering can contribute to the scattered intensity. Accordingly, a roughness determination of both the film surface as well as the interface is also possible [31].

$$\lambda = 2t\Delta(sin\theta) = 2t\Delta\left(\frac{\lambda Q}{4\pi}\right) \qquad (2-31)$$
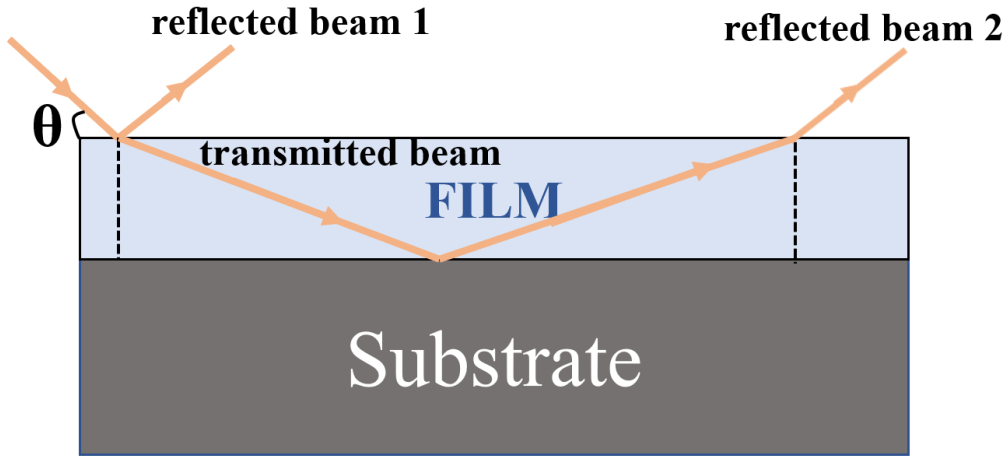
$$\Delta Q = \frac{2\pi}{t} \qquad (2-32)$$

Figure 2.16 Sketch of the reflection and refraction at the film surface and the film-substrate interface.

2.5.4 Neutron diffractometry

Neutrons can be produced by fission, spallation or various nuclear reactions. Considering neutron-matter interactions, the first contribution is the scattering at the nucleus which exhibits a scattering-angle-independent differential cross section shown in **Equation 2-33** [31]. The b refers to the scattering length characterizing the interaction potential. Moreover, b depends not simply on the atomic number and thus it leads to a non-monotonical relation in contrast between the scattering intensity and the atomic number, which is different compared to X-ray scattering.

$$\frac{d\sigma}{d\Omega} = |b|^2 \qquad (2-33)$$

$$\mu_n = -1.913\mu_N \qquad (2-34)$$

The second part is the magnetic scattering (magnetic dipole-dipole interaction) between the magnetic moment of the neutron μ_n (**Equation 2-34**) and of the unpaired electrons of the material, the μ_N denotes the nuclear magneton. The differential cross section is related to the polarization state of the neutron as illustrated in **Equation 2-35**. The σ_Z and σ_Z' refer to the change of the neutron polarization state during the scattering process, the $\vec{M}_\perp$ and $\hat{\vec{\sigma}}$ represents the magnetization after the Fourier transform perpendicular to $\vec{Q}$ and the spin operator, respectively, as shown in **Equation 2-36**.

$$\frac{d\sigma}{d\Omega} = (5.39fm)^2 \left| -\frac{1}{2\mu_B} \langle \sigma_z' | \hat{\vec{\sigma}} \cdot \vec{M}_\perp(\vec{Q}) | | \sigma_Z \rangle \right|^2 \qquad (2-35)$$

$$\begin{cases} \vec{M}_\perp(\vec{Q}) = \hat{\vec{Q}} \times \vec{M}(\vec{Q}) \times \hat{\vec{Q}} \\ \vec{M}(\vec{Q}) = \int \vec{M}(\vec{r}) e^{i\vec{Q}\cdot\vec{r}} d^3r \end{cases} \qquad (2-36)$$

For neutron scattering, the two parts (nuclear and magnetic scattering) are of similar order of magnitude and thus enable to study both the atomic structure and the magnetic structure simultaneously. Similar to X-ray diffractometry, coherent elastic scattering (diffraction) of neutron waves at the crystal lattice also leads to the Bragg law as shown in **Equation 2-23**.

3. Experimental Methods and Instruments

In this chapter, the sample growth, the characterization methods and the corresponding instruments are briefly introduced. Thin films of $La_{0.7}Sr_{0.3}MnO_3$ are epitaxially grown by the High Oxygen Pressure Sputter Deposition (HOPSD) device. For as-prepared samples and post-treated samples, the crystallinity and the out-of-plane lattice parameter (for thin film) are investigated by X-ray Diffraction (XRD). In addition, the structural film state is probed by Reciprocal Space Mapping (RSM). The film thickness and surface roughness are determined using X-ray Reflectivity (XRR). The topography of films and the morphology of power samples are probed by Atomic Force Microscopy (AFM) and by Scanning Electron Microscopy (SEM), respectively. The electric transport and magnetic properties are characterized by the Physical Properties Measurement System (PPMS) and using a Superconducting Quantum Interference Device (SQUID) magnetometer. Furthermore, Rutherford Backscattering Spectrometry (RBS) and Inductively Coupled Plasma Optical Emission Spectroscopy (ICP-OES) are employed to determine the stoichiometry. The study of the oxidation state and of the spin structure are based on X-ray Absorption Spectroscopy (XAS) and Neutron Diffraction (ND).

3.1 High Oxygen Pressure Sputter Deposition (HOPSD)

The sputtering technique is widely used in the field of thin film growth due to its ability to deposit high melting materials and to prepare multi-element films with the desired target stoichiometry. In this thesis, the on-axis deposition from a stoichiometric target using HOPSD

(**Figure 3.1**) is employed to grow epitaxial $La_{0.7}Sr_{0.3}MnO_3$ thin film samples. The growth process can be described with the following steps: i) oxygen plasma generation by a radio frequency (RF) excitation at 13.6MHz, the maximum power is 200W, ii) the generation of sputtered material released from the target via the bombardment of oxygen ions originating from the oxygen plasma. Moreover, charge accumulation at the target surface, which could lead to unwanted arcing, is avoided by the using an RF field, iii) the ejected atoms or clusters of atoms move towards the substrate, iv) followed by physi/chemisorption onto the substrate surface. There surface diffusion to energetical favorable sites and nucleation and crystal growth to form the film occur.

Compared with conventional low oxygen pressure sputter deposition (in the range of 10^{-2}mbar or lower), HOPSD uses oxygen pressures in the range of 1 to 4mbar and is suitable to fabricate metal-oxides in a better quality. On the one hand, the larger oxygen pressure can induce a lower mean free path of oxygen ions due to the enhanced multiple-scattering with the oxygen background gas, thus resulting in a localization of the oxygen plasma and suppressing the so-called resputtering effect of the negatively charged oxygen ions which can be accelerated by the bias voltage and bombard the already deposited film [33]. Moreover, the above mentioned effect depends not only on the oxygen pressure but on the target-substrate distance as well. In our study, a fixed value of 2cm is used. The larger oxygen pressure can also ensure a lower oxygen vacancy concentration during the growth process.

In our HOPSD device, a two-stage pumping system is employed to achieve a base vacuum in the range of 10^{-6}mbar. Oxygen gas is supplied via an oxygen cylinder and controlled through a mass flow controller (MFC) to achieve the desired oxygen pressure and oxygen flow. The sample holder can be heated up to a maximum temperature of 1000℃ for the pre-treatment of the substrate as well as for enhancing the atom surface diffusion during the growth. In addition, stoichiometric targets with a diameter of 5cm can be handled by a movable target arm and thus enable the choice of several materials for e.g. multilayer film growth.
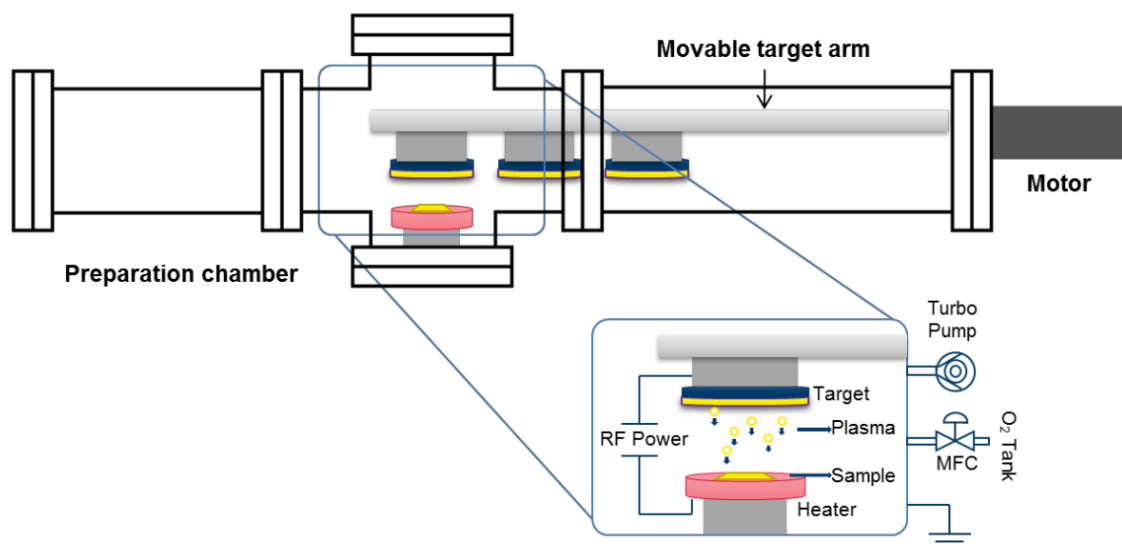
Figure 3.1 Sketch of the HOPSD device, figure taken from Ref [34]. On-axis RF sputtering with a maximum power of 200W. The target-substrate distance is fixed at 2cm.

3.2 X-Ray Reflectivity/ Diffraction (XRR and XRD)

As shown in **Figure 3.2**, the D8 Advance X-ray reflectometer from Bruker AXS is employed to characterize the out-of-plane crystallinity (XRD mode) as well as the thickness and the roughness of thin film samples (XRR mode). This device uses X-rays from the $Cu - K_{\alpha 1}$ characteristic line (1.54Å). Two Göbel mirrors are mounted in order to achieve a highly collimated beam for the reflectometry scan at lower angles, and a channel cut monochromator is installed for precise diffractometry scans at higher angles. In addition, a vacuum chamber with a heating stage is installed to provide various sample environments (maximum vacuum: 1×10^{-6}mbar, maximum temperature: 750℃), which enables in-situ vacuum annealing.

For powder samples, the crystal structure is characterized by a powder diffractometer which is a Huber Imaging Plate Guinier Camera G670 equipped with X-ray radiation from the $Cu - K_{\alpha}$ or $Mo - K_{\alpha}$ line, respectively. The signal is collected via a transmission geometry. By using a laser heating module and a closed-cycle cryostat, a sample environment at the high temperature range (673K to 1773K) or in the low temperature range (10K to 300K) can be realized.
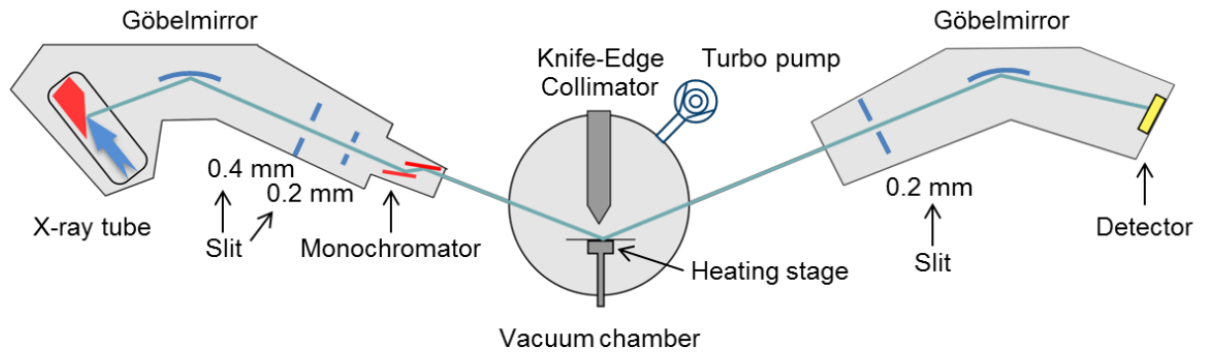
Figure 3.2 Sketch of the Bruker D8 Advance reflectometer equipped with a vacuum chamber and a heating stage, figure adopted from [35].

3.3 Reciprocal Space Mapping (RSM)

The film strain status is probe via RSM. The measurements were conducted by Anton Kaus, Suqin He and Moritz Weber at PGI-7, Forschungszentrum Jülich. The basic principle of RSM is shown in **Figure 3.3**. For LSMO thin film, the (103) Bragg peak of film and of substrate is probed to calculate the in-plane and out-of-plane lattice parameter, i.e. a_x and a_z. The scattering vector $\vec{Q}$ can be decomposed to $\vec{Q}_x$ and $\vec{Q}_z$ using the **Equation 3-1**. Then for a cubic crystal structure, e.g. LSMO, the a_x and a_z are calculated using **Equation 3-2** [12,36].

$$\begin{cases} |\vec{Q}_x| = |\vec{Q}\sin(\omega - \theta)| = \dfrac{4\pi}{\lambda}sin\theta\sin(\omega - \theta) \\ |\vec{Q}_z| = |\vec{Q}\cos(\omega - \theta)| = \dfrac{4\pi}{\lambda}sin\theta\cos(\omega - \theta) \end{cases} \quad (3-1)$$

$$\begin{cases} a_x = \dfrac{2\pi}{|\vec{Q}_x|}\sqrt{h^2 + k^2} = \dfrac{2\pi}{|\vec{Q}_x|}\sqrt{1^2 + 0^2} = \dfrac{2\pi}{|\vec{Q}_x|} \\ a_z = \dfrac{2\pi}{|\vec{Q}_z|}l = \dfrac{2\pi}{|\vec{Q}_z|}3 = \dfrac{6\pi}{|\vec{Q}_z|} \end{cases} \quad (3-2)$$
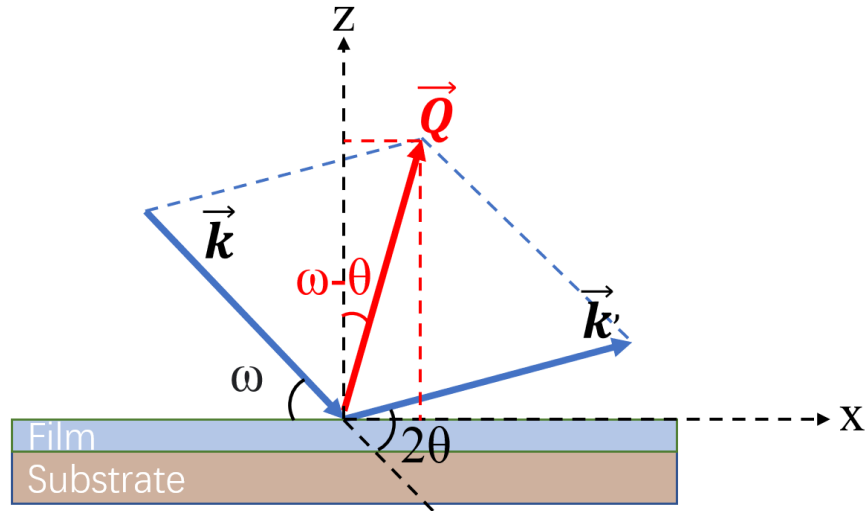
Figure 3.3 Basic principle of RSM, the scattering vector $\vec{Q}$ can be decomposed to $\vec{Q}_x$ and $\vec{Q}_z$ in the x-axis direction and in the z-axis direction, respectively.

3.4 Atomic Force Microscopy (AFM)

The topographic information of thin film samples is collected by an Agilent 5400 atomic force microscope. The basic working principle is described in **Figure 3.4**. By using a laser diode as well as a photodetector, the deflection of a spring-like cantilever with a pointed tip is probed. A feedback system equipped with piezoelectric response elements is used to control the tip-sample position. The tip-sample interaction can lead to a bending of the cantilever thus enabling a topographical imaging of the sample surface.

Three typical modes can be used. First, the tip can be arranged in direct contact with the sample surface called contact mode (static AFM), then the topography information is directly collected from the deflection of the cantilever. Second, by driving the cantilever at a fixed frequency (near the intrinsic resonance frequency of the cantilever) above the sample surface, a shift of the resonance frequency is induced by the tip-sample interaction, resulting in a change in the amplitude (dynamic AFM). This change is recorded. Third, the intermittent contact mode or so-called tapping mode is used when driving the tip directly in a tapping fashion on top of the sample surface [37]. In the above mentioned three modes, the feedback system can be either engaged providing the constant current mode or be disengaged leading to the constant height mode.
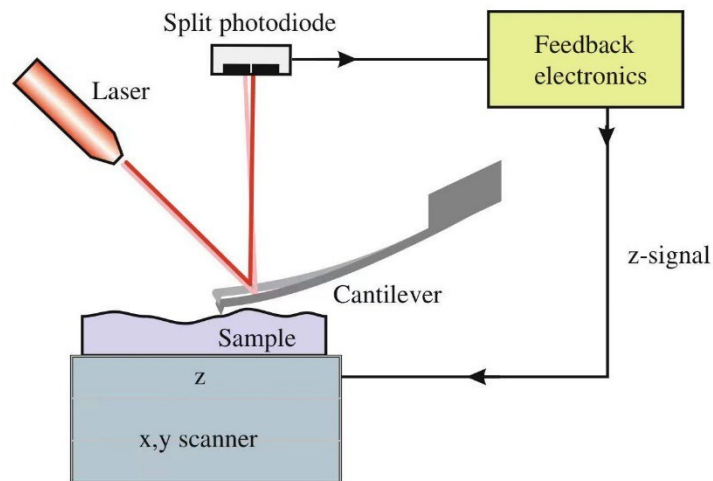
Figure 3.4 Schematic diagram of the AFM working principle, figure taken from [37].

3.5 Scanning Electron Microscopy (SEM)

The morphology of LSMO powder samples is probed via SEM. Measurements were performed by Benjamin Reineke using the JSM-6510 series instrument at JCNS-1. The schematic electron beam path is shown in **Figure 3.5**. Various signals can be produced by the incident electron beam, e.g. secondary electrons and backscattered electrons. The secondary electrons originated from the inelastic scattering between the electron beam and the sample are usually collected as the signal for surface topographic analysis. In addition, backscattered electrons being produced by elastic collisions in deeper regions are used for chemical composition contrast imaging [38].
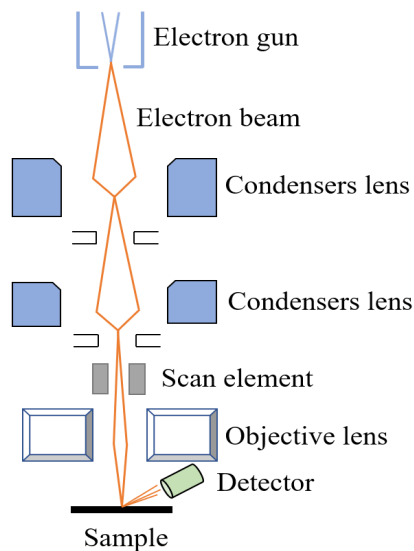

Figure 3.5 Schematic diagram of an SEM microscope.

3.6 SQUID magnetometry

The Superconducting Quantum Interference Device (SQUID) magnetometer from Quantum Design (model MPMS XL) with a sensitivity of $10^{-11} Am^2$ (10^{-8} emu) is employed to characterize the macroscopic magnetic properties of thin film samples as well as of powder samples. The basic principle of detection is illustrated in **Figure 3.6**. The RF-SQUID consists of a RF circuit including a superconducting ring with a Josephson junction as a nonlinear element inside the circuit. Thin film samples or powder pockets are mounted on a plateau prepared on the surface of a straw which is installed on the sample holder rod. By moving the sample holder rod up and down and hence through the pick-up coils, an electrical current is induced by the stray field of the magnetic moment of the sample. The induced current signal is transferred to the superconducting ring and finally probed by the RF circuit.

Using a superconducting solenoid, a magnetic field can be applied in the vertical direction in the range -7T to +7T. The sample environment temperature can be controlled between 1.9K and 400K. In addition, two measurement modes are usually employed. For the so-called direct current mode, the sample is moved through the pick-up coils once and in discrete steps. However, in the reciprocating sample option mode a harmonic oscillatory movement of the sample is used for a faster measurement and with a better signal to noise ratio.
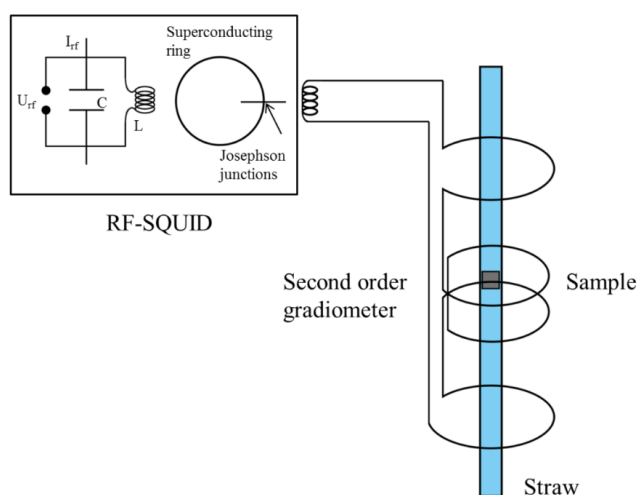

Figure 3.6 Sketch of the SQUID magnetometer detection system with the sample holder straw (blue) with a plateau and a mounted sample (grey square). Figure adopted from [39].

3.7 Physical Properties Measurement System (PPMS)

The Physical Properties Measurement System (PPMS) from Quantum Design, with sample temperatures possible in the range 1.9K to 400K and magnetic fields possible in the range -9T to +9T, enables various physical properties measurements, e.g. electric transport properties, thermal transport properties and magnetization. A schematic of the instrument is illustrated in **Figure 3.7 (a)**.

In this thesis, electric transport properties (i.e. resistivity) of thin films are measured via the van der Pauw method using 4 contacts (**Figure 3.7 (b)**). Thin films are fixed using double-sided tape on the platform of the so-called "resistivity puck", and then connected to the electrodes (I^+, V^+, V^-, I^-) by Pt-wires and silver paste.

The van der Pauw method (four-point probe at the film corners) provides the average sheet resistivity and the Hall coefficient of a laterally homogeneous films. Additionally, the four-point probe can be arranged in a linear way, the so-called linear four-point probe. The latter method can only yield the resistivity along the probe direction and is not suitable for the materials with an anisotropy [40]. The above-mentioned methods require that the contacting area of electrodes should be much smaller than the film size to ensure a point contact. In addition to resistivity measurements, the Vibrating-Sample Magnetometer (VSM option) is employed to measure the magnetization of the samples. Compared to the SQUID magnetometer it has a lower sensitivity of ca. 10^{-9}Am^2 (10^{-6}emu).
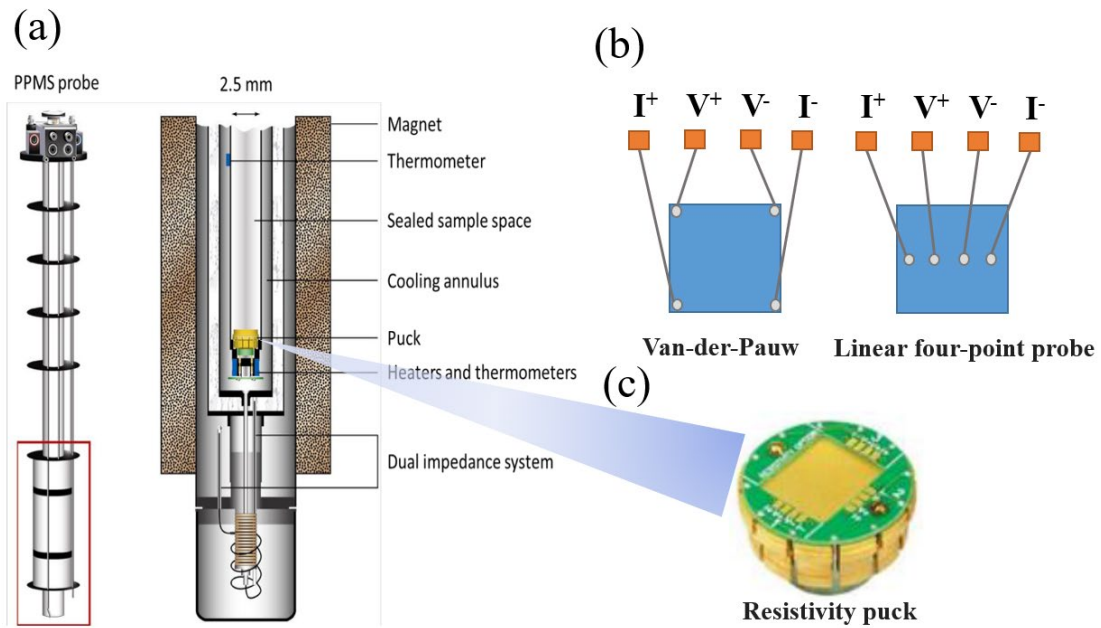
Figure 3.7 (a) Schematic of PPMS, figure taken from Ref [41]. (b) Probe configuration of the Van-der-Pauw method and the linear four-point probe method. (c) Resistivity puck.

3.8 Rutherford Backscattering Spectrometry (RBS）

As a nuclear method, RBS offers non-destructive near-surface analysis of solids and can be employed to quantitatively determine material composition and to probe the elemental depth profiles [42]. In this thesis, RBS was measured at HZDR in Dresden by Dr. Wang Mao and Yunxia Zhou to determine the stoichiometry of films. The analysis of the data was performed completely by myself. As illustrated in **Figure 3.8**, $^4He^+$ ions are accelerated by the Rossendorf van de Graff accelerator to 1.7MeV and bombard a target (sample). This incident high-energy ion beam can be elastically backscattered by the nucleus of target atoms, i.e. Rutherford backscattering. A energy sensitive detector is placed at a backscattering angle of 170° to detect the number as well as the energy loss of backscattered particles which depending on e.g. the element type, the element content and the scattering position. RBS exhibits a good sensitivity for heavy elements, while a lower sensitivity for light elements e.g. oxygen. The target can be rotated to enable a "random channel" mode where only the stoichiometry information is offered. Moreover, the incident angle of ion beam can be fixed to a particular direction to include the information of target crystallinity, and thus a "channeling" mode. In this thesis, only the data of random channel mode is shown.
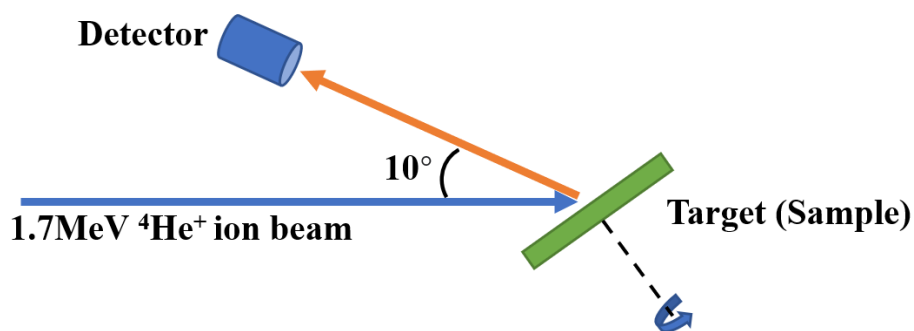
Figure 3.8 (a) Schematic diagram of RBS setup. The detector is placed at a backscattering angle of 170°. The target (sample) can be rotated to enable the random channel mode.

3.9 Inductively Coupled Plasma Optical Emission Spectroscopy (ICP-OES)

The stoichiometry of the as-prepared LSMO powder sample is characterized by ICP-OES. Measurements were performed via the instrument iCAP 6500 at ZEA-3. As **Figure 3.9** illustrates, the powder sample is first dissolved in hydrochloric acid and hydrogen peroxide. Then the solution is vaporized and mixed with Ar-gas. Subsequently, an Ar-plasma is inductively generated setting atoms to excited states. The following falling-back to the atomic ground states leads to the emission of characteristic radiation. A spectrometer is employed to probe the emitted spectrum. The element contained in the sample can thus be determined quantitatively from its characteristic emission lines and their intensities. ICP-OES exhibits an accuracy of 1-3% for the content determination of main elements.
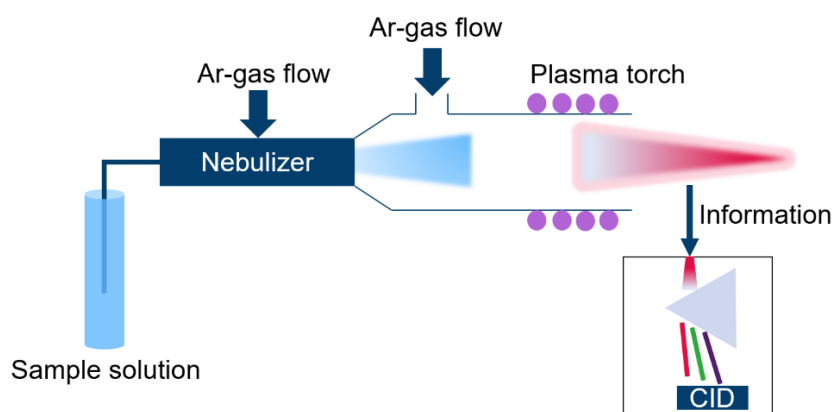

Figure 3.9 Schematic diagram of ICP-OES. The powder sample is dissolved and vaporized. The emitted spectrum triggered by an Ar-plasma is measured via a spectrometer and Charge

Injection Device (CID) detectors.

3.10 X-ray Absorption Spectroscopy (XAS)

High resolution X-ray Absorption Spectroscopy (XAS) is employed to explore the electronic structure of ions. In this thesis, XAS measurements were performed by Suqin He, Dr. Tomas Duchon and Dr. Stefan Cramm at BESSY II, Helmholtz Zentrum Berlin. The analysis of the data was performed completely by myself. The Mn $L_{2,3}$-edge, La $M_{4,5}$ -edge and O K-edge of LSMO films are probed. XAS requires a tunable X-ray source which is usually only available at a synchrotron source. Compared with X-ray photoelectron spectroscopy (XPS), in XAS electrons are excited to the conduction band rather than to the vacuum level. Additionally, XAS exhibits a higher resolution (ca. 0.15 eV) than XPS (0.5 eV) and thus can give more detailed information from the line shape and the energy position. Moreover, XPS is very sensitive to the chemical potential. The basic principle of XAS is shown in **Figure 3.10**, where the Mn L_3 excitation is taken as example. Electrons are excited via X-ray induced photoexcitation from core levels (e.g. K, L and M shells) to the conduction band. This yields so-called "absorption edges". The transition of electronic states follows the dipole selection rules. Due to the different binding energies of core levels as well as the different density of states in the conduction band, the absorption edges probe the electronic structure of the material [43-47].
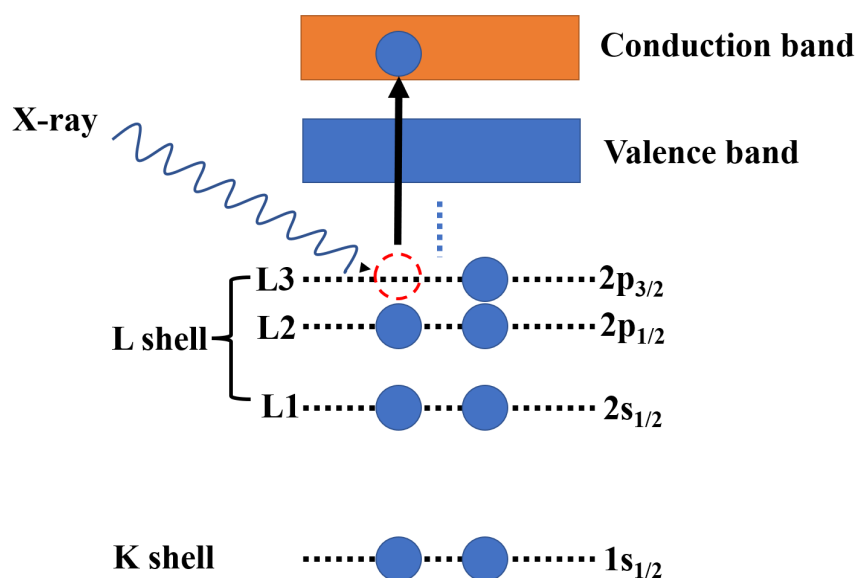
Figure 3.10 Basic principle of XAS as example depicted for the photoexcitation of Mn L_3. The 2p orbital is splitted in $2p_{3/2}$ and $2p_{1/2}$ levels due to the spin-orbit interaction. Electrons in the

$2p_{3/2}$ orbital can be exited to the conduction band and form the Mn L_3 edge in the absorption spectrum.

3.11 Neutron Diffraction (ND)

For this thesis, neutron diffraction on LSMO films were conducted by Suqin, Dr. Karin Schmalzl and Dr. Wolfgang Schmidt at the neutron source of the Institute Laue-Langevinin (ILL) Grenoble, France using the instrument IN12. The analysis of the data was performed completely by myself. IN12 is equipped with various possible sample environments, e.g. large range of temperatures, vacuum vessel, magnetic fields up to ca. 15T. It is a three-axis spectrometer for cold neutrons. The schematic diagram is illustrated in **Figure 3.11**. The neutron beam is first guided by the H144 supermirror guide and a certain wavelength band is selected by a velocity selector. A specific wavelength is filtered out by monochromator crystals (pyrolytic graphite (002)) and collimated towards the sample position. The sample on the sample table can be rotated. After the neutron-sample interaction, the scattered neutrons are detected. Finally, the energy of the neutrons entering the detector can be selected by a pyrolytic graphite (002) analyzer or Heusler analyzer [31].
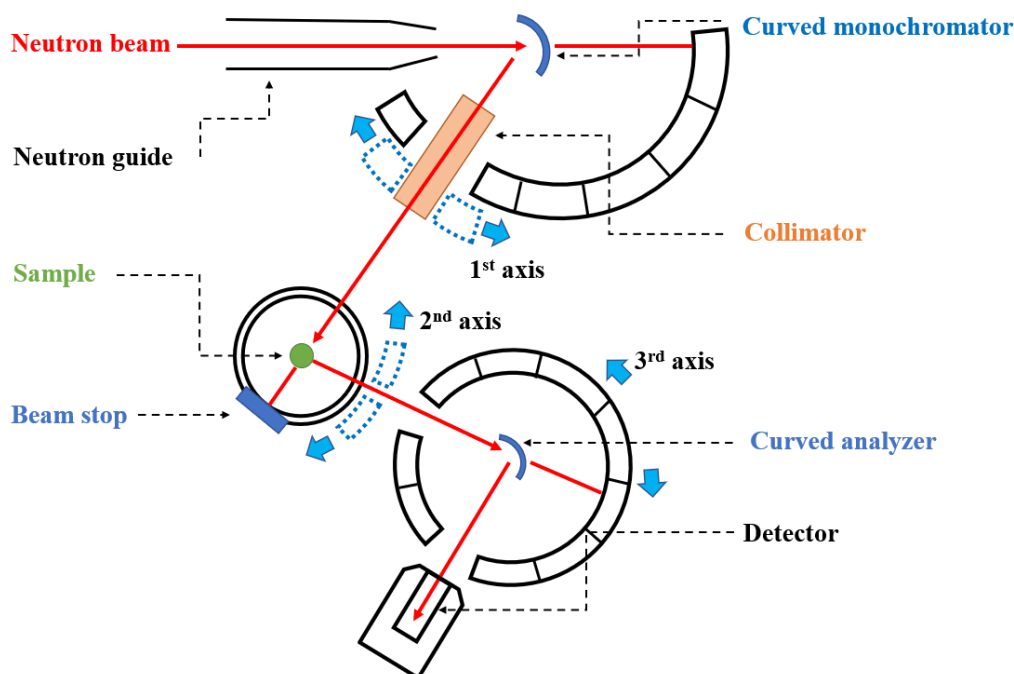

Figure 3.11 Schematic diagram of the three-axis spectrometer IN12. The neutron beam path is shown as a dotted red line.

4. Structural and physical properties of as-prepared epitaxial LSMO thin films

In this chapter, systematic studies on the sample-growth of $La_{0.7}Sr_{0.3}MnO_{3-\delta}$ (LSMO) thin films on insulating $SrTiO_3$ (STO) and on conductive Nb-doped STO (Nb-STO) substrates are described. The influence of growth parameters, i.e. growth temperature and growth time, onto the properties of the film, i.e. lattice structure, magnetic properties and stoichiometry, are investigated.

4.1 Sample preparation

4.1.1 Substrate selection

For the LSMO film growth, STO and Nb-STO substrates with (001) orientation purchased from the companies CrysTec GmbH or SHINKOSHA are selected. As illustrated in **Figure 4.1 (a)**, among other perovskite substrates, STO and $(LaAlO_3)_{0.3}(Sr_2AlTaO_6)_{0.7}$ (LSAT) show a lattice mismatch smaller than 1% referring to bulk-LSMO, which fits well the requirement for the epitaxial growth [48]. Compared with LSAT, STO has a simpler chemical composition and also exhibits a lower tendency for interdiffusion. Moreover, according to **Figure 4.1 (b)** the small thermal expansion coefficient as well as the good structural stability between room temperature and the growth temperature (>800°C) makes STO the best candidate for LSMO film growth. However at lower temperatures, STO will undergo a transition from the cubic to the tetragonal phase thus introducing problems for low-temperature measurements.

Previously ionic liquid gating experiments are performed with platinum (Pt) wires directly connected to the surface corners of the LSMO film. However, the transformation of LSMO occurs with poor uniformity. This is very likely due to the surface-corner electrode geometry. The LSMO near the corners undergo a higher transformation speed and eventually introduce subsystems.

Hence, conductive 0.05wt% Nb-doped STO substrates with resistivity ca. $0.1\Omega m$ are employed. Here, the Pt-wires can be connected either at the edge or on the backside of the substrate rather

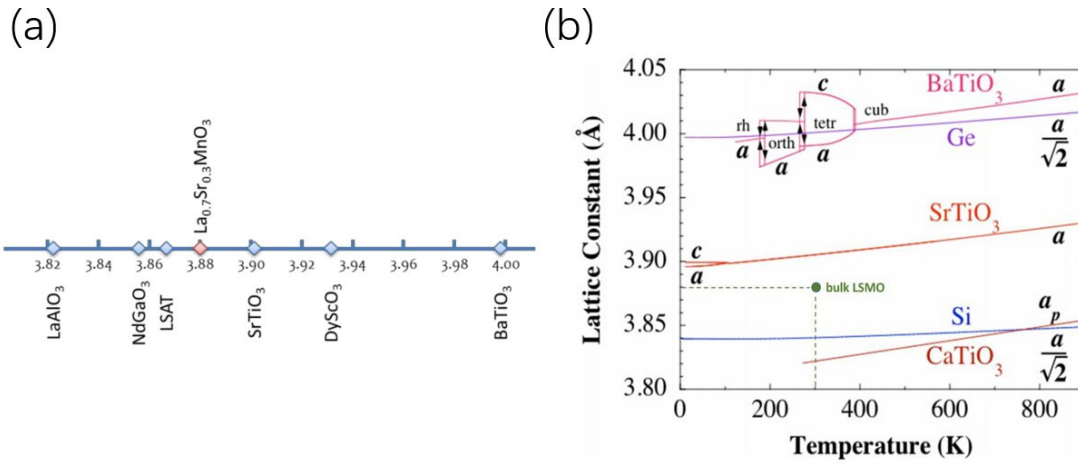than on the film. This can exclude the inhomogeneity introduced by the surface-corner electrode geometry.

(a)

(b)

Figure 4.1 (a) Lattice parameters of various perovskite substrates at room temperature, figure adopted from [11]. (b) Temperature dependence of the lattice constants of various perovskite substrates, figure taken from [49].

4.1.2 Growth details and sample list

Apart from the substrate, the growth temperature, oxygen pressure, plasma power, and the growth time determine the final film quality. For instance, the growth temperature can influence the diffusion and nucleation processes. Different plasma powers will affect the sputtering yield of each element in the target [50]. The oxygen pressure not only influences oxygen vacancies inside the film but acts together with the plasma power on the plasma plume.

Before actual sputtering, first, a 2-hour pumping process evacuates the system to 5.0×10^{-6} mbar. Then oxygen (1-3mbar) is supplied and a 2-hour pre-sputtering procedure with power 80 to 100W is used to remove the adatoms on the target. In the meantime, the substrate is annealed at 950°C in the chamber to achieve a clean and stoichiometric surface [51]. After that, the desired growth temperature is set and stabilized for 40min. Eventually, the growth procedure is started after the target is positioned to above the substrate. All the LSMO film samples involved in this thesis are listed in **Table 4.1**. In this thesis, most samples are grown using a set of already previously optimized parameters marked with blue color [12]. However, the samples are also labeled according to the statues of sputter target. First, a $La_{0.7}Sr_{0.3}MnO_3$ target was ordered form EVOCHEM company, defined as "status I". Then the

original target broke part during sputtering and was replaced by another target with the same stoichiometry from the EVOCHEM company, defined as "status II". After that, the ring which can limit the sputtering-area of the target broke-apart and was replaced. This led to a reduction of the sputtering-area from 16.6cm^2 to 10.2cm^2, defined as "status III".

Table 4.1 Substrate information and growth parameters.

Sample ID	Substrate type	Target status	Growth temperature [°C]	Oxygen pressure [mbar]	Plasma power [W]	Growth time [min]
SP568	STO	Status I	800	2	120	60
SP570	STO	Status I	800	2	120	60
SP576	STO	Status I	800	2	120	60
SP578	STO	Status I	800	2	120	60
SP581	STO	Status I	900	2	120	60
SP582	STO	Status I	700	2	120	60
SP589	Nb-STO	Status I	800	2	120	60
SP594	Nb-STO	Status I	800	2	120	60
SP601	STO	Status II	800	2	120	300
SP603	STO	Status II	800	2	120	300
SP609	Nb-STO	Status III	800	2	90	180

4.2 Growth parameters dependent change of physical properties

4.2.1 Sample growth during target status I

Samples grown during the target status I are intensively involved in the following post-treatment, i.e. 40 nm film series in Al-assisted vacuum annealing and in ionic liquid gating.

4.2.1.1 Structure and topography

First, the sample-growth using the previously determined parameters are repeated e.g. SP578. The topography of the as-prepared SP578 is characterized by AFM, as shown in **Figure 4.2**. The 2D image indicates that the film being sputtered at high oxygen partial pressure is uniform but not flat. There are no terraces observed, but bumps with an average height of ca. 5nm are distributed over the film surface (see **Figure 4.2 (b)**). The surface mean roughness is ca. 1.6nm.
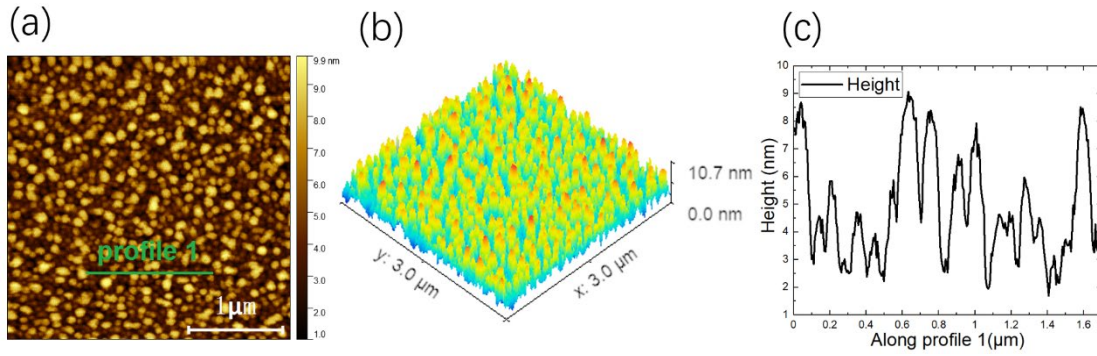
Figure 4.2 AFM topography scans of the as-prepared SP578. Panel (a), (b), and (c) show the 2D, 3D, and the height variation profile along a particular direction (profile1), respectively.

Figure 4.3 (a) and **Figure 4.4 (a)** illustrate the corresponding XRD and XRR pattern of the six as-prepared samples with the same growth parameters on STO and on Nb-STO substrates. The out-of-plane lattice parameters are determined via Gaussian peak position fitting and the Bragg equation. The error of the out-of-plane parameter calculation is estimated to be 0.001Å. The film thickness, roughness and scattering length density (SLD) are derived by fitting the XRR patterns. Results are shown in **Figure 4.4 (b)** and **Table 4.2**. For XRR fitting by the Software GenX, a three-layer model is used as demonstrated in **Figure 4.3 (b)**. A top layer with a thickness of ca. 0.5nm is employed to represent the air-film interface. Then followed by a LSMO layer and a ca. 1nm thick bottom layer which is used to represent the film-substrate interface. The deviation of XRR fitting is assumed to be ca. 1%.

The STO and Nb-STO substrates exhibit the same out-of-plane parameter of 3.902 ± 0.001Å. All films show an out-of-plane parameter ca. 3.85Å which is smaller than the bulk value 3.88Å indicating a compressive strain in the film out-of-plane direction. The clear Laue oscillations imply a good crystallinity. In XRR, the distinct Kissig oscillations reveal a flat film surface and interface quality. The film thickness is fitted to be ca. 40nm, while for SP594 one obtains only 33.73 ± 0.3nm. This can be attributed to the target problem since the target broke shortly after the preparation of SP594. The roughness calculated by XRR is ca. 2nm. The films grown on Nb-STO exhibit a relatively higher SLD of 3% compared with the films grown on STO. Hence, the HOPSD demonstrates a good repeatability on sample growth. The films grown on Nb-STO do not show a significant difference compared to the films grown on STO.
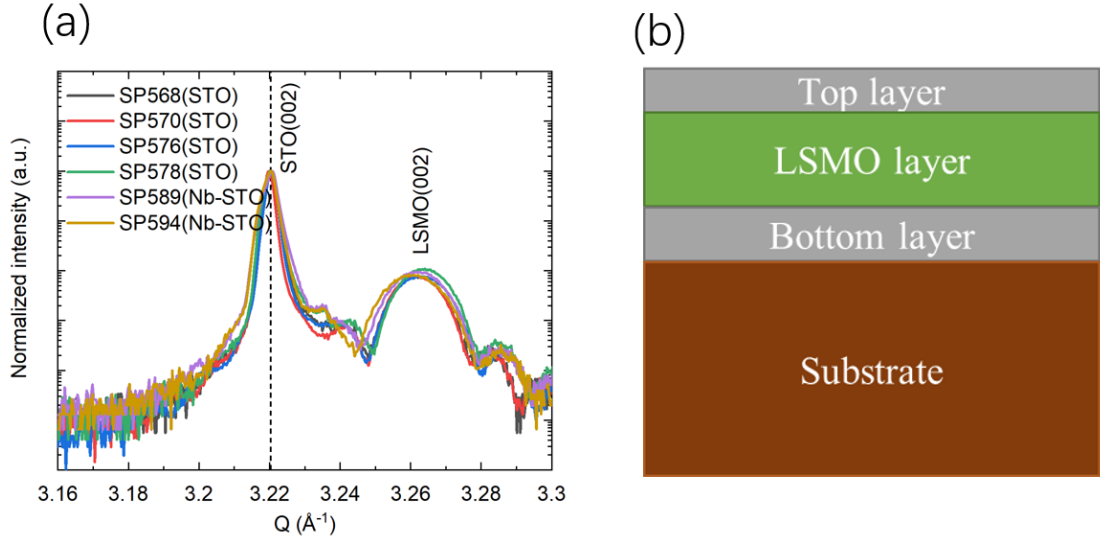
Figure 4.3 (a) XRD scans in the $Q(Q_z)$ range 3.16Å^{-1} to 3.3 Å^{-1} of films grown at the previously determined parameters. SP568, SP570, SP576 and SP578 are grown on STO substrates. SP589 and SP594 are grown on Nb-STO substrates. (b) Schematic of the 3-layer model used in XRR fitting.
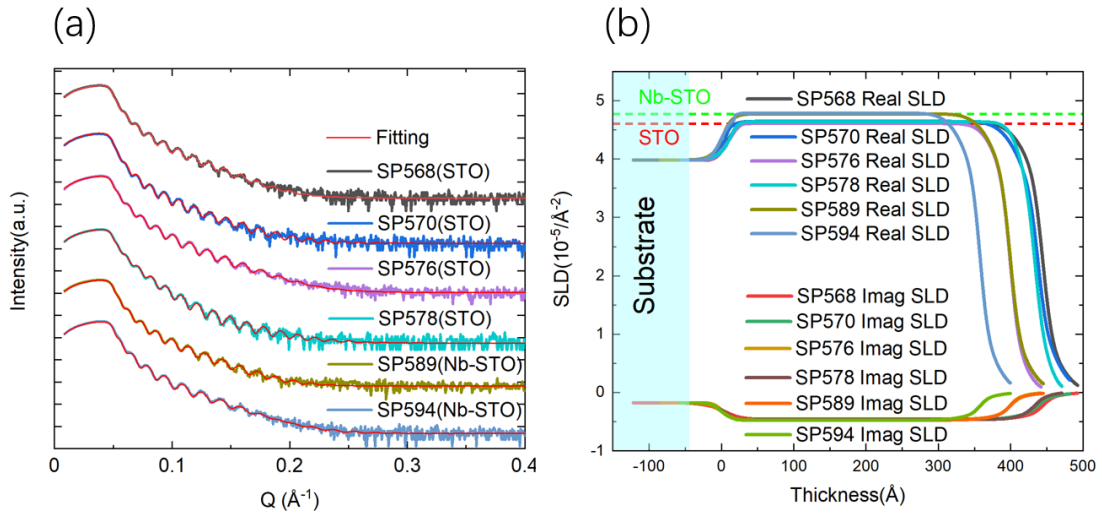

Figure 4.4 (a) Fitted XRR pattern of the as-prepared state of SP568, SP570, SP576, SP578, SP589 and SP594 (b) Corresponding calculated SLD. Fitted by the software GenX.

Table 4.2 XRD and XRR results of films grown at the same parameters

Sample ID	Substrate type	Out-of-plane [Å]	Thickness [nm]	Roughness [nm]	SLD [$10^{-5} \times \text{Å}^{-2}$]
SP568	STO	3.852±0.001	43.41±0.4	3.04±0.03	4.638±0.05
SP570	STO	3.852±0.001	42.85±0.4	3.14±0.03	4.646±0.05
SP576	STO	3.851±0.001	38.13±0.4	2.46±0.02	4.611±0.05

SP578	STO	3.850±0.001	41.91±0.4	2.06±0.02	4.639±0.05
SP589	Nb-STO	3.852±0.001	39.54±0.4	3.02±0.03	4.776±0.05
SP594	Nb-STO	3.853±0.001	33.73±0.3	2.83±0.03	4.788±0.05

Previously, the influence of oxygen pressure onto film preparation was investigated by Dr. Lei Cao [10,11]. Then Hengbo Zhang focused on tuning the plasma power and growth time to improve the film quality [12, 52]. In this thesis, the influence of specifically the growth temperature onto the film quality is studied. For SP582, SP578 and SP581, the growth temperatures 700°C, 800°C and 900°C are selected. Apparently, the temperature variation of 200°C failed to induce significant changes in the XRD pattern as shown in **Figure 4.5**. All three temperatures exhibit similar LSMO peak positions and intensities and with an out-of-plane lattice parameter of ca. 3.85Å. As shown in **Figure 4.6** and **Table 4.3**, both thickness, roughness and SLD have not been significantly influenced by the temperature variation of 200°C. These results provide a hint that films with a good quality might also be obtained at a lower growth temperature.
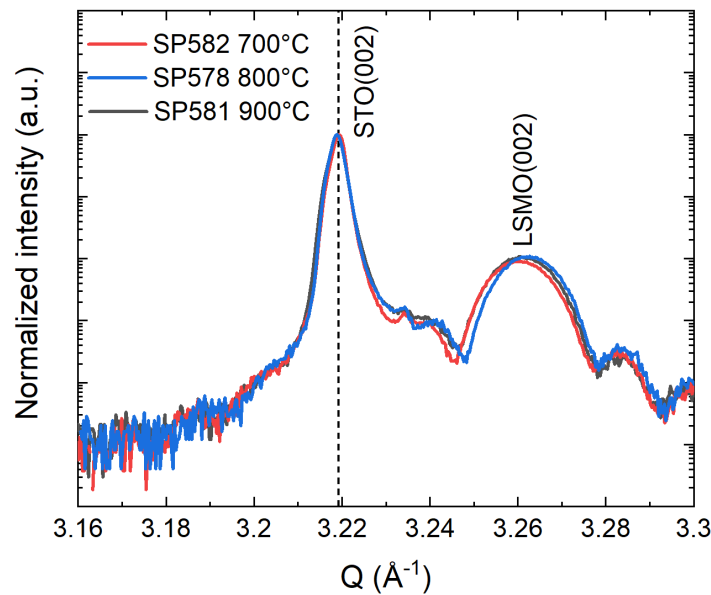

Figure 4.5 XRD patterns of the as-prepared states of SP582, SP578 and SP581. Samples are grown at 700°C, 800°C and 900°C, respectively.
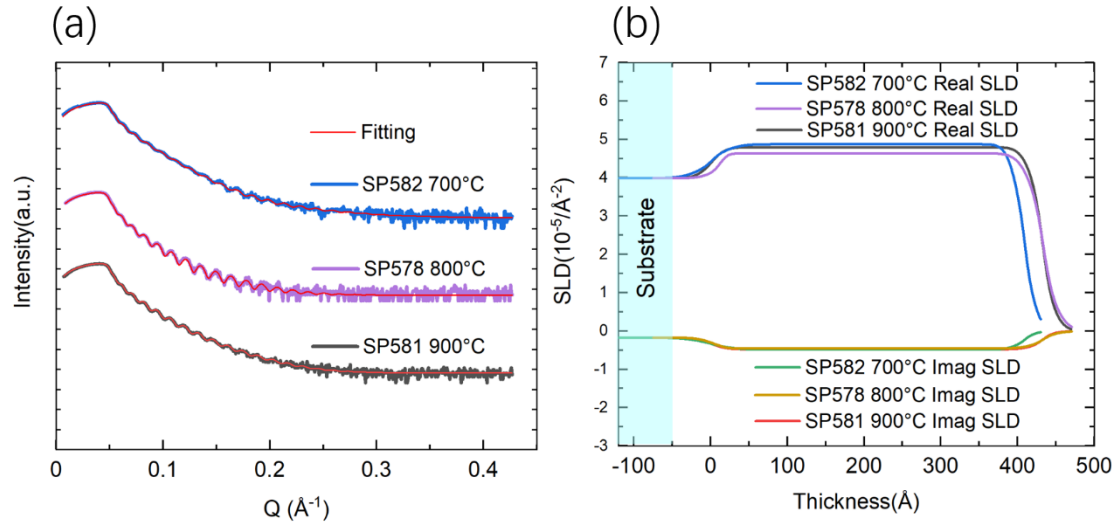
Figure 4.6 (a) Fitted XRR pattern of the as-prepared state of SP582, SP578 and SP581. (b) Corresponding calculated SLD.

Table 4.3 XRD and XRR results of films grown at different temperatures

Sample ID	Growth Temperature [°C]	Out-of-plane [Å]	Thickness [nm]	Roughness [nm]	SLD [$10^{-5} \times Å^{-2}$]
SP582	700	3.855	40.59	1.51	4.874
		±0.001	±0.4	±0.02	±0.05
SP578	800	3.850	41.91	2.06	4.639
		±0.001	±0.4	±0.02	±0.05
SP581	900	3.853	42.87	1.76	4.795
		±0.001	±0.4	±0.02	±0.05

4.2.1.2 Magnetic behavior

The influence of the growth temperature onto the film magnetic properties is characterized by SQUID magnetometry. **Figure 4.7(a)** shows the hysteresis loops measured at 10K. The field cooling (FC) curves are depicted in **Figure 4.7(b)**. **Table 4.4** illustrates the estimated saturation magnetization M_S, coercive field H_C and Curie temperature T_C. For samples grown at 700°C, 800°C and 900°C, rectangular shaped loops indicate that the magnetization reversal occurs by domain wall motion. Typical ferromagnetic behavior is observed in FC curves. A kink is observed at 105K which is very likely induced by the influence of the STO phase transition onto the film magnetic anisotropy. Among the investigated temperatures, the 800°C result shows both high M_S of $3.08\pm0.02\mu_B$/Mn and T_C of 326.6 ± 1K. This implies a good long-range

magnetic ordering of the film grown at 800°C. However, the larger $\mu_0 H_C$ of 14.16±0.5mT might reveal that the domain wall motion is hindered by pinning to crystal defects. μ_0 refers to the permeability of free space. The sample grown at 700°C shows a reduction of T_C by ca. 14K, while at 900°C the M_S is reduced to only 2.41±0.02μ_B/Mn.

To summarize, samples grown at 700°C, 800°C and 900°C can hardly show a clear difference in XRD and XRR. The 800°C grown film is found to exhibit the best magnetic ordering via magnetometry and thus makes 800°C the optimal temperature for sample growth.
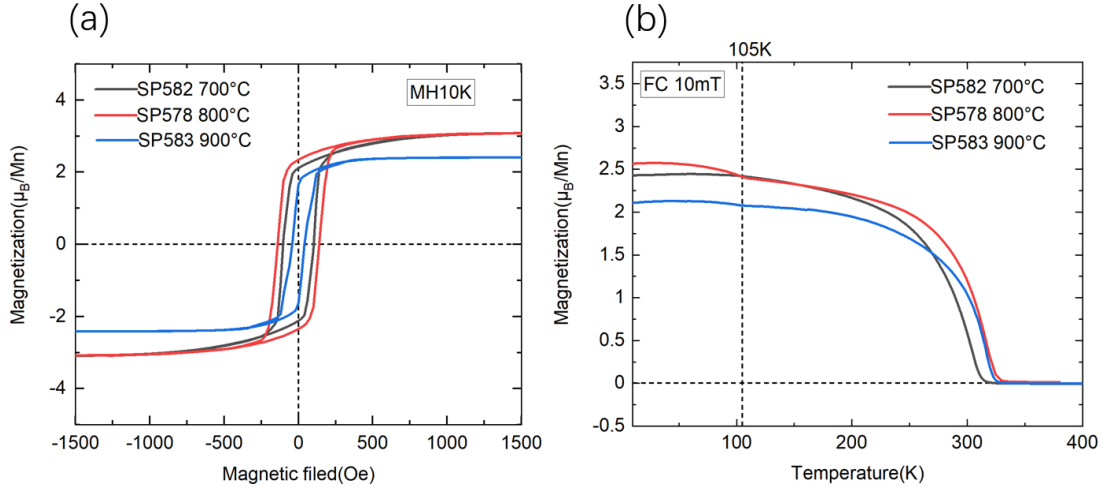

Figure 4.7 (a) Hysteresis loops of the as-prepared samples grown at different temperatures i.e. 700°C for SP582, 800°C for SP578 and 900°C for SP581, measured at 10K. (b) Corresponding FC curves measured at 10mT. The kink at 105K can be attributed to the influence of the STO phase transition.

Table 4.4 Estimated M_S, H_C and T_C of films grown at different temperatures

Sample ID	Growth Temperature [°C]	M_S [μ_B/Mn]	$\mu_0 H_C$ [mT]	T_C [K]
SP582	700	3.08±0.02	10.33±0.5	312.2±1
SP578	800	3.08±0.02	14.16±0.5	326.6±1
SP581	900	2.41±0.02	4.17±0.5	322.8±1

4.2.1.3 Mean field theory approximation

Mean field theory is employed to estimate the total angular momentum quantum number J of the as-prepared SP578. For manganese ion 3d orbitals, the orbital angular momentum is assumed to be fully quenched i.e. $L = 0$. Thus, the $g_J = 2$ according to **Equation 2-5**. For

Mn^{3+}, J is calculated via $J = |L - S|$ to be 2 and for Mn^{4+} to be 1.5. With the assumption that 70% Mn^{3+} and 30% Mn^{4+} coexist in La$_{0.7}$Sr$_{0.3}$MnO$_3$, the ideal J value for the double exchange interaction is estimated to be 1.85. Illustrated in **Figure 4.8(a)**, the fitting region is selected to be between 130K and 380K, thus the disturbance of STO phase transition at 105K can be excluded. In the FC curve, the M_S is evaluated by extending the curve from 130K to 0K to be 2.4μ$_B$/Mn, and T_C is set as mentioned before to 326.6K. A magnetic field of 10mT is applied. The related equations in **Chapter 2** are listed below. Based on these parameters, the fitting process is: i) calculation of λ via **Equation 4-1** for different J values, ii) y calculated via **Equation 4-2**, the measured magnetization $M_{measured}$ is inputted for representing the effective mean field $\vec{B}_{mf} = \lambda M_{measured}$, iii) a new magnetization $M_{calculated}$ is calculated using the mean field approximation via **Equation 4-3**.

$$\lambda = \frac{3k_B T_C}{g_J \mu_B (J+1) M_S} \tag{4-1}$$

$$y = \frac{g_J \mu_B J (B + \lambda M_{measured})}{k_B T} \tag{4-2}$$

$$\frac{M_{calculated}}{M_S} = B_J(y) = \frac{2J+1}{2J} \coth\left(\frac{2J+1}{2J} y\right) - \frac{1}{2J} \coth\left(\frac{y}{2J}\right) \tag{4-3}$$

The results are shown in **Figure 4.8(b)**. When decreasing the J value from 1.85 to 0.01, the model tends to converge to the experimental data. However, such small J values are unphysical. The mean field approximation can fit well in the region near T_C, while the deviation is larger at lower temperatures. Consequently, a perfect fitting is not found, and the J value can only be estimated to between 0.5 and 1. This is as expected. The mean field theory is a too rough approximation for highly correlated system such as complex oxides.
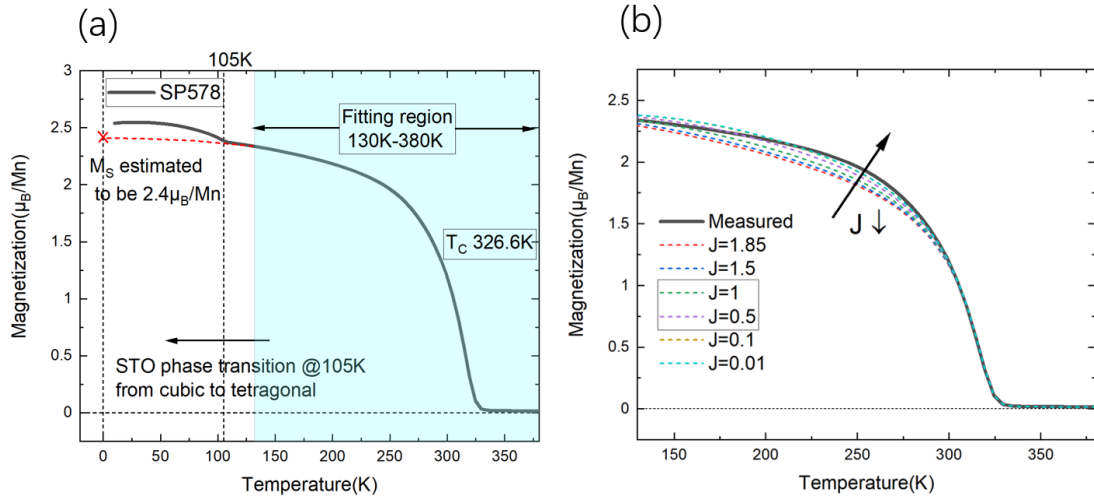
Figure 4.8 (a) FC curve of SP578 measured at 10mT, 130K-380K is selected as the fitting region. (b) J fitting using the mean filed theory approximation, different J values are chosen. The calculated curves at different J values are compared with the measured FC curve.

4.2.2 Sample growth during target status II

In the target status II, only several samples were prepared. These samples have a larger thickness by extending the sputtering time from 1 hour to 5 hours. "Thick" films were prepared in order to obtain a better signal for neutron diffraction studies.

4.2.2.1 Structure and topography

The surface topography of SP601 is characterized via AFM as shown in **Figure 4.9**. When the sputtering time is increased from 1 hour to 5 hours, isolated large islands with a height of ca. 15nm emerge. The surface mean roughness is 1.5nm.
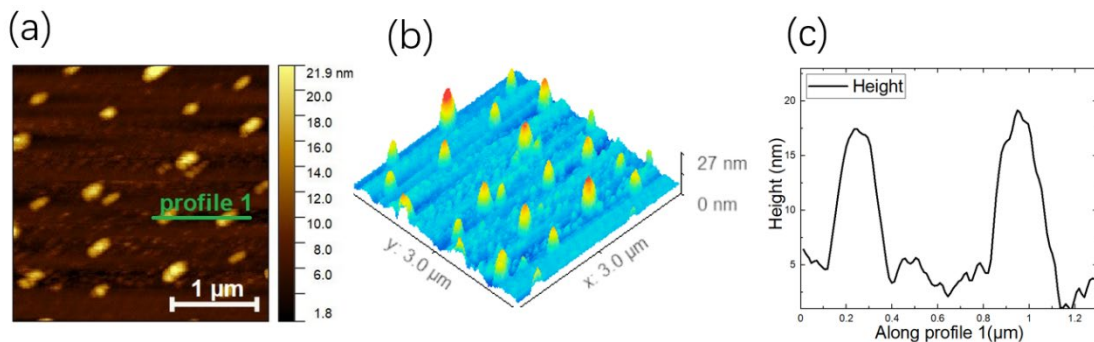

Figure 4.9 AFM topography scans of the as-prepared SP601. Panel (a), (b), and (c) show the 2D, 3D, and height variation profile along a particular direction (profile1), respectively.

Figure 4.10 illustrates the XRD patterns of SP601 and SP603. Compared to the 40nm film SP578, the out-of-plane lattice parameter is increased from 3.850 Å to 3.864 Å indicating that

the compression strain is partially relaxed. The (002) Bragg peak intensity is enhanced by a factor of 3.4 which might be due to the increased thickness. While when assuming the thickness to be ca. 200nm (according to the 5 hours sputtering time) the corresponding peak intensity should be enhanced by a factor of 25 referring to **Equation 2-21**. This limited enhancement of intensity implies that the thick film could be either less than 200nm or with a poorer crystallinity.
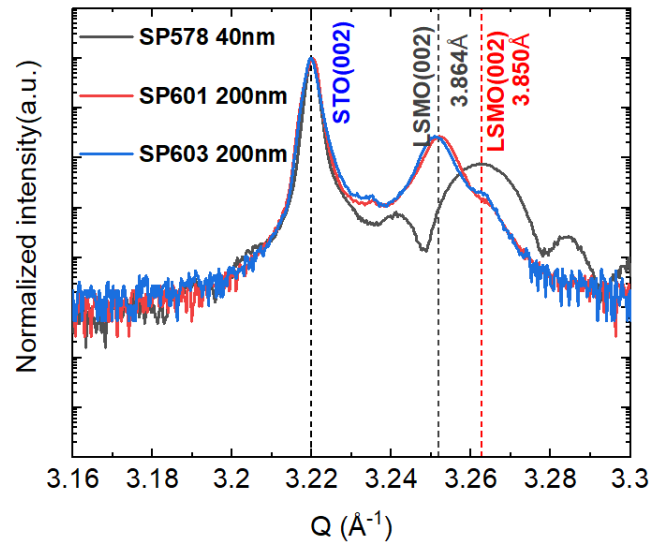

Figure 4.10 XRD patterns of as-prepared films from target status II. The thickness of SP578 is 41.91±0.4nm as calculated before. For SP601 and SP603, the thickness is estimated from the growth time to be ca. 200nm.

The XRR data is shown in **Figure 4.11(a)**. The Kissig oscillations of the thick films disappeared. Two potential reasons can induce this phenomenon. When measuring XRR, the incident angle is only ca. 1°. This will lead to a long path of the beam 2 (see figure) and thus to a strong absorption as shown in Figure **4.11(b)**. The absorption is increased from 49.2% in the 40nm film to 96.5% in the 200nm film. Moreover, the spacing of the Kissig oscillations of a 200nm film can be calculated using **Equation 2-32** to be only ca. 0.003Å which is basically impossible to be resolved.
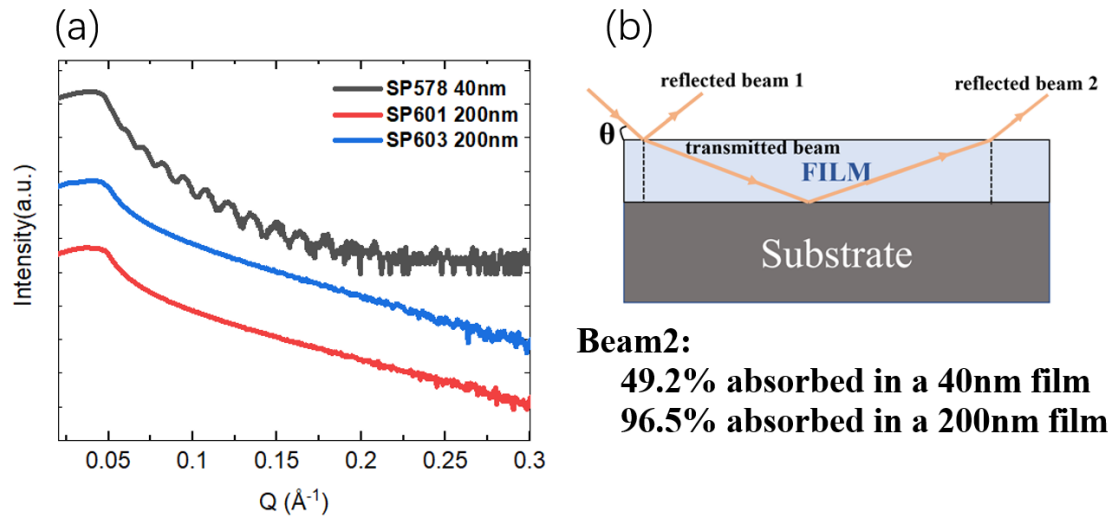
Figure 4.11 (a) XRR patterns of the as-prepared SP578, SP601 and SP603. (b) Schematic diagram of reflection and refraction at the film surface and interface. The absorption of beam 2 is listed for different film thicknesses.

4.2.1.2 Magnetic behavior

The magnetic behavior of SP601 is investigated via SQUID magnetometry. **Figure 4.12** illustrates the FC curve measured at 10mT. A surprising reduction of T_C from 326.6±1K in the 40nm film to 287.5±1K in this 200nm film is observed. The reduced T_C indicates a weaker double-exchange interaction. One might assume that the 200nm film exhibits a poor crystallinity thus leading to a weaker long-range magnetic ordering. Moreover, a film off-stoichiometry can influence the Mn oxidation state resulting in different exchange interactions and hence lead to a different T_C.

Subsequent investigations of the target itself lead to the conclusion that the target stoichiometry is incorrect (see also below).
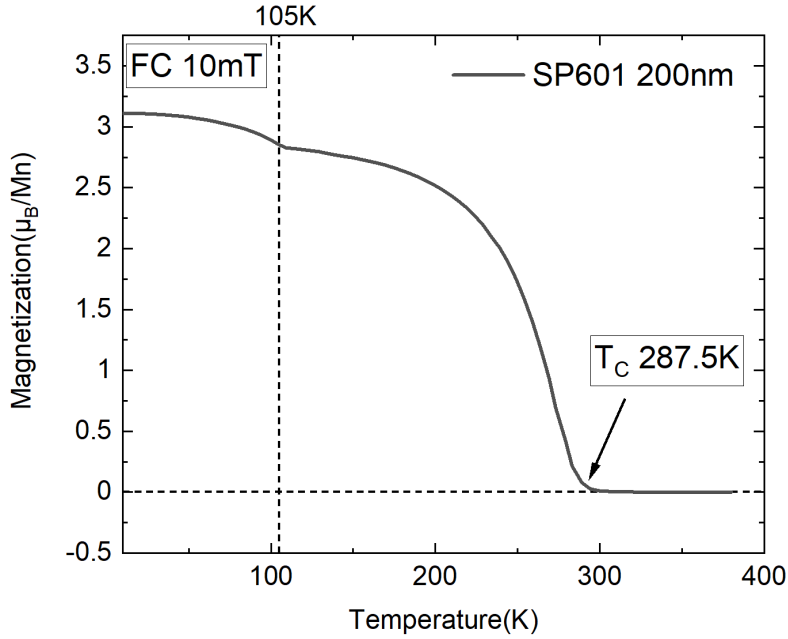
Figure 4.12 FC curve of the as-prepared SP601, measured at 10mT.

4.2.3 Reciprocal space mapping

In order to determine the strain status of the as-prepared films RSM is employed. The (103) lattice plane is probed and the corresponding in-plane and out-plane lattice parameters are calculated. SP578 and SP601 are grown to obtain different film thicknesses. Because these samples are intensively involved in the following post-treatments, these were chosen for RSM characterization as shown in **Figure 4.13**. SP578 with a thickness of ca. 40nm shows the same in-plane parameter as the STO substrate which is ca. 3.9Å. This indicates that the film is grown epitaxially fully strained on the substrate. In the out-of-plane direction, the calculated parameter 3.85Å corresponds well with the results obtained using XRD. Compared with the LSMO bulk value 3.88 Å, the results imply a tensile strain in the film in-plane direction while a compressive strain in the out-of-plane direction. However, the (103) peak of SP601 with a thickness of ca. 200nm shifts to lower values in both directions which reveals that the strain is partially relaxed.
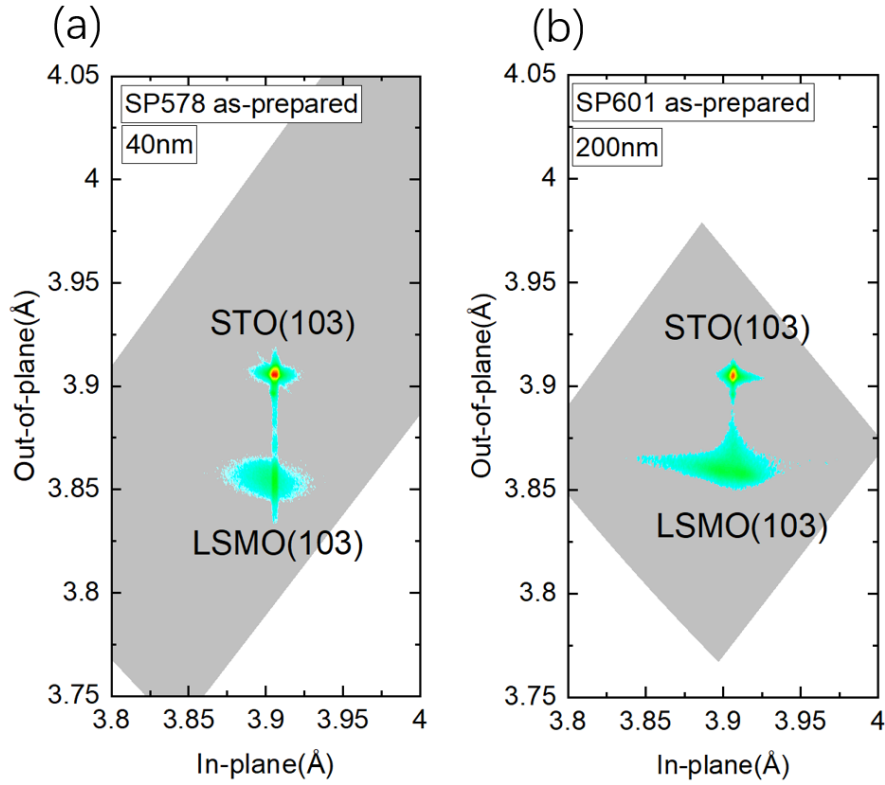
Figure 4.13 Reciprocal space mapping of the as-prepared film, where the (103) lattice plane is probed. (a) SP578 with a thickness of ca. 40nm. (b) SP601 with a thickness of ca. 200nm.

4.2.4 Stoichiometry

The stoichiometry of SP578 and SP601 is determined via RBS. The results are illustrated in **Figure 4.14**. The kinetic energy of the backscattered ions decreases when atoms are either located at a deeper position of the film or has a lower mass of nucleus. Hence, the film La peak appears at the highest energy, followed by the film Sr peak, and then the film Mn peak. Moreover, the elemental contributions from the substrate are mixed in the signal, thus a fitting by a software using a model is required in order to calculate the film stoichiometry. Furthermore, the width of the film peak is positively correlated with the film thickness. The shape of a peak can be used to evaluate the elemental distribution inside the film.

The stoichiometry of the as-prepared SP578 is calculated to be $La_{0.64}Sr_{0.26}Mn_{0.857}O_{3.25}$. However, RBS exhibits a poor accuracy for light elements, e.g. oxygen, and thus only the ratio between La, Sr and Mn is presented in the following text. Since La and Sr occupy the A-sites in ABO_3 perovskite structure the sum of La and Sr is normalized to 1 for a better comparison, i.e. $La_{1-x}Sr_xMn_y$. Then for SP578, the stoichiometry is $La_{0.71}Sr_{0.29}Mn_{0.95}$, which is almost

unchanged compared to the expected one, while Mn is slightly deficient. For SP601, which exhibits a larger thickness of ca. 200nm, the stoichiometry is determined to be $La_{0.75}Sr_{0.25}Mn_{0.83}$. This result implies a strong Mn deficiency in film and a wrong La to Sr ratio which is different to the desired one. A multisystem can be employed to explain the Mn deficiency in the as-prepared films, e.g. a system contains $La_{1-x}Sr_xMnO_3$, La_2O_3 and SrO. The results are shown in **Table 4.5**. The a, b and c refer to the estimated portion of each subsystem. δ denotes the deviation of oxygen stoichiometry during sample growth.

The wrong stoichiometry of SP601 is due to a wrong stoichiometry of the sputtering target, i.e. the new target in the status II, which has been very recently confirmed by EDX studies on the sputter target with the help of Mr. Friedrich at the institute PGI-7. The target stoichiometry has been determined to be $La_{0.78}Sr_{0.22}Mn_{0.92}$. This stoichiometry leads as expected to a reduced T_C as observed in **Chapter 4.2.1.2**.
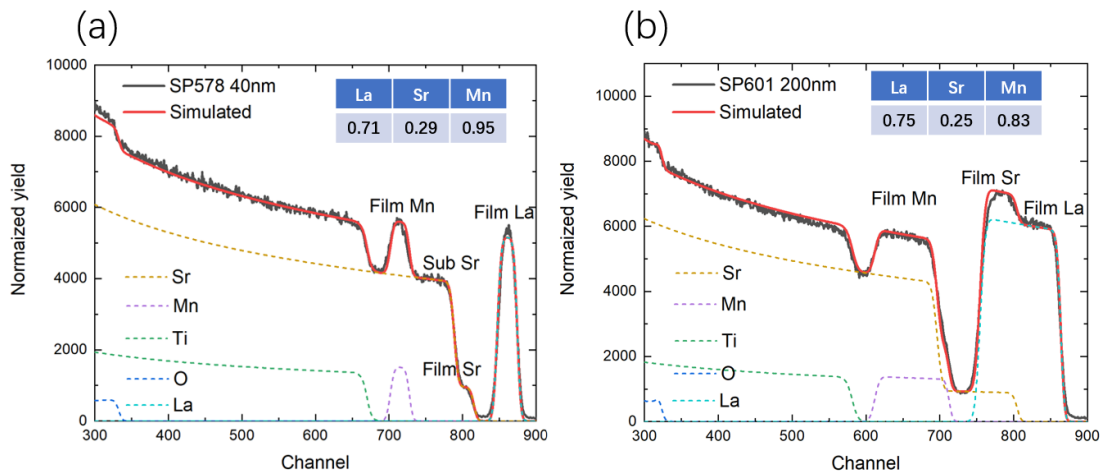

Figure 4.14 RBS spectrum of as-prepared SP578 and SP601. The individual element contribution curves are shown with dotted lines. The data is fitted via the software SIMNRA. Results are inserted as tables in the figure.

Table 4.5 Estimated composition of the as-prepared film SP578 and SP601.

	SP578	SP601
RBS data	$La_{0.71}Sr_{0.29}Mn_{0.95}O_{3-\delta}$	$La_{0.75}Sr_{0.25}Mn_{0.83}O_{3-\delta}$
a $La_{1-x}Sr_xMnO_3$	$0.95\ La_{2.11\delta+0.54}Sr_{0.46-2.11\delta}MnO_3$	$0.83\ La_{2.41\delta+0.08}Sr_{0.92-2.41\delta}MnO_3$
b La_2O_3	$(0.1-\delta)\ La_2O_3$	$(0.34-\delta)\ La_2O_3$
c SrO	$(2\delta-0.15)\ SrO$	$(2\delta-0.51)\ SrO$
δ range	$0.075 \leq \delta \leq 0.1$	$0.26 \leq \delta \leq 0.34$

4.3 Summary

In this chapter, we demonstrate the successful sample growth of LSMO film via HOPSD. The as-prepared films with a thickness of ca. 40nm exhibit a very good crystallinity when using the previously optimized growth parameters, characterized by XRR and XRD. No significant structural difference was found when growing films on STO and on Nb-STO substrates. The 40nm films were evidenced by RSM to be grown epitaxially fully strained on the substrate. The film stoichiometry was confirmed by RBS to be almost the desired ratio i.e. $La_{0.7}Sr_{0.3}Mn_1$.

Moreover, the influence of growth temperature onto film physical properties are investigated. The films grown at different temperatures, i.e. 700°C, 800°C and 900°C, were verified by XRD to show a similar out-of-plane lattice parameter of 3.85Å, while different magnetic properties were found via SQUID magnetometry. 800°C is demonstrated to be best growth temperature due to the highest T_C and the largest M_s.

In addition, "thick" films were successfully prepared by extending the sputtering time. A thickness of 200nm is estimated. We demonstrate an increased intensity of Bragg peak in XRD scans, which might enable a larger signal for neutron diffraction. The thick films were found via RSM to show a partial strain relaxation. During the sample preparation of thick films, the new target was evidenced by EDX to have an incorrect stoichiometry which could result in the reduced T_C and the film off-stoichiometry, as observed via SQUID magnetometry and via RBS, respectively.

5. Control of physical properties via topotactic phase transition on LSMO thin films and powder by post-annealing

In this chapter, the studies on Aluminum (Al)-assisted vacuum annealing on LSMO films and on LSMO powder are discussed. We demonstrate that Al-assisted vacuum annealing can constitute an optimized way to trigger the topotactic PV to BM phase transition as demonstrated on 40nm and 200nm thick LSMO films as well as on ball-milled LSMO powder samples. The lattice structural variation during the phase transition is systematically investigated by XRD.

Additionally, RSM is employed to identify the strain state of the films. The film topography and thickness information are collected by AFM and XRR. The oxygen vacancy induced change of the magnetic and electrical transport properties are characterized using a SQUID magnetometer and a PPMS device. Moreover, the film stoichiometry during the phase transition is determined based on RBS measurements. Furthermore, XAS is employed to probe the ionic oxidation states at different topotactic states. Here I also will summarize results using neutron diffraction on thin films, which unfortunately gave only a partial success. Besides the strained thin film system, the stoichiometry, lattice structure and magnetic behavior of strain-free bulk-like powder samples are investigated by ICP-OES, powder XRD and SQUID magnetometry.

5.1 Motivation

Previously, the PV-BM phase transition in LSMO film was realized by Dr. Lei Cao and Hengbo Zhang using thermal vacuum annealing. However, either high temperatures such as 750°C or long annealing times such as 62h were required [10,11,12]. In this chapter, I will describe the usage of Al as oxygen getter material to optimize the annealing conditions and to provide the future possibility for detailed in-situ studies, e.g. in-situ XAS, in-situ polarized neutron reflectometry or in-situ neutron diffraction.

Al-assisted vacuum annealing was previously preliminary investigated by Hengbo Zhang. However, the BM phase was not achieved. In my work, this assisted annealing was further investigated, several measures have been used for improvement as described below. It was found that a high-efficiency topotactic phase transition from PV to BM can actually be realized via this method. Moreover, Al-assisted vacuum annealing is also employed on the bulk-powder system for comparison. Here I also succeeded to trigger the PV to BM phase transition and hence provided the possibility for future powder neutron diffraction studies. Neutron diffraction is necessary for probing the spin structure variation and in particular during the phase transition. In addition, the investigation of the role of strain during the phase transition is of high importance.

5.2 Al-assisted vacuum annealing on LSMO thin films

In this chapter, the Al-assisted vacuum annealing on LSMO thin films is described. The annealing is accomplished using a sealed vacuum tube.

5.2.1 Al-assisted vacuum annealing method

The experimental configuration is illustrated in **Figure 5.1**. Nr.60060 Al-foil is polished by sandpaper P400 to remove the surface oxide layer. A bare Al surface will passivate itself and form ca. 3nm thick surface Al oxide layer according to the chemical reaction: $4Al + 3O_2 \rightarrow 2Al_2O_3$ on the time scale of 24h as mentioned in Ref [53]. In this sense a bare Al surface can act as an efficient oxygen getter material.

In this study freshly polished Al-foil is immediately sealed together with the film in a quartz tube and evacuated to $10^{-5} \sim 10^{-6}$ mbar with the help of ZEA-1. Afterwards, the sealed vacuum tubes are heated in a temperature-controlled furnace.
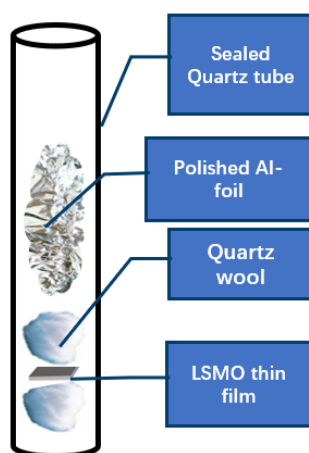

Figure 5.1 Experimental configuration of Al-assisted vacuum annealing for LSMO thin films. Quartz wool is used to avoid a direct contact of the film and the Al-foil.

During the annealing process, the tube is heated to $350 \sim 550°C$. The Al can be used as oxygen getter until the growing Al oxide layer reaches ca. 200nm [54]. A quantification of this getter effect is unfortunately not easily possible and might be a subject for future studies.

During this getter process oxygen vacancies are introduced near the film surface via the reaction: $2O_O(\text{nearsurface}) \rightarrow 2\,V_O^{\cdot\cdot} + O_2(\text{gas}) + 4e'$. The oxygen molecules are hereby desorbed from

the film due to the reduced oxygen partial pressure as a result of the getter process. The thus introduced oxygen vacancies enable oxygen bulk diffusion in the film. The bulk diffusion coefficient of oxygen in LSMO is reported to be ca. $10^{-17}\mathrm{cm}^2\mathrm{s}^{-1}$ at 600°C [55]. The oxygen desorption process can be promoted via either a lower oxygen partial pressure or an increased temperature.

5.2.2 Sample growth and annealing parameters

The sample growth and annealing information is shown in **Table 5.1** and **Table 5.2**. SP578 exhibits a thickness of 41.91±0.4nm. As mentioned in **Chapter 4**, the thickness of SP601 and SP603 is estimated to be ca. 200nm according to the growth time. In the following, the label "40nm" and "200nm" are used to represent the above-mentioned thicknesses.

After preparation, the samples are divided into 4 segments, labeled by -1, -2, -3, and -4. The 40nm films SP578-1 and SP578-2 have a size of ca. 5mm×5mm which can be loaded into the quartz tube with an inner diameter of 1.4cm and a length of 17cm. The tube volume is thus 104.7cm^3. Ca. 0.5g of Al in the form of regular Al foil is used. The 200nm films, i.e. SP601 and SP603, are grown and annealed for the preparation for neutron diffraction which requires a film size of 10mm×10mm. Thus, a tube with an inner diameter of 2.4cm and a length of 12cm is used. The tube volume is 217.1cm^3 . The corresponding Al mass is increased to ca. 1.0g.

Table 5.1 Sample information involved in **Chapter 5.2**.

Sample ID	Sputter target status	Growth temperature [°C]	Oxygen pressure [mbar]	Plasma power [W]	Growth time [min]	Estimated thickness [nm]
SP578	Status I	800	2	120	60	41.91±0.4
SP601	Status II	800	2	120	300	ca. 200
SP603	Status II	800	2	120	300	ca. 200

Table 5.2 Al-assisted vacuum annealing parameters involved in **Chapter 5.2**.

Sample ID	Al-content [g]	Tube volume [cm^3]	Vacuum level [mbar]	Annealing temperature [°C]	Annealing time [hour]

SP578-1	0.5	104.7	1×10^{-5}	350	12
SP578-2	0.5	104.7	1×10^{-5}	400	12
SP601-2	1.0	217.1	5×10^{-6}	400	6
SP601-3	1.0	217.1	5×10^{-6}	400	12
SP601-4	1.0	217.1	5×10^{-6}	450	12
SP603	1.0	217.1	5×10^{-6}	450	15

5.2.3 Annealing condition dependent structural changes

For the 40nm films SP578 series, the annealing time was fixed to 12h. Three different annealing temperatures 350°C, 400°C and 450°C were chosen for investigation (**Figure 5.2 (a)**). The 350°C annealing results in left-shifted Bragg peaks with no new peaks emerging (see **Figure 5.2 (b)**). This indicates an expanded PV phase with an out-of-plane parameter of 3.934Å. The PV phase under expansion is defined as "E-PV" phase as used in the following text. When assuming the film is still fully strained, then the oxygen-loss induced lattice expansion can be directly estimated via the change of the out-of-plane lattice parameter being 2.2%. When oxygen vacancies are generated via annealing, the Mn oxidation state is reduced and thus a larger Mn ion radius results.

After annealing at 400°C, a BM phase with an out-of-plane parameter of 16.461Å is achieved. The wide-range XRD plot is shown in **Figure 5.2 (b).** The thus obtained BM-LSMO exhibits weak superlattice peaks indicating a poor quality of the BM phase. However, the results show that a PV-BM phase transition can be successfully triggered via Al-assisted vacuum annealing, which has been considered as impossible in a previous study [12].
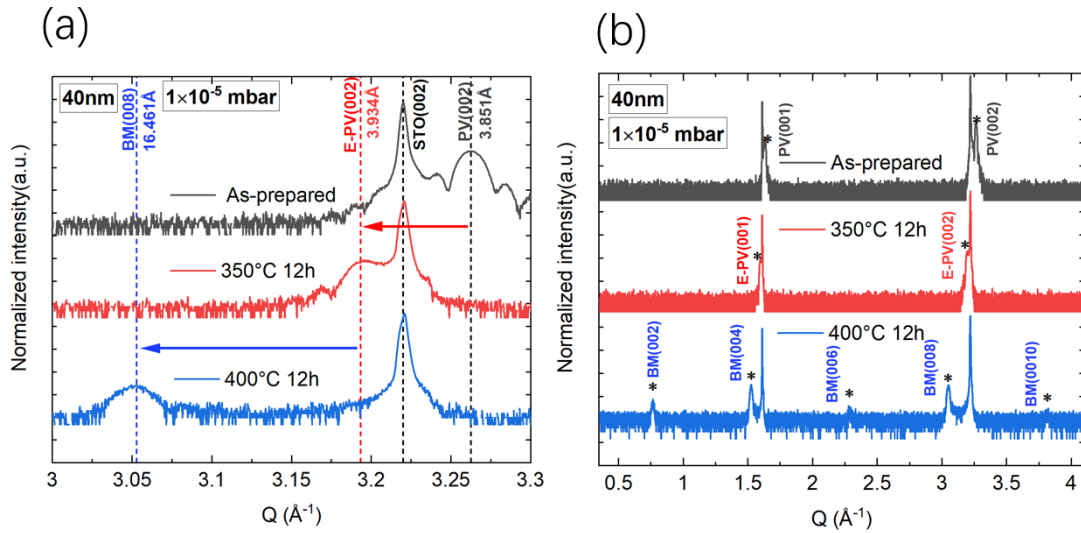
Figure 5.2 XRD pattern of the 40nm as-prepared and annealed films (SP578 series). (a) XRD scans in the $Q(Q_z)$ range 3Å^{-1} to 3.3Å^{-1}. (b) XRD scans in a broader Q range. Film peaks are marked with stars.

For neutron diffraction, more material is required for a sufficiently large signal. Hence thicker films were prepared. Firstly, sample SP601 with a thickness of ca. 200nm is employed to explore the optimal annealing parameters for a "thick" film. Considering that the increased thickness might hinder the film oxygen desorption process leading to a lower transformation speed, the vacuum is improved from 1×10^{-5} mbar to 5×10^{-6} mbar. The film SP601-2 annealed at 400°C for 6h shows a mixed state (**Figure 5.3 (a)**). According to the previous work of Dr. Lei Cao, one can attribute this mixed state to be a E-PV phase mixed with an intermediate phase [10,11]. However, the superlattice peaks of the intermediate phase are weak which might indicate that this phase is on the verge to form a homogeneous lattice (**Figure 5.3 (b)**). When extending the annealing time to 12h, the peak position stays almost unchanged. In addition, the peak intensity of the intermediate phase is increased, and the peak intensity of the E-PV phase is reduced (see blue arrows in **Figure 5.3 (a)**). Additionally, strong superlattice peaks emerge (**Figure 5.3 (b)**). This implies a partial transformation from the E-PV phase to the intermediate phase. One can assume that the PV phase already reaches the expansion maximum which is 3.965 Å (2.6%). In this state, oxygen vacancies are randomly arranged in the film thus leading to a high internal energy. Subsequently, the accumulated internal energy promotes oxygen vacancies to form ordered structures, i.e. alternating layers of oxygen octahedra (O) and tetrahedra (T). For the alternating O and T structures, the neighboring T sheets show different

orientations thus increasing the lattice periodicity from 1 unit cell to 4 unit cells thus forming a superlattice as illustrated in **Figure 5.4**. However, this intermediate phase exhibits a non-centered structure, which allows the observation of both odd and even superlattice peaks.

Upon changing the annealing temperature to 450°C, the final lattice parameter is increased from 16.152 Å to 16.448 Å. Odd superlattice peaks are forbidden at the higher symmetry being a clear fingerprint for a BM-LSMO. For the 200nm thick SP601 series, the BM phase is achieved when annealed at a larger temperature of 450 °C and at a better vacuum compared to the 40nm thick SP578 series.
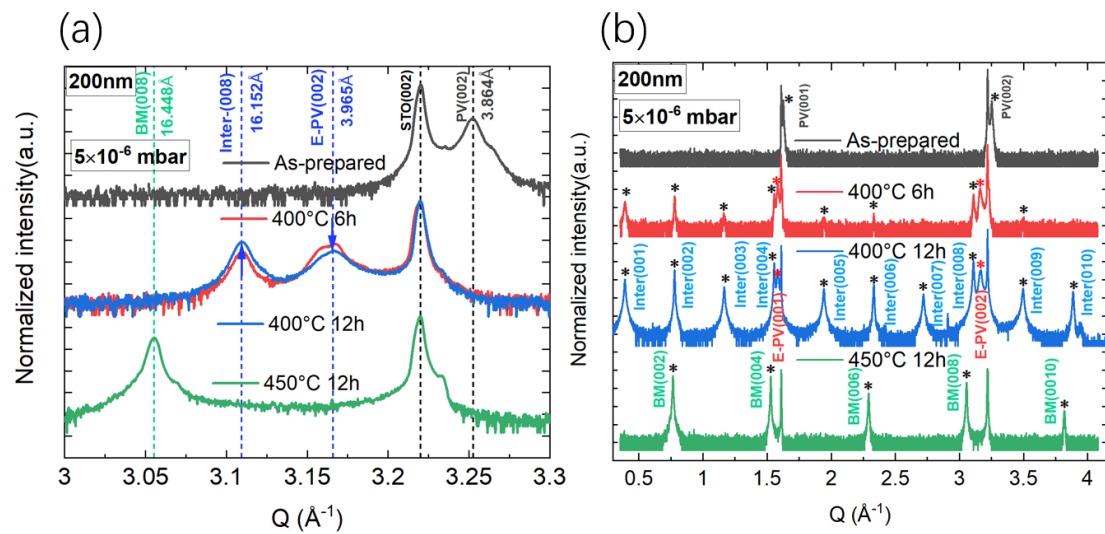

Figure 5.3 XRD pattern of the 200nm as-prepared and annealed films, i.e. SP601 series. (a) XRD scans in the Q range 3Å^{-1} to $3.3\ \text{Å}^{-1}$. (b) XRD scans in a broader Q range. Film peaks are marked with stars.
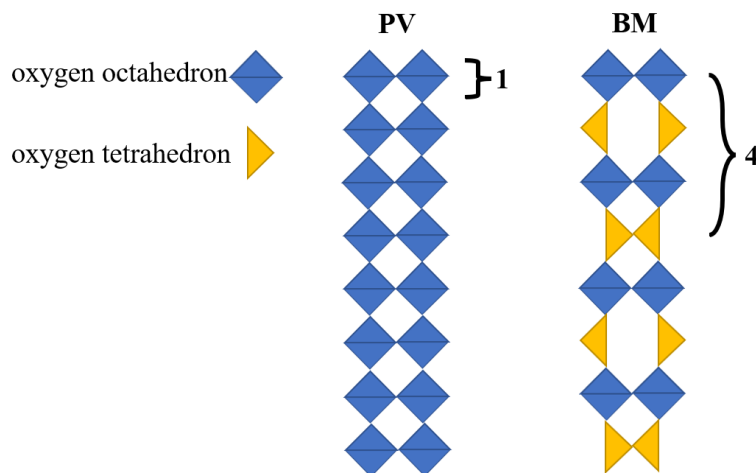

Figure 5.4 Lattice schematics of the as-prepared PV phase and the topotactic BM phase.

To ensure the consistency of samples in subsequent measurements, the stability of annealed films in air is investigated as shown in **Figure 5.5**. For the 350°C 12h annealed film, the lattice structure varies continuously during half a year as shown in **Figure 5.5 (a)**. The right-shifted (002) peak implies that lattice expansion is reduced, which can be attributed to the oxygen reabsorption. However, one finds that the film (002) peak position of the 40nm and 200nm thick BM-LSMO (**Figure 5.5 (b)** and **Figure 5.5 (d)**) stays unchanged. It means the system does not retake oxygen from air. This situation also applies to the 200nm thick film with mixed states (**Figure 5.5 (c)**). One can assume that, once the oxygen vacancy rearranging process is triggered, the re-oxygenation in air is inhibited.
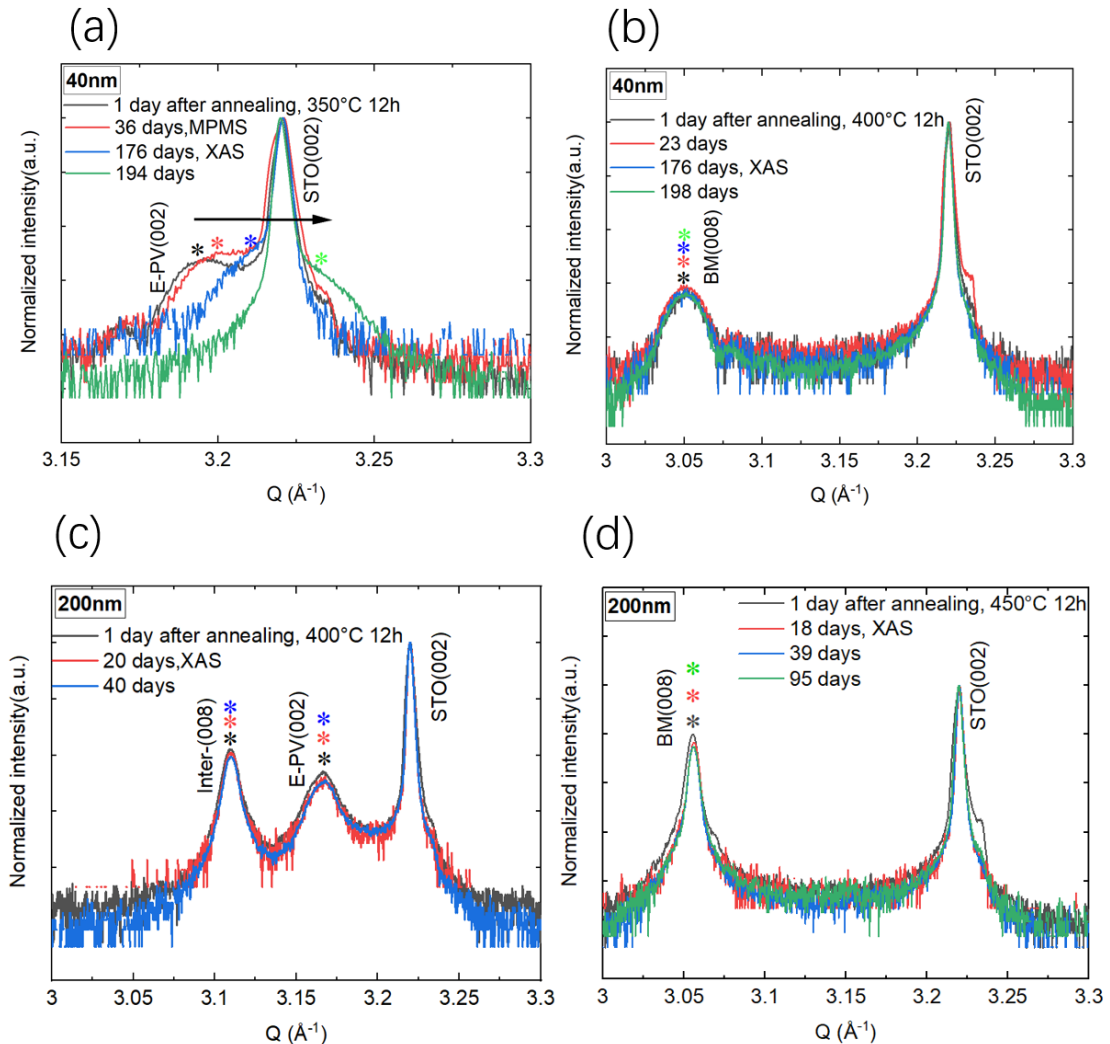

Figure 5.5 XRD pattern of the 40nm and 200nm thick annealed films, i.e. SP578 and SP601 series, measured after air exposure for different times. (a) 40nm film SP578-1 annealed at 350°C for 12h. (b) 40nm film SP578-2 annealed at 400°C for 12h. (c) 200nm film SP601-3

annealed at 400°C for 12h. (d) 200nm film SP601-4 annealed at 450°C for 12h. Film peaks are marked with stars.

5.2.4 Surface and morphology changes

The thickness as well as roughness information of the 40nm SP578 series is collected by XRR as illustrated in **Figure 5.6** and **Table 5.3**. As mentioned before, for the 200nm thick SP601 series one cannot apply any meaningful XRR fitting due to the lack of Kissig oscillations.

For the as-prepared SP578 and the 350°C 12h annealed SP578-1 (E-PV), the three-layer model as mentioned in **Chapter 4** is used for fitting. The results indicate a reduction of both SLD and film thickness. However, for the 400°C 12h annealed SP578-2 (BM), the previous model failed to fit the curve. Hence, a four-layer model involving a top layer, two LSMO layers and a bottom layer is employed. SLD is fitted to be further decreased to $(3.641 \pm 0.04) \times 10^{-5} \text{Å}^{-2}$ for SP578-2 (BM). This 21.5% SLD reduction is larger than the theoretical PV to BM SLD reduction value, i.e. 10.2%, which implies a film decomposition. In perovskites, an excess of oxygen vacancies can lead to a breakdown of the crystal structure.

AFM is used to probe the film surface as shown in **Figure 5.7**. The as-prepared films show either small or large surface islands. These islands can undergo a fast oxygen desorption during annealing due to the large specific surface area thus leading to an enhanced structural decomposition. Hence, the surface becomes flattened resulting in a reduced roughness. With increasing the annealing temperature, the surface begins to break into regions forming large depressions.
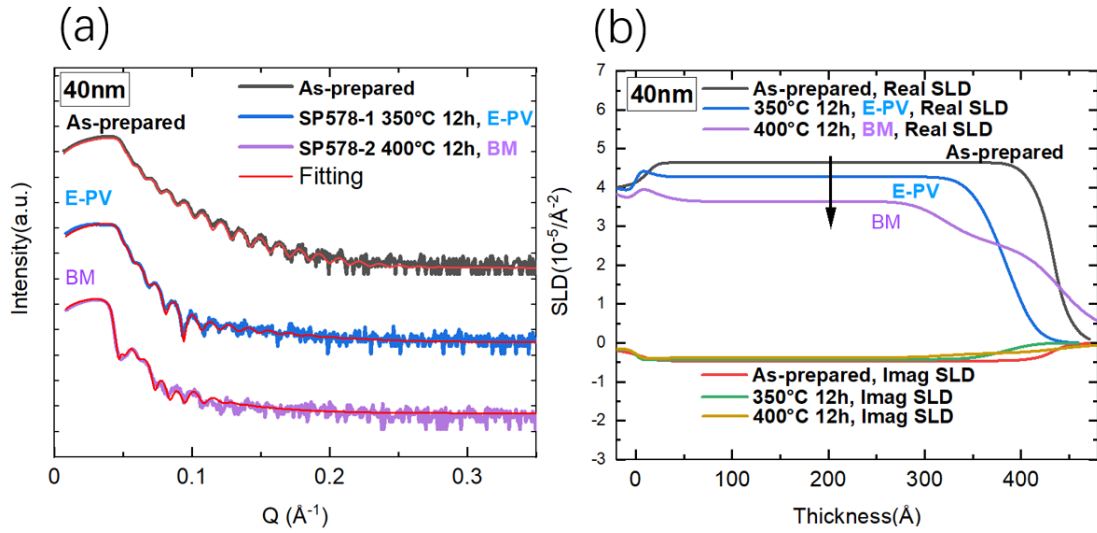
Figure 5.6 (a) Fitted XRR pattern of the as-prepared state of SP578, 350°C 12h annealed SP578-1 and 400°C 12h annealed SP578-2. (b) Corresponding calculated SLD. Fitted by the software GenX.

Table 5.3 Calculated data from XRR measurements.

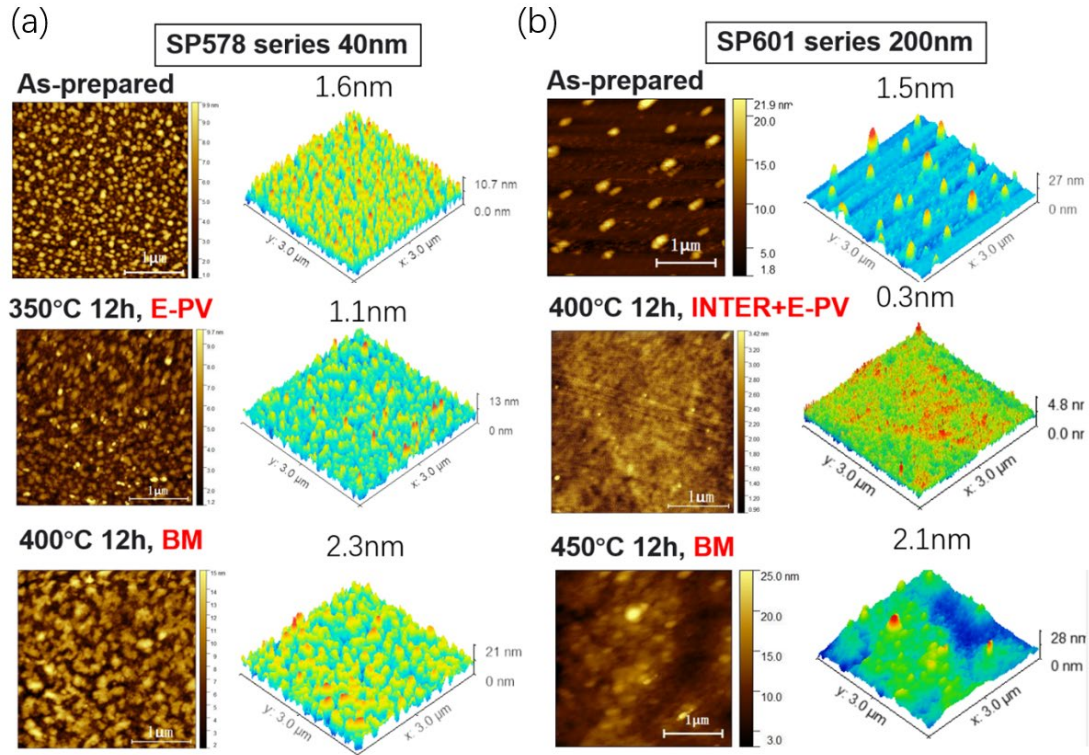| Sample ID	Sample state	Surface roughness [nm]	LSMO 1st layer thickness [nm]	LSMO 1st layer SLD [$10^{-5}Å^{-2}$]	LSMO 2sec layer thickness [Å]	LSMO 2sec layer SLD [$10^{-5}Å^{-2}$]
SP578	As-prepared	2.06±0.02	41.91±0.4	4.639±0.05		
SP578-1	E-PV	2.61±0.02	37.52±0.4	4.276±0.04		
SP578-2	BM	2.25±0.02	12.14±0.1	2.799±0.03	31.54±0.3	3.641±0.04

Figure 5.7 AFM measurements of the as-prepared and annealed films. (a) 2D and 3D surface morphology of the SP578 series, respectively. (b) 2D and 3D surface morphology of the SP601series, respectively.

5.2.5 Magnetometry measurements

The zero-field cooling (ZFC) and field cooling (FC) curves of SP578 and SP601 series are displayed in **Figure 5.8**. For the E-PV phase of 40nm SP578-1 a typical antiferromagnetic behavior with a Néel-temperature of 45.5K is observed, while for the mixed state of the 200nm SP601-3, an antiferromagnetic state with reduced Néel-temperature of ca. 30K appears. During annealing, the resulting oxygen vacancies can lower the oxidation state of Mn and lead to a lattice expansion, which will suppress the double-exchange interactions and result in antiferromagnetism via superexchange interactions between the Mn ions. Moreover, super-exchange can act among Mn^{2+} or among Mn^{3+}. These different superexchange interactions can yield different mean field strength in the sublattice thus diverse Néel-temperatures, i.e. Mn^{3+} can lead to a stronger antiferromagnetism thus a higher Néel-temperature.

Interestingly, the 40nm and 200nm BM-LSMO films show in the FC and ZFC curves a possible peak above room temperature. This might be a sign for a new type of magnetic structure (**Figure**

5.9). The "oscillations" in **Figure 5.9** exhibit a signal variation of ca. $5 \times 10^{-10} Am^2$ which is very close to the instrument sensitivity, i.e. $10^{-11} Am^2$ and hence attributed to instrument noise.
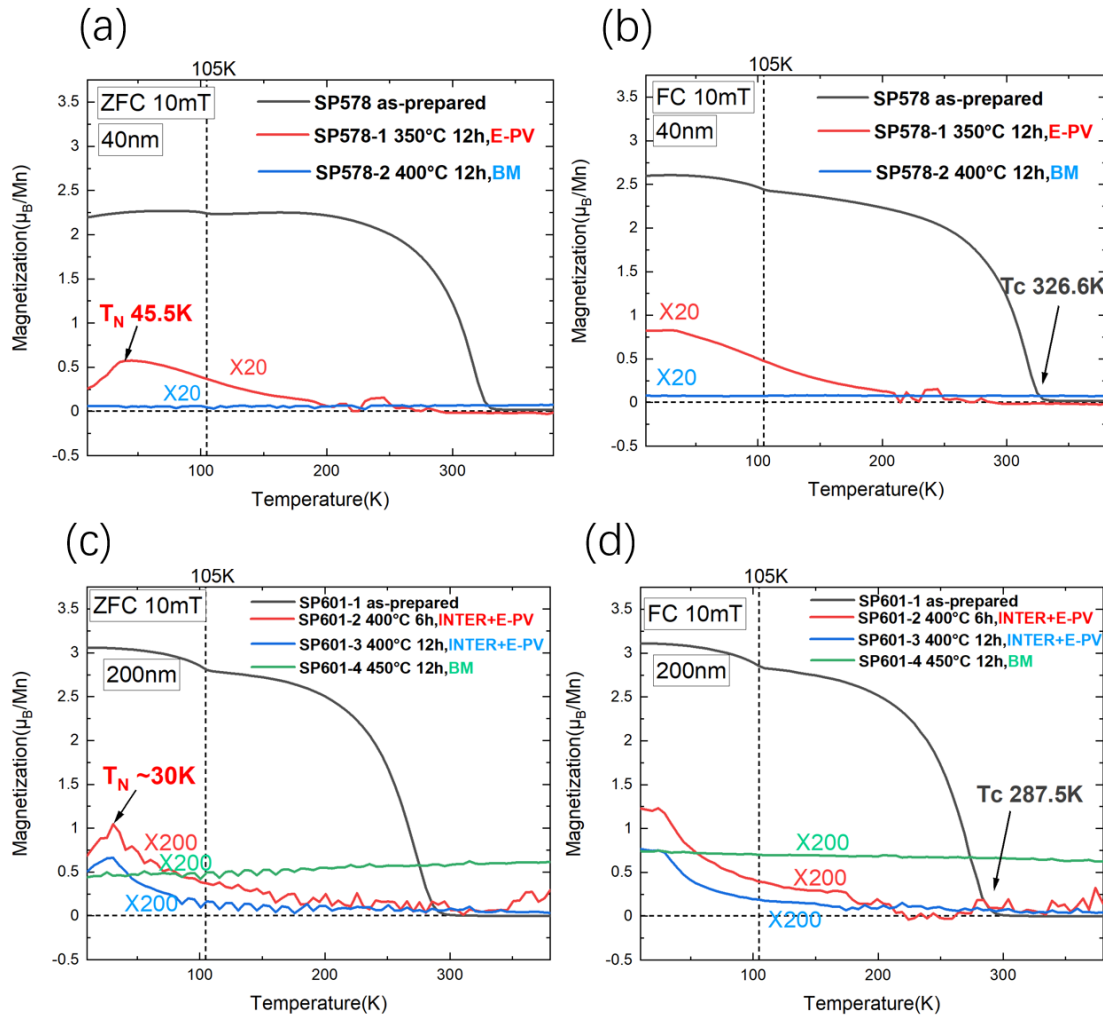

Figure 5.8 Magnetization vs. temperature ZFC and FC curves of the SP578 and SP601 sample series, measured at 10mT. (a), (b) ZFC and FC curves of the SP578 series. The data of the annealed samples (SP578-1 and SP578-2) is enhanced by a factor of 20. (c), (d) ZFC and FC curves of the SP601 series. The data of the annealed samples (SP601-2, SP601-3 and SP601-4) is enhanced by a factor of 200.
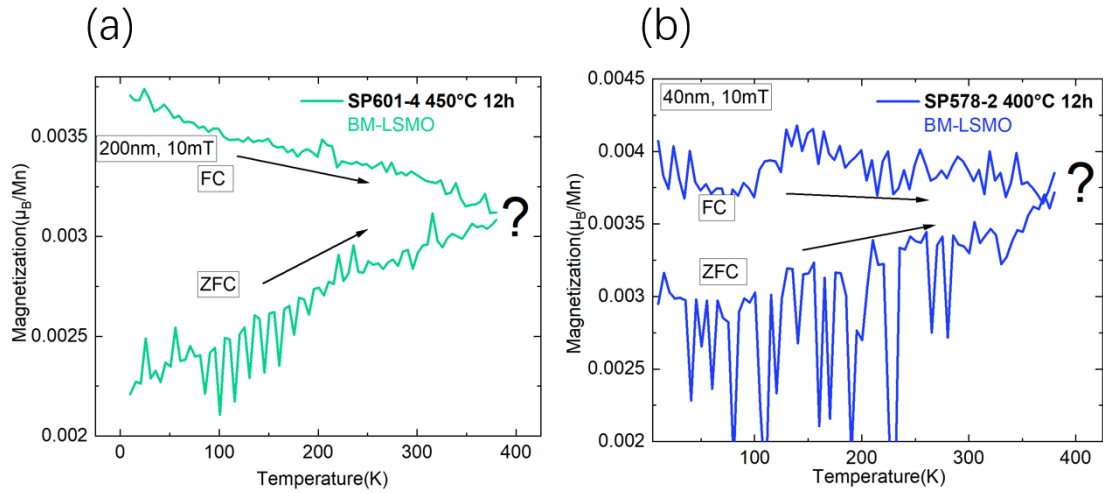
Figure 5.9 (a) ZFC and FC curves of the 40nm BM-LSMO sample (SP578-2). (b) ZFC and FC curves of the 200nm BM-LSMO sample (SP601-4).

5.2.6 Resistivity measurements

The electrical transport properties of the thin films are characterized via the van der Pauw method using the PPMS device. The results are shown in **Figure 5.10**. The as-prepared state of the 40nm SP578 and 200nm SP601 film exhibits as expected a metal to insulator transition around T_C (326.6 K and 287.5 K). For the 40nm film in the E-PV state (SP578-1) and the 200nm film (SP601-3), being in the mixed state, the resistivity at room temperature is enhanced by three to four orders of magnitude compared with the as-prepared state. This can be explained by the induced changes in the exchange interactions. For the as-prepared state, the double-exchange enables hopping of Mn 3d electrons and thus a net charge transfer and hence a metallic behavior. However, for the antiferromagnetic E-PV phase and the mixed phase, the superexchange interactions only allow O 2p electrons being delocalized among neighboring Mn ions. This leads to insulating behavior.
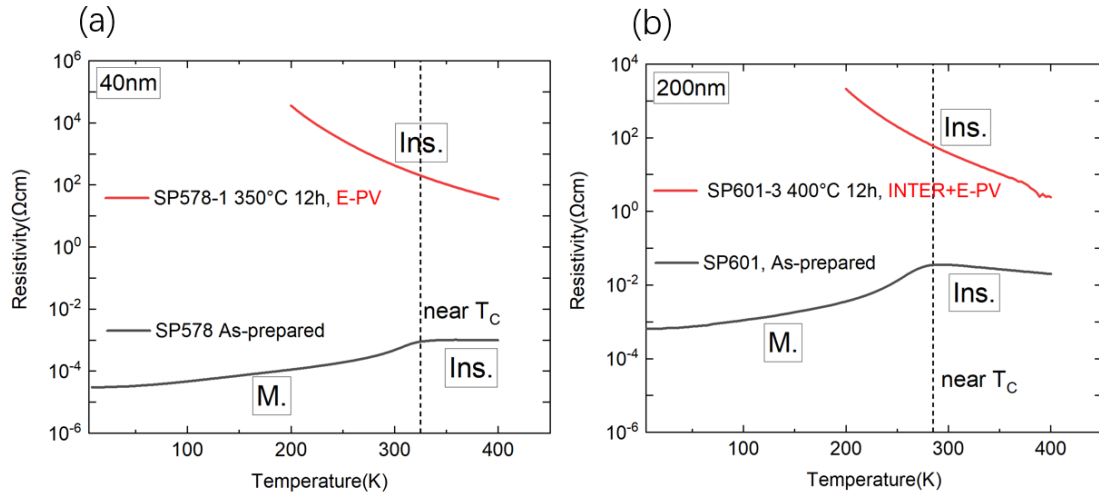
Figure 5.10 (a) Resistivity vs. temperature of the as-prepared and the annealed 40nm film, i.e. SP578 as-prepared and SP578-1. (b) Resistivity vs. temperature of the as-prepared and annealed 200nm film, i.e. SP601 as-prepared and SP601-3.

5.2.7 X-ray Absorption Spectroscopy

High resolution XAS enables the characterization of ion oxidation states. The results are shown in **Figure 5.11**. From the peak positions and the line shapes, one can determine the ionic oxidation states. For both 40nm SP578 and 200nm SP601 as-prepared and annealed samples, the oxidation state of La stays at La^{3+} (**Figure 5.11 (a) and (b)**). The oxidation state of Mn can be probed via the Mn $L_{2,3}$-edge (**Figure 5.11(c) and (d)**). For the as-prepared 40nm and 200nm film, according to the L_3-edge peak position (see green arrow), one can conclude that Mn^{3+} and Mn^{4+} coexist in the film. The ferromagnetic behavior of the as-prepared state can be attributed to the double-exchange interaction between Mn^{3+} and Mn^{4+}. For the E-PV 40nm film SP578-1 and the mixed-state 200nm film SP601-3, the contribution of Mn^{2+} starts to dominate. As demonstrated in **Chapter 5.2.5**, SP578-1 and SP601-3 exhibit antiferromagnetic behavior with different Néel-temperatures. The larger L_3 to L_2 branching ratio of SP601-3 indicates an increased amount of the high spin states and thus more Mn^{2+} [44,46]. This gives a hint that superexchange interactions among Mn^{3+} and among Mn^{2+} result in different Néel-temperatures. For the final 40nm and 200nm BM-LSMO, only the features of Mn^{2+} are observed. In **Figure 5.11(e) and (f)**, the O K-edge is highlighted. Considering different hybridizations, the spectrum can be divided into the following hybridization regions: i) O 2p orbitals hybridize with Mn 3d orbitals which appears between ca. 527eV and 533eV, ii) O 2p

orbitals hybridize with La 5d or Sr 4d orbitals between ca. 533eV and 538eV, iii) O 2p orbitals hybridize with Mn sp orbitals between ca. 538eV and 546eV. The electrons in O 1s orbitals can be exited to the conduction band via the hybrid orbitals between O 2p orbitals and metal ion orbitals thus forming O K-edge. The pre-edge spectrum (hybridization with Mn 3d orbitals) can be used to quantify the Mn 3d orbital occupancy state. For the 40nm film SP578 series and the 200nm film SP601series, after annealing, the intensity of the $e_g \uparrow$ peak decreases and of the $t_{2g} \downarrow$ peak increases. This indicates that more electrons exist in the Mn 3d orbitals compared with the as-prepared state, thus reflects a lower Mn oxidation state after annealing [47,56].
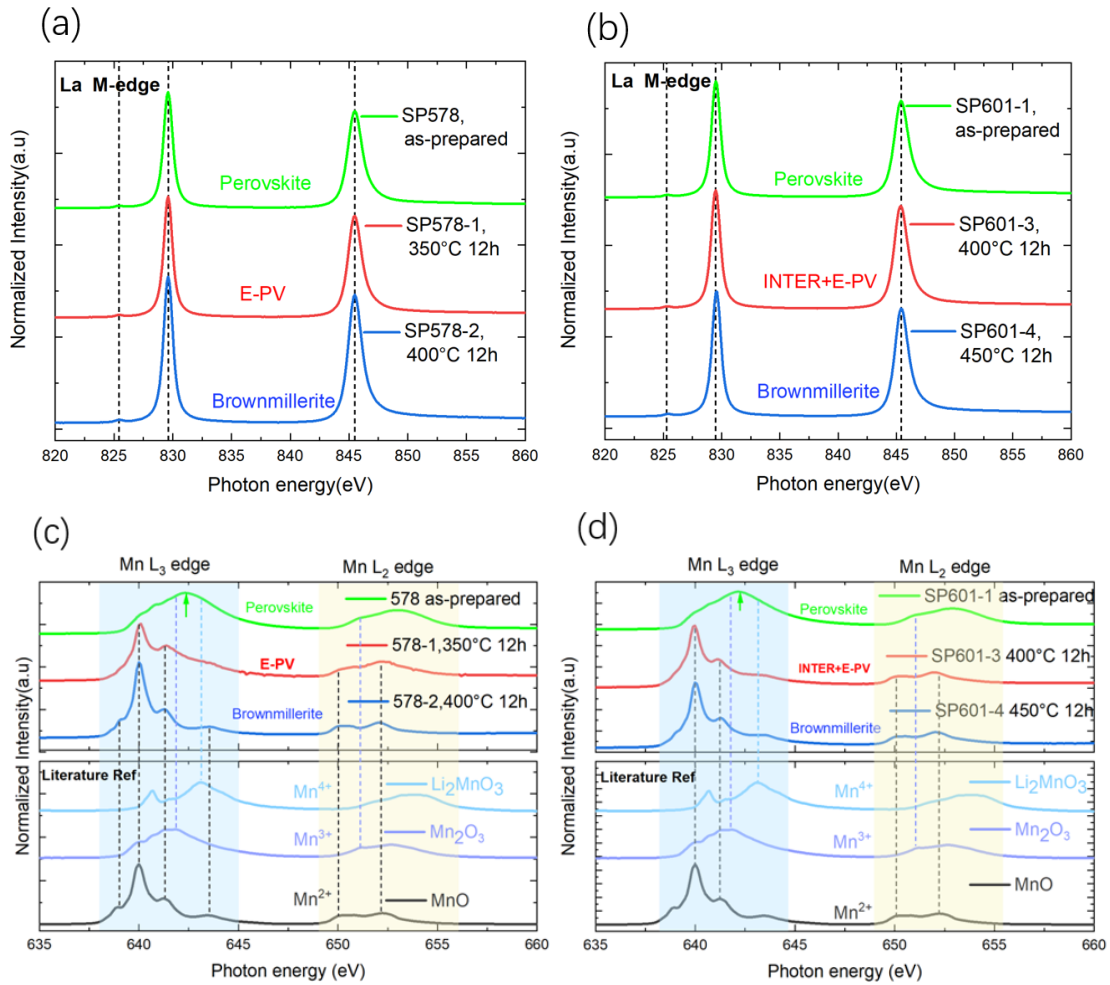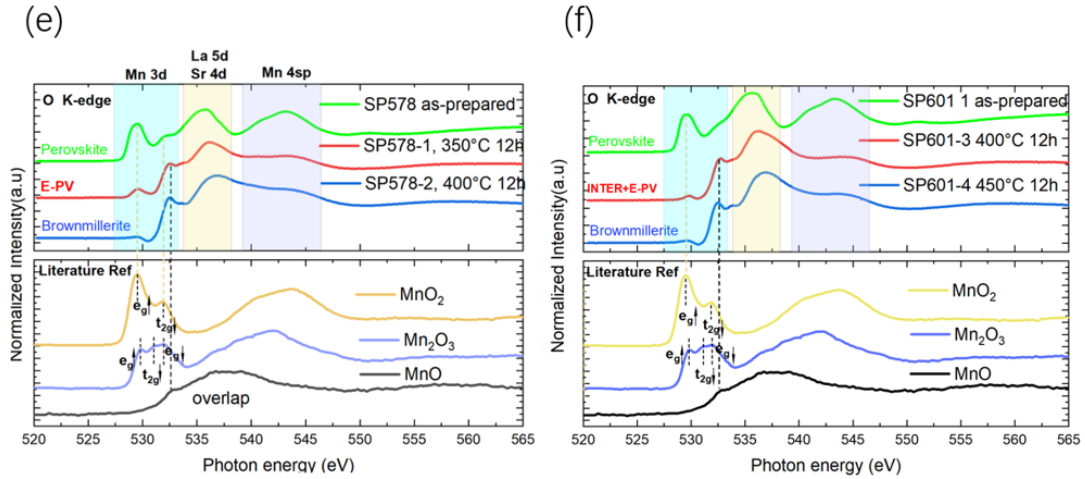
Figure 5.11 XAS spectra of the SP578 and SP601 sample series. (a), (b) Lanthanum M-edge. (c), (d) Manganese L-edge. (e), (f) Oxygen K-edge. Reference data from [45] and [46].

5.2.8 Stoichiometry characterization

RBS is measured to determine the film stoichiometry before and after annealing, as shown in **Figure 5.12**, **Table 5.4** and **Table 5.5**. Considering that RBS measurements exhibit poor accuracy when determining the stoichiometry of light elements, only the ratio of La : Sr : Mn is shown. The La + Sr is normalized to 1. For the SP578 series, the La to Sr ratio remains constant during annealing, i.e. 0.7:0.3. However, the Mn-content shows surprisingly a clear reduction from 0.95 to 0.75 and to 0.55. The change of the Mn-content is very likely due to an Mn desorption from the film and a simultaneous SrO and La_2O_3 segregation at the film surface [57]. In addition, more complex LSMO-phases might co-exist [56], but an exact determination of the relative ratio of composition is beyond the scope of this thesis and a topic for future studies.

For the mixed state 200nm film SP601-3, the spectrum curve is smeared out and cannot be fitted. One might attribute this smeared out behavior to the mixed state which contains different structures and thus different elemental concentrations. Moreover, SP601-4 (BM) also shows an almost constant La : Sr : Mn ratio after annealing compared with the as-prepared SP601. The deviated La : Sr ratio, i.e. 0.75:0.25, is due to the target problem as mentioned in **Chapter 4**.
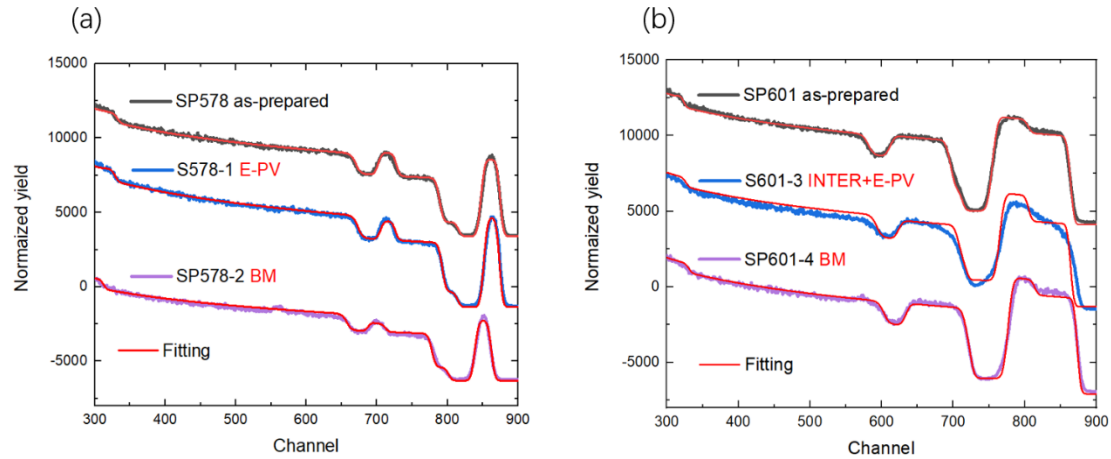
Figure 5.12 (a) RBS spectrum of the 40nm SP578 sample series. (b) RBS spectrum of the 200nm SP601 sample series.

Table 5.4 Determined stoichiometries from RBS data fits of the SP578 series.

Sample ID	Sample state	La : Sr : Mn
SP578	As-prepared	0.71 : 0.29 : 0.95
SP578-1	E-PV	0.73 : 0.27 : 0.75
SP578-2	BM	0.69 : 0.31 : 0.55

Table 5.5 Determined stoichiometries from RBS data fits of the SP601 series.

Sample ID	Sample state	La : Sr : Mn
SP601	As-prepared	0.75 : 0.25 : 0.83
SP601-3	Inter-, E-PV	?
SP601-4	BM	0.75 : 0.25 : 0.80

5.2.9 Neutron diffraction

The thin film sample SP603 with a size of 10mm×10mm was Al-assisted vacuum annealed at 450°C for 15h. A 200nm thick BM-LSMO phase and with only a very small residual portion of the intermediate phase remaining was obtained. To probe the SP603 BM-LSMO magnetic structure, neutron diffraction was employed. However, neutron diffraction, using a wavelength of 2.31Å, was measured only at 295K due to time constraints of the beam time which was conducted by Suqin He. Magnetometry results obtained on BM-LSMO SP601-4 indicated that a possible antiferromagnetic state exists with a Néel-temperature at ca. 400K. Therefore potential antiferromagnetic structures were probed, i.e. A-type, C-type and G-type antiferromagnetism, as shown in **Figure 5.13**. Correspondingly, the vicinity around the (0 0

0.5), (0.5 0.5 0) and (0.5 0.5 0.5) Bragg peaks were scanned. The measurement is only a partial success. The nuclear peak of the film can be observed e.g. the (002) BM-LSMO nuclear peak (**Figure 5.13 (a)**) in contrast to previous efforts by Dr. Lei Cao at the same instrument at Grenoble and at DNS at Garching, where even the nuclear Bragg peak was unobservable.
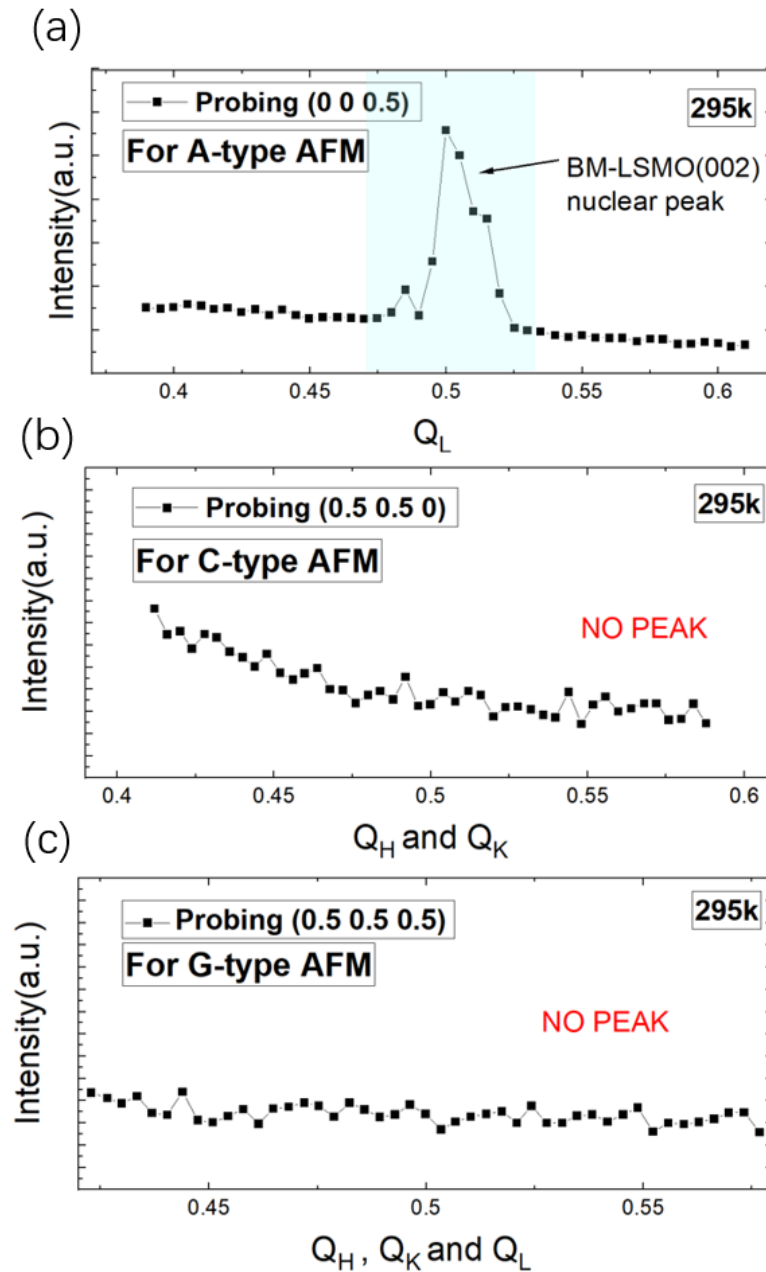

Figure 5.13 Neutron diffraction pattern of the annealed 200nm film SP603. (a) Scan around the vicinity of the (0 0 0.5) Bragg peak in order to probe an A-type antiferromagnetic (AFM) structure. (b) Vicinity around the (0.5 0.5 0) Bragg peak in order to probe a C-type AFM structure. (c) Vicinity around the (0.5 0.5 0.5) Bragg peak in order to probe for a G-type AFM structure.

5.3 Al-assisted vacuum annealing on LSMO powder

Chapter 5.2 described the Al-assisted vacuum annealing on the strained thin film system. In this section, the strain free bulk-like LSMO powder samples and Al-assisted vacuum annealing are discussed for comparison. In our previous study, bulk powder samples were prepared by hand-milling which exhibits particle sizes in the order of 5μm with a very broad size distribution. For the study described here, powder samples are reproduced however using ball-milling in order to obtain a narrower particle size distribution.

5.3.1 Powder sample preparation

A S100 planetary ball mill from Retsch company is used for the LSMO bulk powder preparation. Bulk LSMO is obtained from an old LSMO sputtering target being the same target used for the preceding hand-milling preparation. First, the bulk LSMO target is broken and hand-milled in a SiO_2 crucible to reduce the particle size to the millimeter range. Then 10 grams of pre-milled powder is further milled in the planetary ball mill at a speed of 250 rounds per minute for 120 minutes.

The morphology of the final as-prepared powder samples is characterized using SEM. As shown in **Figure 5.14**, one can obtain powder samples with an overall relatively homogeneous particle size distribution (**Figure 5.14(a)**). The average size is approximately 3μm (**Figure 5.14(b)**). Moreover, such small particles can aggregate (**Figure 5.14(c)**) due to e.g. electrostatic or van der Waals interactions. Additionally, small amounts of individual large particles (**Figure 5.14(d)**) with sizes of ca. 50μm still remain after ball milling. Elemental analysis by ICP-OES yields the mass content of selected elements as illustrated in **Table 5.6.** Fe, Si and Al show a low content, while the molar ratio of La : Sr : Mn is 71.30 : 31.35 : 100 which reveals a similar stoichiometry compared with the sputtering target which is 70 : 30 :100.

Table 5.6 Elemental analysis of the as-prepared powder sample.

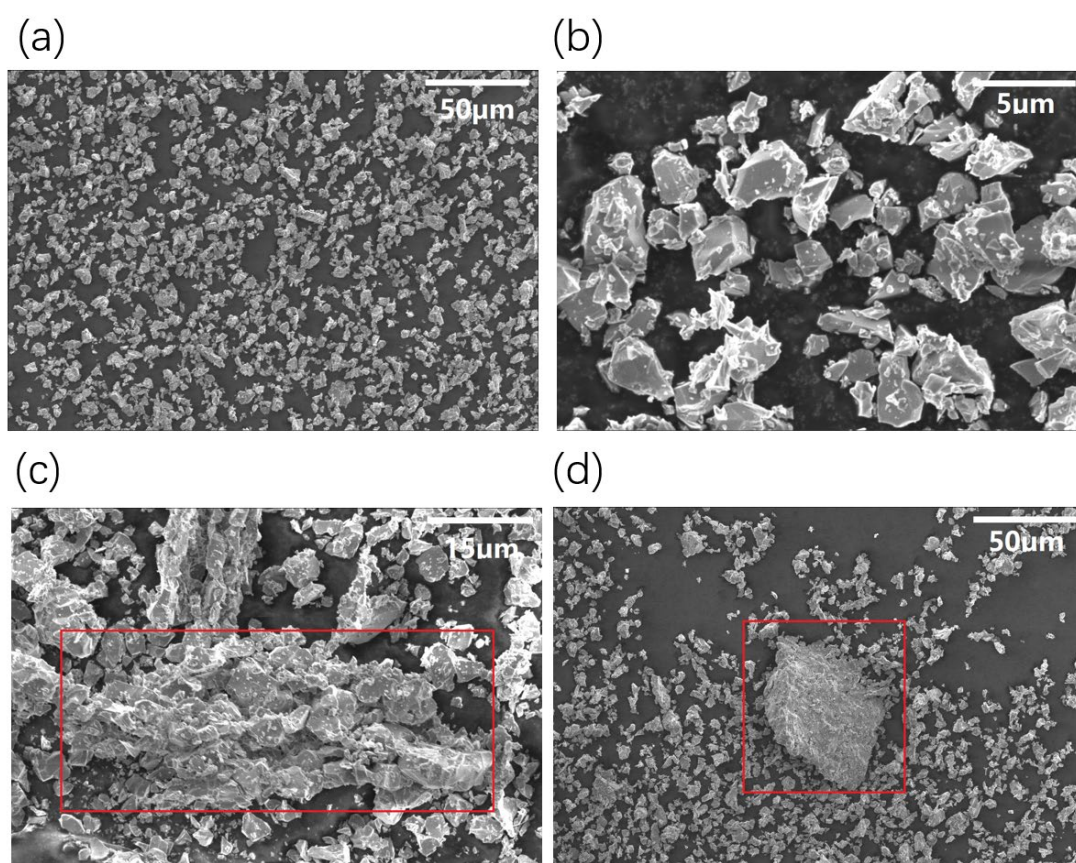| Sample ID	La [%]	Sr [%]	Mn [%]	Fe [%]	Si [%]	Al [%]	La : Sr : Mn molar ratio
As-prepared	42.9 ±0.7	11.9 ±0.08	23.8 ±0.4	0.0125 ±0.0005	0.0123 ±0.0012	0.0039 ±0.0003	**71.30 : 31.35 : 100**

Figure 5.14 SEM images of the as-prepared powder samples. Panels (a), (b) show an overview and a zoom-in part of the powder samples, respectively. Panels (d), (c) show aggregates and the residual large-sized particles (red box), respectively.
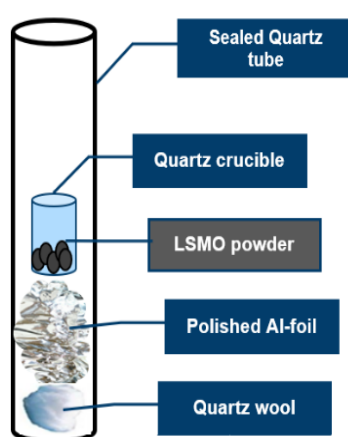
5.3.2 Structural changes

Figure 5.15 Experimental configuration of Al-assisted vacuum annealing on LSMO powder.

As shown in **Figure 5.15**, ca. 0.05g of the as-prepared LSMO powder sample is loaded in a quartz crucible and then sealed together with ca. 0.5g polished Al-foil in the quartz tube. The

tube size is the same as the one employed for the 40nm SP578 thin film sample series. The assembly was then evacuated at ZEA-1 to reach 5×10^{-6} mbar and subsequently annealed in a furnace. The annealing time for all series is fixed to be 20 hours. Various annealing temperatures 350℃, 450℃ and 550℃ are selected for this investigation. The corresponding XRD patterns are shown in **Figure 5.16**. For the as-prepared powder sample, the XRD shows a typical PV structure which implies a good crystal quality after ball milling. When annealed at 350℃, the sample demonstrates no significant structural transformation indicated by the green dotted lines. At 450℃, the structure is observed to be partially in the previously found intermediate phase. For 550℃ one finds the highest transformation speed. Here a BM phase is achieved. The PV to BM topotactic transition obviously can also be triggered by Al-assisted vacuum annealing of ball-milled powder.

In my previous work, powder samples annealed without Al at 550℃ for 75h shows no structural variation, which confirms the importance of Al as oxygen getter during annealing. It will be important for a future study to estimate the thickness of Al oxide layer on Al-foil after triggering the LSMO PV to BM phase transition and any by this to check if the used amount of Al is sufficient. 1.77mg oxygen will be released when 0.05g powder LSMO is transformed from PV to BM. Thus only 1.99mg Al (0.4% of 5g Al) is oxidized according to the reaction: $4Al + 3O_2 \rightarrow 2Al_2O_3$. Correspondingly, a ca. 73nm thick Al_2O_3 layer will be formed on the Al-foil surface. This thickness is smaller than the maximum possible thickness as reported i.e. 200nm [54].
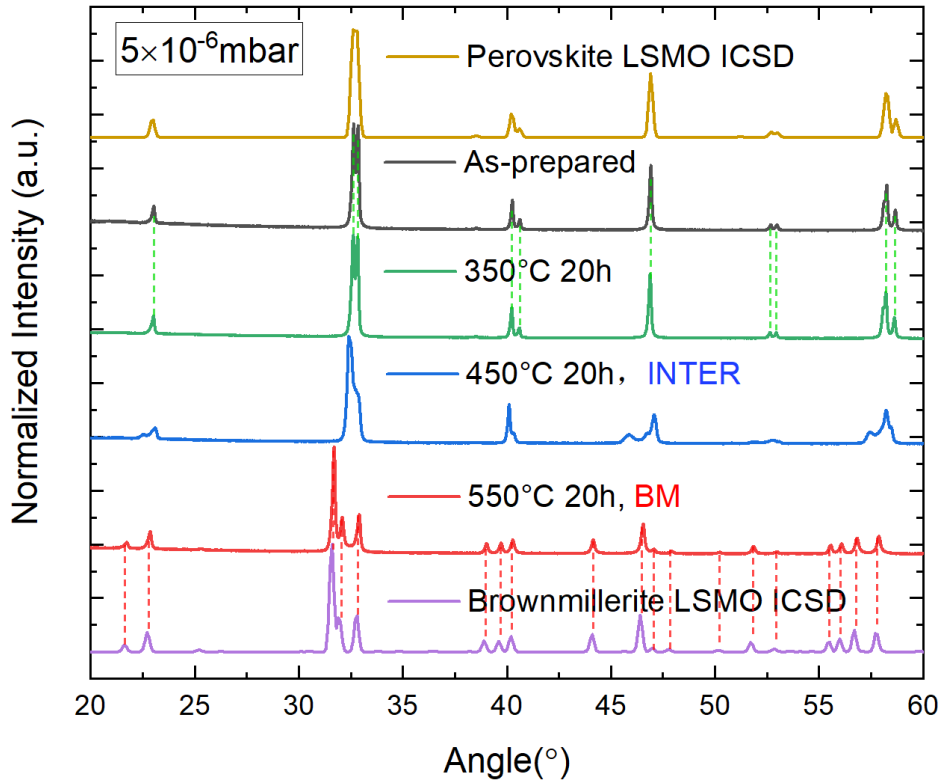
Figure 5.16 XRD pattern of the as-prepared powder sample and of various samples annealed at different temperatures for 20h: 350°C, 450°C and 550°C. ICDS data base patterns for the PV and BM phase are also shown for comparison.

5.3.3 Magnetometry measurements

To characterize the magnetic properties before and after annealing, FC and ZFC curves are measured using SQUID magnetometry, as shown in **Figure 5.17**. In the FC curve (**Figure 5.17(a)**), the as-prepared powder sample exhibits a T_C of ca. 369K, while the 350°C annealed sample shows a reduced T_C of ca. 355K. This reduction might be due to the weaker double-exchange interactions induced by oxygen vacancies. However, in the XRD patterns one cannot observe an obvious structural change. This finding demonstrates the large sensitivity of magnetic properties to even small changes in the electronic structure of such systems. At the temperature of 325K, the magnetization contribution of antiferromagnetism is negligible, and thus can be employed to estimate the remaining ferromagnetic contribution by comparing the value of magnetization. For the 350°C 20h annealed powder sample, 56.41% ferromagnetic contribution remains. For the 550°C 20h annealed powder sample (BM) only 0.23% remains. In the ZFC curve (**Figure 5.17(b)**), the BM phase shows a typical antiferromagnetic behavior with a Néel-temperature around 55K. However, this result is different from the BM-LSMO film

but close to the result presented in **Chapter 6**, which is a E-PV state film obtained via ILG. This implies that the 550℃ 20h annealed powder sample is not a pure BM phase. The real signal of BM-LSMO powder might be masked by a remaining E-PV phase.
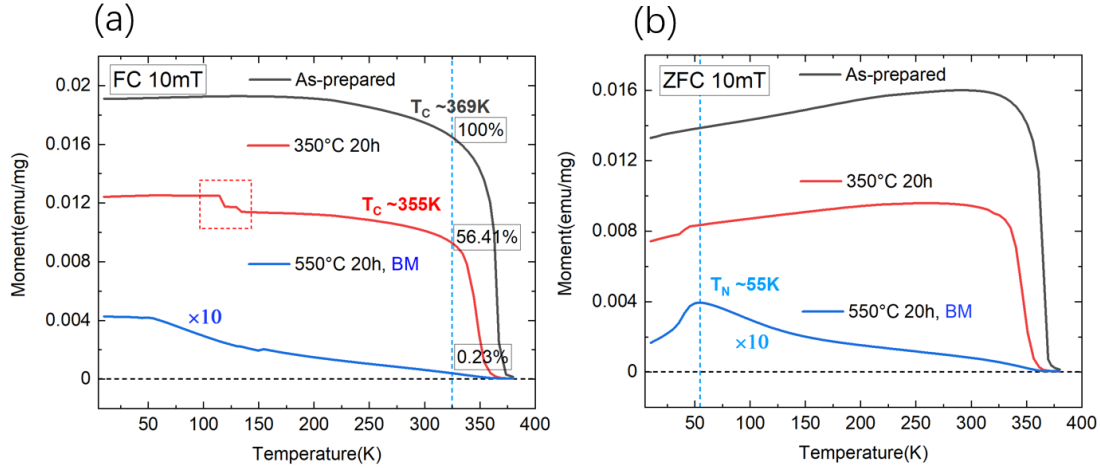

Figure 5.17 Magnetization-temperature curves of the as-prepared powder sample and the annealed samples, normalized by sample mass. Panel (a) shows the FC curves. Panel (b) shows the ZFC curves. The amplitude of the blue curves is multiplied by a factor of 10 for better comparison. Several kinks appear in the curves as marked by the red boxes. These are very likely artifacts caused by the measuring device.

Similar to thin film samples, the mean field theory approximation is applied to model the magnetic properties of the as-prepared ferromagnetic powder samples. The value for M_S is estimated to be $1.91 \times 10^4 \mathrm{Am^2Kg^{-1}}$ by extending the FC curve to 0K. The fitting steps are the same as shown in **Chapter 4.2.1.3**. Results are shown in **Figure 5.18**. In total a ferromagnetic type order parameter behavior is reproduced. However, all physically realistic J values lead to a large deviation between model and measured FC curve. This only gives a hint that the mean field theory approximation can hardly fit a complex oxide system to the pronounced electronic correlations and the interplay of various degrees of freedom in the system.
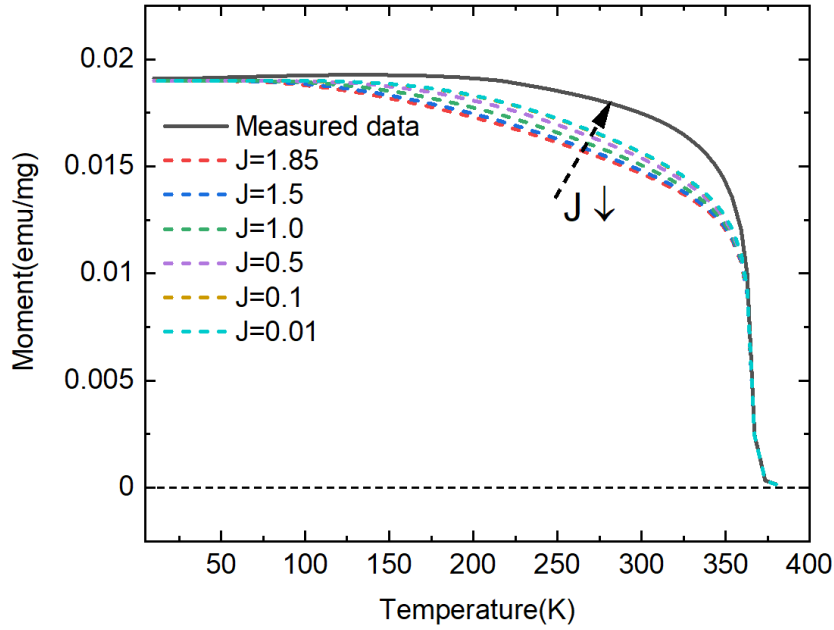
Figure 5.18 Mean field theory approximation fitting of the as-prepared powder sample for various *J* values.

5.4 Summary

In this chapter, we demonstrate that the PV-BM topotactic phase transition can be successfully triggered in 40nm and 200nm LSMO films via Al-assisted vacuum annealing at more optimal conditions, i.e. at only 400°C for 12h and 450°C for 12h, respectively. The structural changes during the phase transition are characterized by XRD. A clear transformation process between the E-PV phase and the intermediate phase is evidenced by the change of Bragg peak intensity as well as the emerging of superlattice peaks in XRD patterns. This indicates the previously reported oxygen rearranging process. The final BM phase is confirmed by the observation of only even superlattice peaks. Moreover, a decomposition of film is found during annealing and verified by the strongly reduced SLD in XRR and by the topographic changes observed in AFM measurements.

The coexistence of Mn^{3+} and Mn^{4+} in the as-prepared films is evidenced by XAS thus leading to double-exchange interactions and ferromagnetic behavior. After annealing, the oxidation state of Mn is found to be reduced. This can result in superexchange interactions and thus antiferromagnetism, which is observed in the 200nm mixed state film and in the 40nm E-PV film by SQUID magnetometry. The different Néel-temperatures i.e. 30K and 45K might be

attributed to superexchange interaction among Mn^{2+} and among Mn^{3+}, respectively. However, the obtained BM-LSMO films exhibit a new type of magnetic structure, as a peak appears at ca. 400K in magnetization vs. temperature curves. To probe the spin structure of BM-LSMO, neutron diffraction measurements were performed, while only the nuclear film Bragg peaks could be detected.

We also successfully triggered the PV-BM phase transition via Al-assisted vacuum annealing in ball-milled bulk-like LSMO powder samples. BM-LSMO powder with antiferromagnetic behavior was obtained after annealing at 550°C for 20h. However, the antiferromagnetic signal might be overlaid by a remaining E-PV phase.

6. Control of physical properties via ionic liquid gating on LSMO and Fe₃O₄ thin films

This chapter describes the studies using ionic liquid gating (ILG) on LSMO and Fe_3O_4 thin films grown on a conductive substrate Nb-STO and the impact of ILG onto the physical properties.

6.1 Motivation

For LSMO thin films, various ways can be employed to modify the physical properties, e.g. thermal vacuum annealing [10,11,12], voltage control [13], ion irradiation [58] and ILG [15,59]. Compared with thermal vacuum annealing, ILG can exhibit a larger transformation efficiency. Moreover, a "triple-state phase transformation" was reported via ILG on the $SrCoO_3$ system. A BM phase and a hydrogenated BM phase (HBM) were obtained from the original PV phase [16]. However, a similar PV-BM-HBM transition has never been reported for the LSMO system. Hence, ILG was applied on our LSMO films to trigger a potential multiple-ionic switching. As a side study, an attempt of ILG on Fe_3O_4 thin films was performed.

Previously, LSMO films grown on insulating STO substrates were used for ILG. Electrodes were directly connected on top of the film surface corners. Consequently, untransformed areas under the coverage of electrodes are introduced in this approach (**Figure 6.1**). The presence of

untransformed areas will also increase difficulties in XRR analysis and magnetization measurements. Moreover, an inhomogeneous lattice expansion in the out-of-plane direction was observed via XRD on films gated at 5V and 6V, which could be attributed to the fact that the LSMO near the corner electrodes can be transformed at a higher speed compared to areas far apart from the corners. This inhomogeneous transformation results in structural subsystems in the film. Additionally, the gated films exhibit a reduction of magnetization and of T_C as found from SQUID magnetometry indicating weaker double exchange interactions. When extending the gating time, no further structural changes occur. This saturation behavior can be explained by a self-passivation effect of the film during gating. One can assume that the film near the corner electrodes can be transformed at a very high speed and form insulating parts. Thus, the film far apart from the corners will lose the voltage supply. This can lead to a termination of transformation, as illustrated in **Figure 6.1(b)**.

In this chapter, conductive Nb-STO substrates are employed. Then, the Pt wires can be connected either at the edge or on the backside of the substrate rather than on the film. This might improve the homogeneity of the film during the transformation and avoid the self-passivation effect. Furthermore, the mode of "intermittent-in-situ" gating is described here.
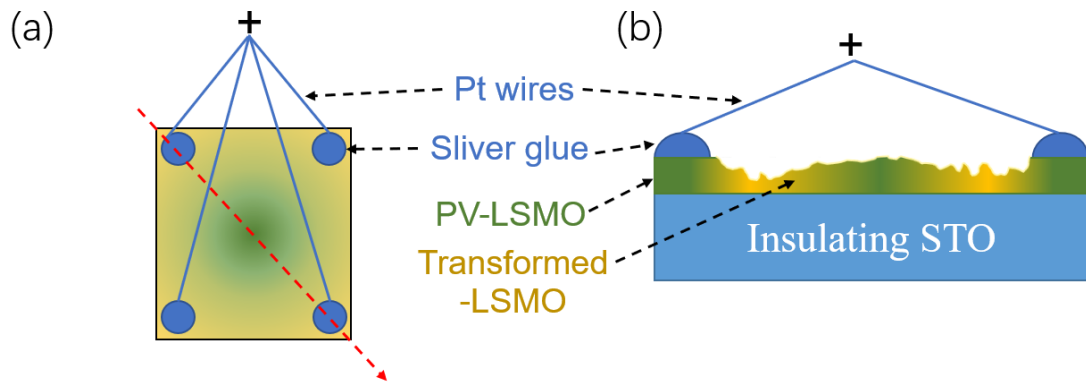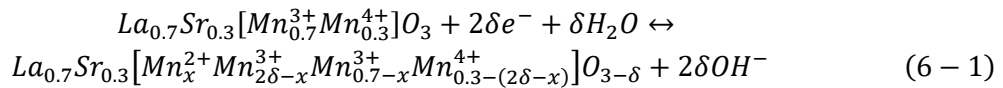

Figure 6.1 Schematic of the electrode connections using surface-corner positions. (a) Top view, electrodes are connected via silver glue at surface corners. (b) Side view along the red line direction in panel (a): the LSMO film beneath the electrodes are untransformed (green), the LSMO near the corners undergoes a higher transformation speed and a larger decomposition thus being transformed to an insulating state and lead to self-passivate. Different colors of the film illustrate the subsystems.

6.2 Ionic liquid gating method and experimental configuration

By applying a voltage using an ionic liquid $[DEME]^+[TFSI]^-$ various physicochemical phenomena can be triggered. Frist, the electric field will drive anions and cations inside the ionic liquid and then accumulate them at the corresponding electrodes. The accumulated charge will also induce an accumulation of opposite charges at the solid side by electrostatic induction thus forming an electric double layer (EDL, illustrated in **Figure 6.2**) with a thickness of several nanometers. This generates an electric field near the solid surface. Moreover, the charge accumulation at the inner surface of the solid can introduce charge depletion in the rest of the film thus enabling electrostatic doping [60]. Such electrostatic doping can trigger a change of orbital occupancies and by this tune the magnetic properties [61].

Second, using a higher gating voltage, the insertion or removal of ions induced by the electrical field as well as electrochemical reactions can dominate. The as-prepared ionic liquid contains a certain amount of water. When exposing the ionic liquid to air, traces of water moisture will also be introduced. The potential electrochemical reaction promoted by water can bring oxygen vacancies inside the LSMO film, as described in **Equation 6-1** [14,62]. Here δ and x denote the electrochemical reaction induced oxygen off-stoichiometry and the resulting Mn^{2+}, respectively. Moreover, hydrogen ions originating from water splitting can be inserted into the film via the electrical field in the ionic liquid and the EDL, i.e. hydrogen ions are small enough to enter the LSMO lattice. Such a so-called "dual ionic transfer", i.e. for hydrogen and oxygen, has been demonstrated through ILG recently [16].
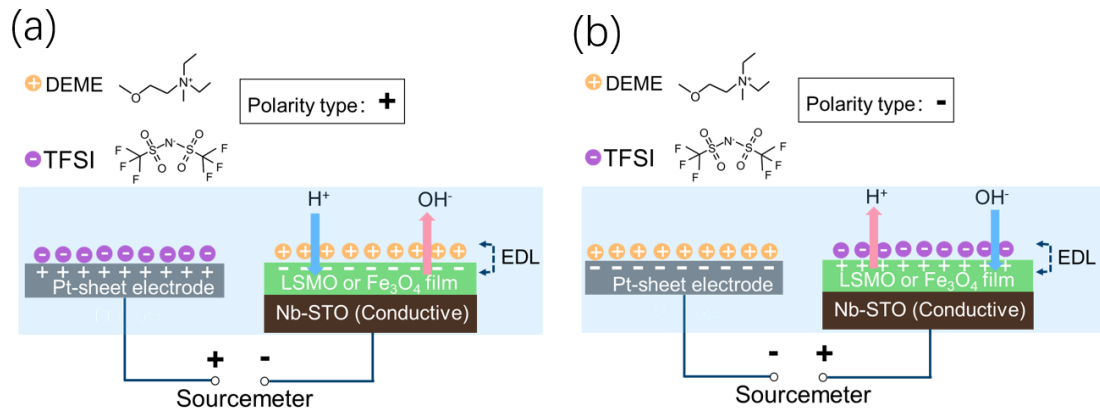
$$La_{0.7}Sr_{0.3}[Mn_{0.7}^{3+}Mn_{0.3}^{4+}]O_3 + 2\delta e^- + \delta H_2O \leftrightarrow$$
$$La_{0.7}Sr_{0.3}[Mn_x^{2+}Mn_{2\delta-x}^{3+}Mn_{0.7-x}^{3+}Mn_{0.3-(2\delta-x)}^{4+}]O_{3-\delta} + 2\delta OH^- \qquad (6-1)$$

Figure 6.2 ILG mechanism at different electrical polarities. The polarities ± are defined in panel (a) and (b), respectively.

The typical experimental configuration defined as type 1 is shown in **Figure 6.3 (a)**. The gating voltage is supplied by a Keithley 2400 Sourcemeter, allowing the desired voltage value with a current upper limit during the gating experiment. A quartz reaction cell with two pools was prepared by ZEA-1. The film with a size of $5mm \times 5mm$ is mounted using double-sided tape at the bottom of the second pool, and two Pt wires with a diameter of $50\mu m$ are connected by Acheson Silver DAG 1415M glue at the edges of the conductive Nb-STO substrate thus enabling the entire film as electrode (cathode or anode depending on polarity).

Similarly, a Pt sheet fixed at the base of the first pool has the same area as the film and is also connected by a Pt wire at the center of the surface and thus acts as another electrode. Such a two-pool cell can hereby ensure that the film and the Pt electrodes are at the same height and thus reduce an electrical field inhomogeneity caused by a vertical misalignment. The cathode and anode are separated horizontally by ca. 2mm and are both surrounded by sufficient ionic liquid. The corresponding Pt wires are connected to Pt sheets which are connected to the Sourcemeter by copper wires.

To further improve the homogeneity of the electric field in the lateral direction, the type 2 configuration is used (**Figure 6.3 (b)**). Two Pt electrodes are placed on both sides of film and the Pt wire is glued by silver glue at the bottom of the film substrate. This configuration can enable a stronger but more homogenous electric field at the film surface at the same voltage.
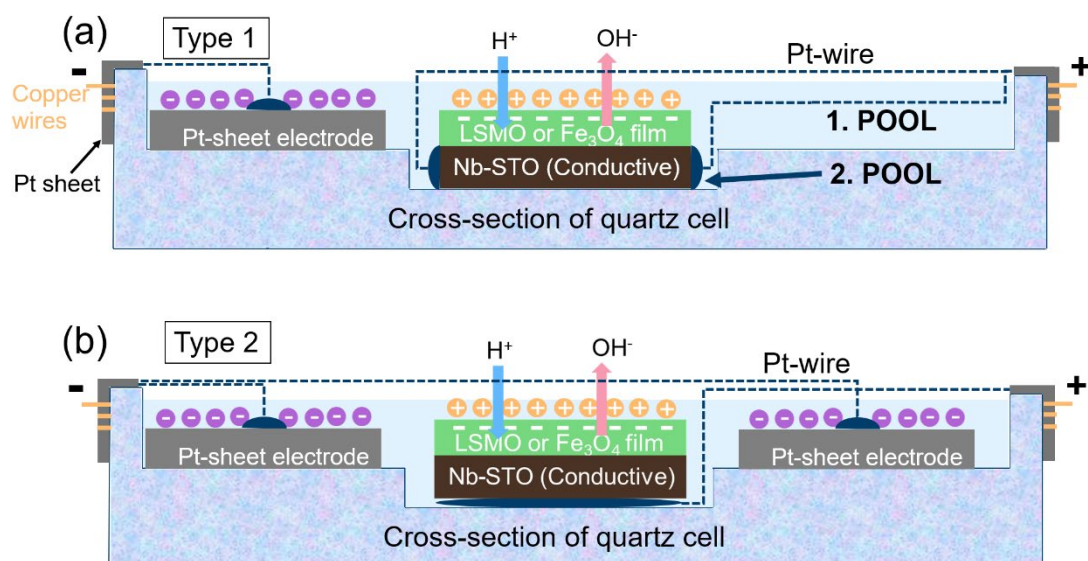
Figure 6.3 ILG experimental configuration at polarity +. (a) type 1 configuration. (b) type 2 configuration.

6.3 Changes of physical properties after ionic liquid gating on LSMO thin films

6.3.1 Sample growth and gating parameters

For LSMO, two gating voltages i.e. 2.8V and 3.2V were investigated on 40nm films via the type 1 configuration with polarity +. Additionally, a reduced voltage 2.6V was applied on a 100nm film via the type 2 configuration with the same polarity. The growth and gating parameters are provided in **Table 6.1** and **Table 6.2**. In the following text, SP589-4 and SP594-2 are labeled as "40nm film" and SP609 labeled as "100nm film".

Table 6.1 LSMO film growth parameters and the as-prepared thicknesses.

Sample ID	Sputter Target status	Growth temperature [°C]	Oxygen pressure [mbar]	Plasma power [W]	Growth time [min]	Thickness [nm]
SP589-4	Stage I	800	2	120	60	39.54$\pm$0.4
SP594-2	Stage I	800	2	120	60	33.73$\pm$0.3
SP609	Stage III	800	2	90	180	ca. 100

Table 6.2 LSMO ILG parameters.

Sample ID	Electrical polarity [±]	Gating configuration	Gating type	Gating voltage[volt]	Total gating time[min]
SP589-4	+	Type 1	Intermittent	3.2	50
SP594-2	+	Type 1	Intermittent	2.8	60
SP609	+	Type 2	In-situ	2.6	56

Due to the strong absorption of X-rays by ionic liquids, the 2.8V and 3.2V gating experiments are performed in an "intermittent-in-situ mode". The ionic liquid is first added for gating and then removed for a short time to expose the film surface for an XRD measurement. Subsequently the liquid is added back to the cell and the gating is continued. This process is repeated until the end of the gating experiment. The thickness of the liquid above the film is estimated to be 2mm during ILG.

6.3.2 Structural changes

Figure 6.4 shows the XRD pattern during gating at 2.8V and 3.2V. For 2.8V gating (**Figure 6.4 (a)**). After 10min the (002) film Bragg peak shifts towards the STO (002) peak indicating a lattice expansion and exhibits a lower intensity when compared with the as-prepared state. Then the thin film peak starts to overlap with the substate STO (002) peak after 15min. However, with further gating, the film peak seems to disappear. One might attribute this finding to a structural decomposition of the film or a continued overlapping with the substrate peak.

For 3.2V (**Figure 6.4 (b)**), the transformation speed is enhanced due to the increased gating voltage. Already after 10min the film peak appears on the left-hand side of STO (002) peak but with a lower intensity and with the estimated out-of-plane lattice parameter of 3.932 ± 0.005Å. With assuming that the film is still fully strained on the substrate, the lattice expansion can be directly determined using the out-of-plane parameter to be 2.1%. For longer gating times, the film peak turns to become an extended plateau-like feature. This might be due to a coexistence of many sub-systems with a wide distribution of lattice parameters. The corresponding maximum expansion is estimated to be 3.971 ± 0.005Å (3.1% expansion) for 20min and

4.003±0.005Å (3.92% expansion) for 30min. For 50 min, a more extended plateau-like feature is observed.
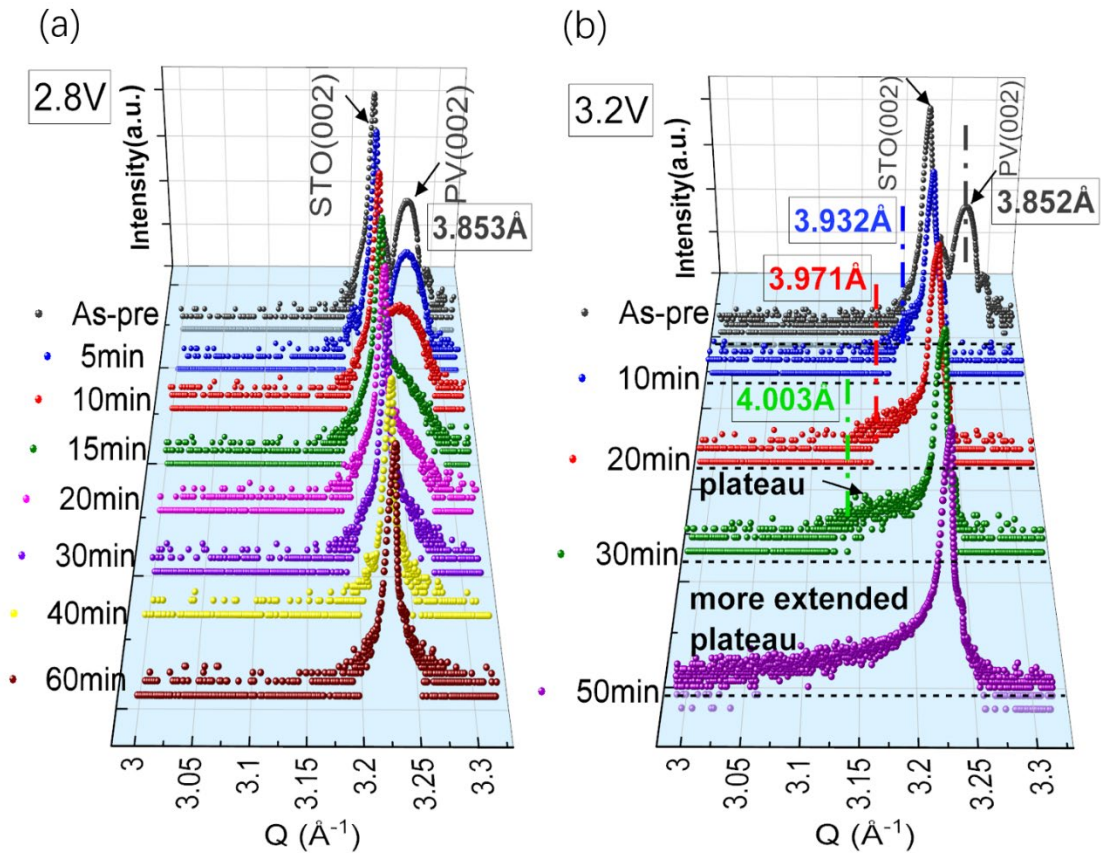

Figure 6.4 XRD pattern during gating. (a) 2.8V 60min gating of SP594-2 using the configuration type 1 using polarity ＋. (b) 3.2V 50min gating of SP589-4 using the configuration type 1 using polarity ＋.

The investigation of the stability of the gated films is shown in **Figure 6.5**. After 5 days in air, the XRD pattern of the 2.8V gated film reveals a right-shifted film peak. This confirms that the previously disappeared film peak is not due to a structural destruction of the lattice but due to the overlapping of the film peak with the STO (002) peak. This right-shifting can be attributed to the oxygen-retake resulting in a decrease of lattice expansion. For the 3.2V gated film, the XRD pattern stays almost unchanged after 23 days. This might imply that interestingly the film is stabilized at higher gating voltages or it is decomposed to an amorphous structure.
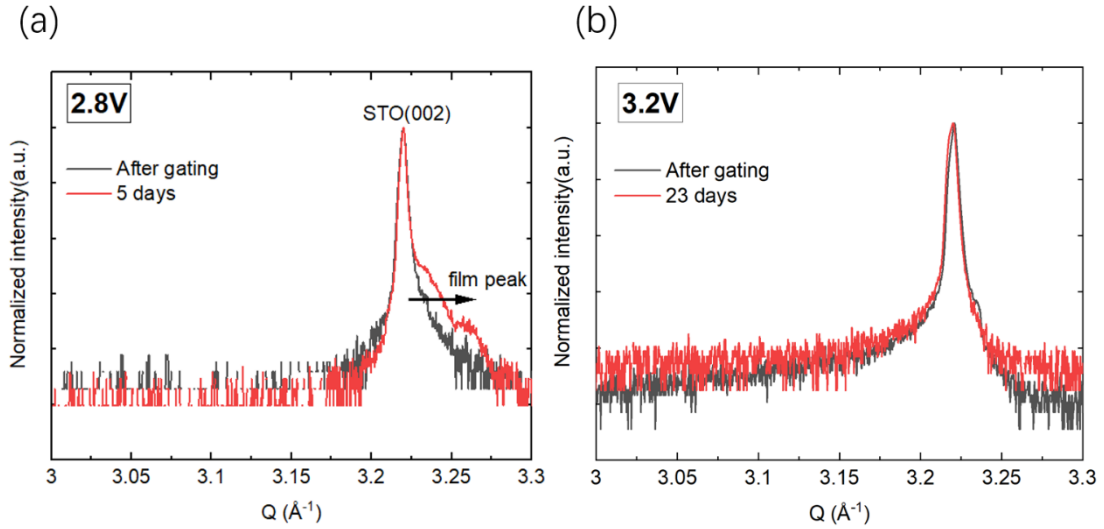
Figure 6.5 Stability investigation after gating. (a) 2.8V 60min gated SP594-2, after gating and in air for 5 days. (b) 3.2 V 50min gated SP589-4, after gating and in air for 23 days.

The thickness, roughness and SLD are characterized via XRR. The results are shown in **Figure 6.6** and **Table 6.3**. For the as-prepared SP589 and the 2.8V gated SP594-2, a three-layer model as mentioned in **Chapter 4** is used. For 3.2V gated SP589-4, a four-layer model as mentioned in **Chapter 5** is employed for a better fitting result. It follows that the thickness of the as-prepared SP589 is 39.54 ± 0.4nm with a roughness of 3.02 ± 0.03nm. After 2.8V gating, the roughness of SP594-2 is reduced from 2.83 ± 0.03nm to 0.62 ± 0.01nm, meanwhile the SLD is decreased from $(4.79\pm0.05)\times10^{-5}\text{Å}^{-2}$ to $(4.58\pm0.05)\times10^{-5}\text{Å}^{-2}$ (see **Chapter 4**). For the 3.2V gated SP589-4, the results indicate a depth dependent SLD reduction. Near the surface the SLD is reduced by 33.5% to $(3.18\pm0.03)\times10^{-5}\text{Å}^{-2}$. For the second LSMO layer it is reduced by 21.8% to $(3.74\pm0.04)\times10^{-5}\text{Å}^{-2}$. Both 33.5% and 21.8% are larger than the theoretical SLD reduction of the oxygen vacancy induced PV to BM phase transition being 10.2%. This suggests that either a decomposition started at the surface and continues deeper into the film or it indicates a hydrogen-insertion induced lattice expansion.
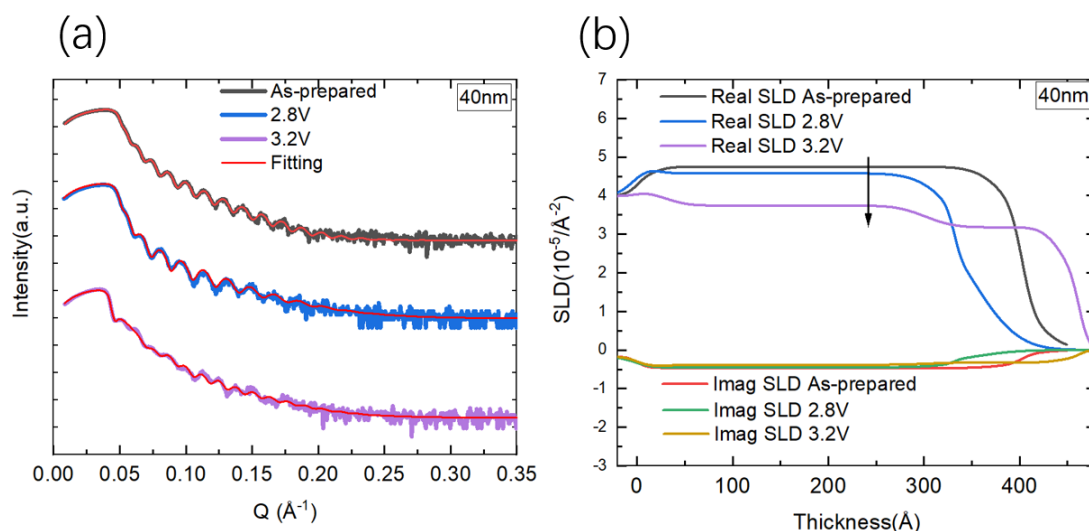
Figure 6.6 (a) Fitted XRR pattern of the as-prepared SP589, the 2.8V 60min gated SP594-2 and the 3.2V 50min gated SP589-4. (b) Corresponding calculated SLD. Fitted by the software GenX.

Table 6.3 Data fitted from the XRR measurements.

Sample ID	Gating voltage	Surface roughness	LSMO 1st layer thickness	LSMO 1st layer SLD	LSMO 2sec layer thickness	LSMO 2sec layer SLD
	[volt]	[nm]	[nm]	$[10^{-5}Å^{-2}]$	[nm]	$[10^{-5}Å^{-2}]$
SP589 as-prepared		3.02 ± 0.03	39.54 ± 0.4	4.78 ± 0.05		
SP594-2	2.8	0.62 ± 0.01	31.64 ± 0.3	4.58 ± 0.05		
SP589-4	3.2	1.70 ± 0.02	14.50 ± 0.1	3.18 ± 0.03	27.32 ± 0.3	3.74 ± 0.04

As mentioned above, when using the type 1 configuration, the film during ILG exhibits either a relative slow transformation speed or a poor homogeneity. For improving the transformation, the type 2 configuration is used. Considering the decomposition effect, ILG was attempted for the first time on a "thick" film with a thickness of ca. 100nm. For this film, a "real-time in-situ gating" mode is employed and the thickness of the ionic liquid above the film is reduced to ca. 1mm for better X-ray penetration. The 100 nm film SP609 was gated at 2.6V. As **Figure 6.7** illustrated, the in-situ XRD only shows a very low signal, while the (002) film peak cannot be resolved.
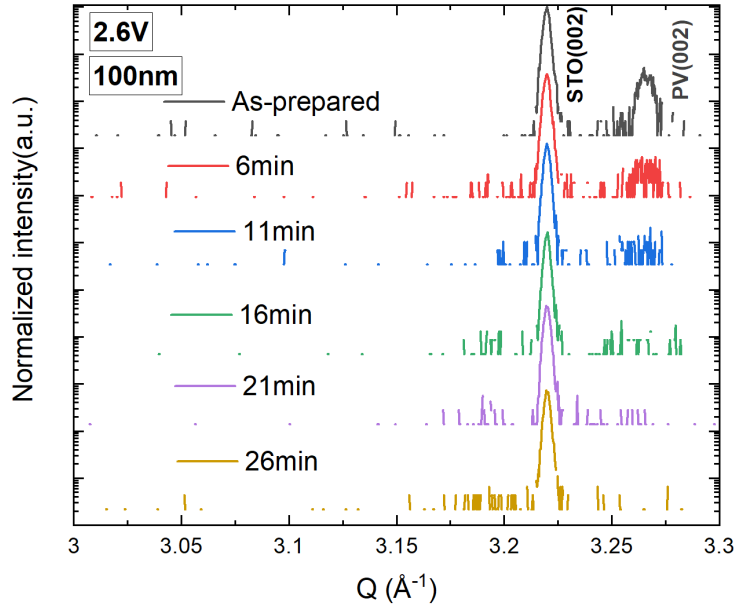
Figure 6.7 Complete in-situ monitoring XRD with uninterrupted coverage with the ILG liquid during the experiment of the100nm film SP609, gated at 2.6V using the type 2 configuration.

Consequently, the gating mode was switched back to the "intermittent-in-situ" mode for a better resolution. The results are shown in **Figure 6.8 (a)**. After 26min gating the film peak emerged at the left-hand side of the STO (002) peak with an out-of-plane parameter of 3.942±0.001Å (2.4% expansion). The "extended PV phase" with a lattice expansion is defined as "E-PV", as mentioned in **Chapter 5**.

After 56min the film peak was observed at nearly the same position at 3.947±0.005Å while with a strong intensity reduction, which indicates a film decomposition effect. However, the plateau-like feature was not observed implying an improved homogeneity during gating. The structural stability of the 100nm film gated at 2.6V is checked before the SQUID measurement, illustrated in **Figure 6.8 (b)**.
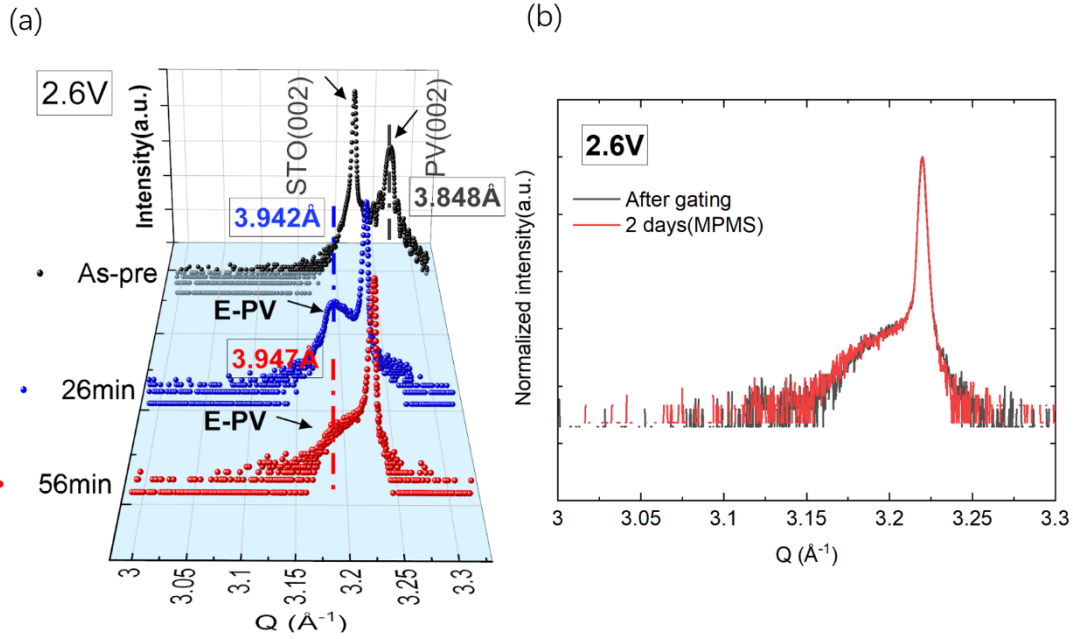
Figure 6.8 (a) "Intermittent-in-situ" mode XRD pattern of the 100nm film SP609 during the gating at 2.6V. (b) The structure of the gated SP609 is confirmed to be unchanged using XRD before the SQUID measurement.

The XRR data of the gated SP609 film is shown in **Figure 6.9** and **Table 6.4**. As mentioned in **Chapter 4**, the Kissig oscillation of a "thick" film cannot be observed, which is likely due to signal damping of the increased film thickness and the small oscillation period to be resolved. This also applies to the as-prepared SP609 film. The thickness of SP609 is estimated by the deposition time yields ca. 100nm. However, after gating SP609 shows a clear Kissig oscillation, the four-layer model used for the 3.2V gated 40nm SP589-4 film is employed for fitting. The total thickness of the gated SP609 is found to be 22.88$\pm$0.2nm which implies that ca. 70% of film is decomposed during gating. This reflects the high transformation speed when using the type 2 configuration even at a low voltage of 2.6V.
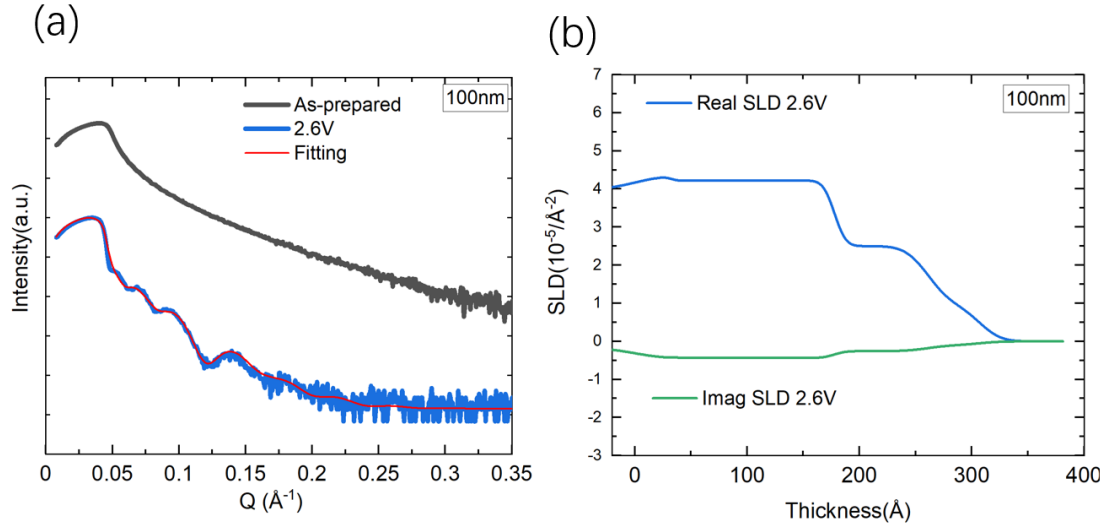
Figure 6.9 (a) Fitted XRR pattern of the as-prepared state of SP609 and the 2.6V 56min gated SP609. (b) Corresponding calculated SLD. Fitted by software GenX.

Table 6.4 Data fitted from the XRR measurements.

Sample ID	Gating voltage [volt]	Surface roughness [Å]	LSMO 1st layer thickness [Å]	LSMO 1st layer SLD [10^{-5}Å^{-2}]	LSMO 2sec layer thickness [Å]	LSMO 2sec layer SLD [10^{-5}Å^{-2}]
SP609 As-prepared			ca. 100nm			
SP609 gated	2.6	1.63±0.02	8.37±0.08	2.50±0.03	14.51±0.1	4.22±0.04

To summarize, for the 40nm film, the 2.8V case demonstrates a lower transformation speed. The film peak overlaps with the STO (002) peak after 60min gating. Moreover, the film peak reappears again due to oxidation in air. The 3.2V case shows a larger speed of transformation. Here the film peak appears on the left-hand side of the STO (002) peak. However, the larger transformation speed might introduce a decreased homogeneity leading to a distribution of sub-systems and hence the appearance of a broad peak (or plateau). The 33.5% and 21.8% reduced SLD in XRR implies a decomposition of film. The type 2 configuration exhibits a large transformation speed on the 100nm film at 2.6V and shows a good film homogeneity during gating. The film thickness is reduced by ca. 70% after gating. These results constitute a major further step in employing ILG for the transformation from the PV to the BM phase. However, to achieve a complete and homogeneous transformation further work is necessary, in particular to optimize the in-situ ILG cell setup.

6.3.3 Changes of magnetic behavior

The magnetic properties of 2.6V gated 100nm SP609 film are characterized by SQUID-magnetometry. The ZFC curves are shown in **Figure 6.10(a)**. The gated film exhibits a typical antiferromagnetic behavior with a Néel-temperature at ca. 55K. This value for the Néel-temperature is close to the value which we obtained for the BM-LSMO powder system (i.e. 55K) as discussed in **Chapter 5.3.3**. The large broadness of the peak might be attributed to the coexistence of subsystems as mentioned in **Chapter 6.3.2**. When gated with polarity +, the introduced $V_O^{\cdot\cdot}$ and H_i can change the oxidation state of Mn and hence the superexchange interactions between Mn^{3+} and Mn^{3+} or among Mn^{2+} and Mn^{2+} can lead to the antiferromagnetism. To estimate the remaining ferromagnetic contribution, the FC curve of the as-prepared and the gated film are normalized to the value at 200K where the antiferromagnetic contribution is negligible. As show in **Figure 6.10 (b)** the remaining ferromagnetic contribution of the gated film is ca. 0.77% which implies that the double-exchange interaction in film is largely suppressed.
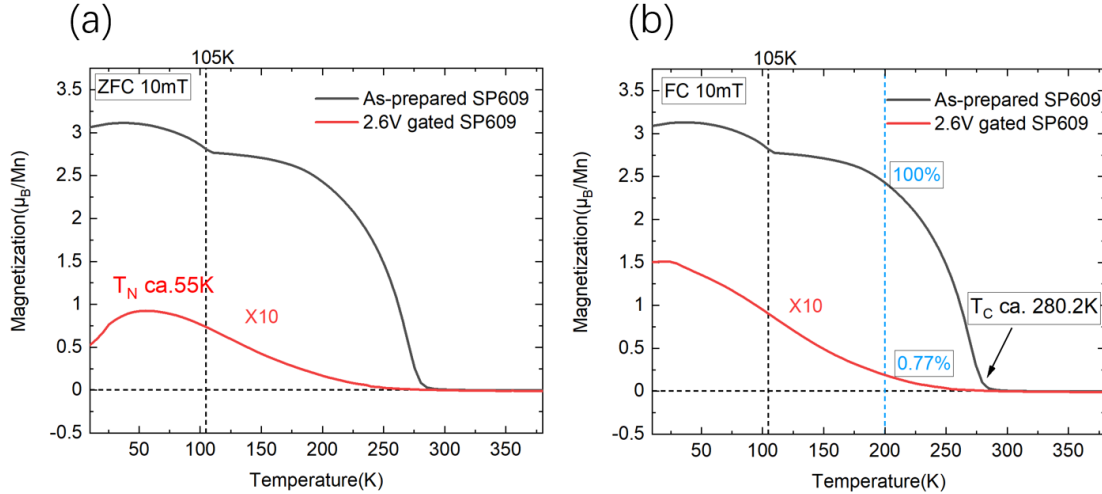

Figure 6.10 Magnetization vs. temperature curves of the as-prepared 100nm film SP609 (black curve) and after 2.6V gating (red curve), measured at 10mT. Panel (a) shows the ZFC curves. Panel (b) shows the corresponding FC curves. Data of the gated film is enhanced by a factor of 10 for a better comparation.

6.4 Changes of physical properties after ionic liquid gating on Fe₃O₄ thin films

6.4.1 Structural changes

In addition to the LSMO films, ILG is used for magnetite (Fe_3O_4) thin films. The sample information is shown in **Table 6.5**. Fe_3O_4 films were prepared by Yifan Xu using PLD at PGI-7. All Fe₃O₄ films were grown using the same growth parameters. The ILG time is fixed to 30min. The lattice structure is characterized by XRD. The results are shown in **Figure 6.11**. The sample D004 was gated first at 4V, then continued to be gated at 5V with the same polarity −. For samples D005 and D006, the gating polarity is changed to + and gated at 4V and 5V, respectively. The (004) peak of the as-prepared Fe_3O_4 film exhibits a weak intensity. By comparing the peak positions, one cannot see any obvious structural change for the −4V, +4V, −5V and +5V gated film. However, when assuming the structure is transformed either to wüstite ($Fe_{1-x}O$) or maghemite ($\gamma - Fe_2O_3$), the (004) peak of maghemite and the (002) peak of wüstite show a position near the (004) peak of magnetite. Hence, other methods are required to characterize the gated films e.g. SQUID magnetometry.

Table 6.5 Magnetite ILG parameters.

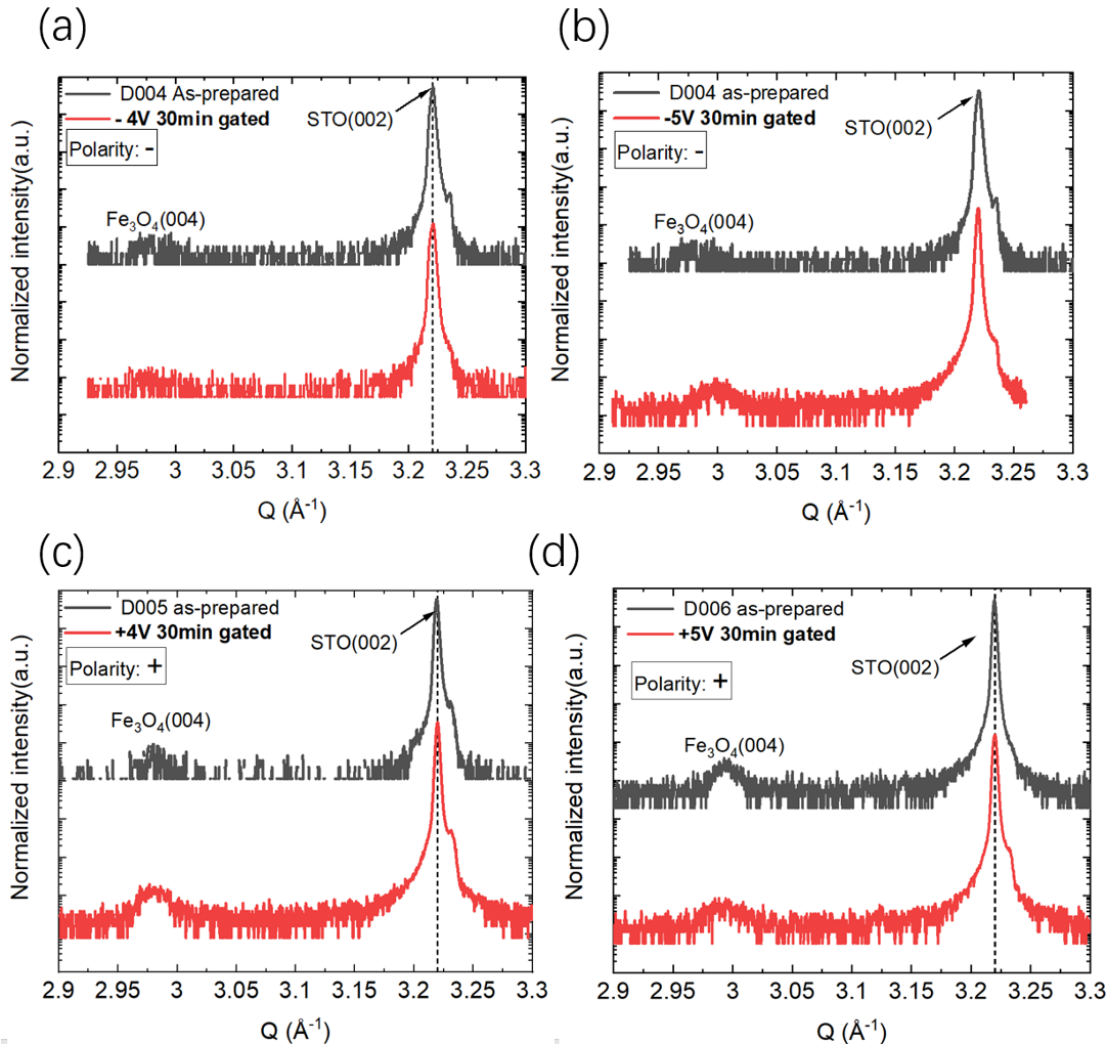| Sample ID	Growth temperature [°C]	Electrical polarity [±]	Gating configuration	Gating type	Gating voltage [volt]	Gating time [min]
D004	500	−	Type 1	Ex-situ	4	30
Gated D004	500	−	Type 1	Ex-situ	5	30
D005	500	+	Type 2	Ex-situ	4	30
D006	500	+	Type 2	Ex-situ	5	30

Figure 6.11 XRD pattern of magnetite films before and after gating i.e. D004, D005 and D006. (a) 4V 30min using polarity −.(b) 5V 30min using polarity −.(c) 4V 30min using polarity +.(d) 5V 30min using polarity +.

6.4.2 Changes of magnetic behavior

In order to explore the effect of gating onto the physical properties of the magnetite thin films in more detail, ZFC curves are measured at 50mT as shown in **Figure 6.12**. In **Figure 6.12 (a)**, the ZFC curves of the 4V gated film at either polarity + or − overlap with the curve of the as-prepared state. The film gated at 5V for both polarities show a reduced magnetization. The film gated at +5V demonstrates not only a magnetization reduction but a change of the curve shape as well. The +4V, -4V and -5V gated films share a similar curve shape as those from the as-prepared state.

Bulk magnetite shows a cubic to monoclinic phase transition and a metal to insulator phase transition at 125K (Verwey transition) [25,63]. This is accompanied by a rotation of the magnetic easy axis from the in-plane [110] direction to the out-of-plane [100] direction. Moreover, one finds a kink-like reduction of the magnetization with decreasing temperatures when measuring along the in-plane direction. One can determine the Verwey transition temperature T_V from the maximum of the $\partial M/\partial T$ curve or by the point where $\partial^2 M/\partial^2 T = 0$ as shown in **Figure 6.12 (b)**. The value of T_V can be influenced by the oxygen content and hence could be used for a magnetite stoichiometry characterization. For the as-prepared film, the reduced T_V of 112.9$\pm$1K compared with bulk system (125K) can be attributed to a substrate induced strain effect or a film off-stoichiometry. For the gated films, no obvious change of T_V is observed. Consequently, ILG cannot trigger a significant change of the magnetic properties with the present gating configuration.
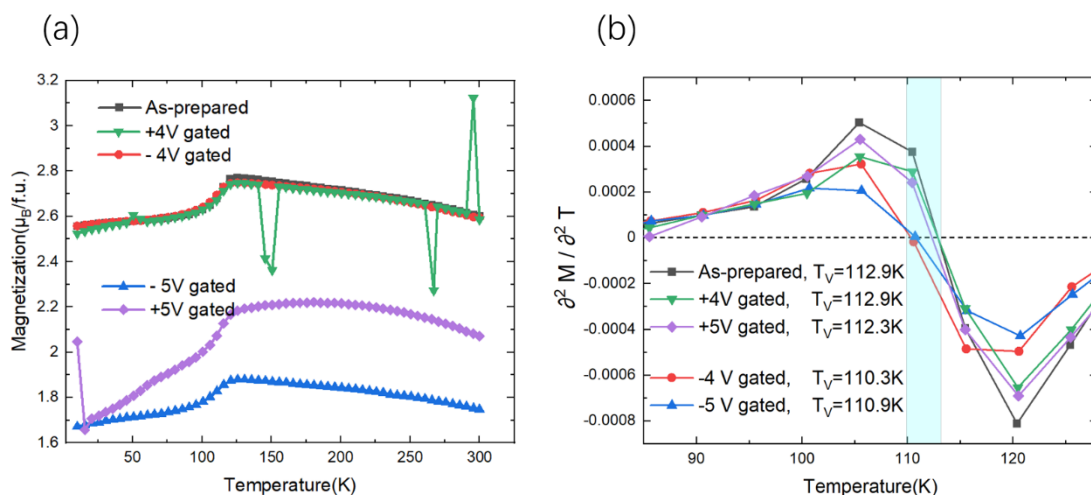

Figure 6.12 (a) Magnetization vs. temperature ZFC curve of the as-prepared and gated magnetite film, measured at 50mT. (b) Corresponding $\partial^2 M/\partial^2 T$ curves for the T_V determination.

6.5 Summary

In this chapter we demonstrate that the physical properties of LSMO films grown by HOPSD can be successfully tuned via ILG, i.e. the structural and magnetic properties. In XRD, the observed lattice expansion can be attributed to the increased Mn ion radius which could be triggered by the dual-ion transform as reported in the $SrCoO_3$ system [16]. The 2.8V and 3.2V gating experiments on 40nm films suggest that the transformation speed is enhanced at a higher

gating voltage. Moreover, a higher voltage also decreases the film homogeneity and thus leads to a plateau-like feature in the XRD scans. In XRR, the 33.5% and 21.8% SLD reduction of the 3.2V gated film implies a film decomposition effect via ILG. Using the type 2 configuration, as illustrated on a 100nm film, a large transformation speed at 2.6V as well as an improved film homogeneity is achieved. It suggests that this configuration can be used for future ILG studies and in particular for in-situ polarized neutron reflectometry. Additionally, the ca. 70% reduction of film thickness gives clear evidence for a decomposition effect during ILG.

Furthermore, using ILG we realized a ferromagnetic to antiferromagnetic phase transition on a 100nm LSMO film. The resulting antiferromagnetic behavior might be attributed to the superexchange interactions among Mn^{3+} or among Mn^{2+}. Either $V_O^{\cdot\cdot}$ or $H_i^{\cdot}$ in the film can lead to a reduction of the Mn oxidation state thus favoring superexchange interactions.

Compared with our previous studies based on insulating STO substrates, the conductive Nb-STO avoids the self-passivation effect and enables a more continuous film transformation. Moreover, the problem of the untransformed areas beneath the electrodes is solved thus enabling a better characterization via XRR and SQUID magnetometry.

However, according to the results of XRD and SQUID magnetometry measurements, ILG failed to exert an obvious effect on magnetite films at 4V and 5V gating voltages.

7. Summary and outlook

This thesis focuses on the tuning of the physical properties of LSMO film and powder samples via oxygen off-stoichiometry. For the 40nm film growth via HOSPD, we demonstrate that 800°C is the best growth temperature according to the highest T_C and the largest magnetization of the obtained films. Moreover, very thick, i.e. 200nm, films were successfully prepared.

Furthermore, we succeeded in triggering the PV to BM topotactical phase transition on LSMO 40nm and 200nm films via Al-assisted vacuum annealing. Compared to the previous study, the phase transition can be realized under more optimal conditions, i.e. at a lower temperature of 400°C for 12h and at 450°C for 12h, respectively. A clear E-PV to intermediate phase transition process is found from XRD studies which indicates an oxygen vacancy rearranging process. XAS

directly provides oxidation state information of Mn at various annealing states. By comparing these results with magnetometry data the different Néel-temperatures found on 40nm and 200nm films can be attributed to the superexchange interaction among Mn^{3+} and among Mn^{2+}, respectively. The obtained BM phase is found to show a new type of magnetic behavior as found from SQUID magnetometry rather than the previously reported antiferromagnetic behavior with a T_N of ca. 30K. A possible peak at ca. 400K in curves of magnetization vs. temperature implies a possible novel antiferromagnetic phase. The successful triggering of the PV-BM phase transition on 200nm films can enable a better signal for neutron diffraction studies for probing the spin structure of BM-LSMO films. However, in a brief attempt during a neutron diffraction beam time at IN12, Grenoble, only the nuclear film Bragg peaks could be detected. But this constitutes a (partial) success since previous attempts to perform neutron diffraction on similar thin films even did not reveal the nuclear Bragg peaks. As an outlook we will need to consider other methods, e.g. non-resonant high energy X-ray scattering.

LSMO powder with uniform particle size was achieved in this thesis by ball milling. Al-assisted vacuum annealing is found to also be able to trigger the PV-BM phase transition on powder samples at 550°C for 20h. The BM-LSMO powder shows a typical antiferromagnetic behavior with a T_N of ca. 55K. In the near future, a neutron diffraction experiment is planned to probe the spin structure of the antiferromagnetic BM-LSMO phase on powder samples.

Additionally, ILG is employed using a self-designed reaction cell for LSMO films. The previously found self-passivation effect is relieved when using conductive Nb-STO substrates. This allows films to be continuously transformed from the as-prepared state to E-PV state. We demonstrate that a significant lattice expansion can be triggered in a short time i.e. 1 hour. A higher transformation speed can be employed when increasing the gating voltage. However, this is accompanied by a lower film homogeneity and a starting film decomposition. Additionally, we improved the ILG efficiency via a refined gating configuration and realized a ferromagnetic to antiferromagnetic transition on a 100nm film.

References

1. Waser, R., et al., Redox-Based Resistive Switching Memories-Nanoionic Mechanisms, Prospects, and Challenges. Advanced Materials, 2009.**21**(25-26): p.2632-2663.

2. Tong, B., et al., Oxygen Vacancy Defects Boosted High Performance p-Type Delafossite $CuCrO_2$ Gas Sensors. ACS Applied Materials and Interfaces, 2008.**10**(40): p.34727-34734.

3. Wang, X., et al., Oxygen vacancy defects engineering on Ce-doped $\alpha - Fe_2O_3$ gas sensor for reducing gases, Sensors and Actuators B: Chemical, 2019.**302**: p.127165.

4. Sinha, L., Shirage, P., Surface Oxygen Vacancy Formulated Energy Storage Application: Pseudocapacitor-Battery Trait of $W_{18}O_{49}$ Nanorods. Journal of The Electrochemical Society, 2019.**166**(14): p.A3496-A3503.

5. Wang, L., et al., Oxygen exchange kinetics on solid oxide fuel cell cathode materials-general trends and their mechanistic interpretation. Journal of Materials Research, 2012.**27**(15): p.2000-2008.

6. Muñoz-García, A. B., et al., Oxygen transport in perovskite-type solid oxide fuel cell materials: Insights from quantum mechanics. Accounts of Chemical Research, 2014.**47**(11): p.3340-3348.

7. Kobayashi, S., et al., Quantitative analyses of oxidation states for cubic $SrMnO_3$ and orthorhombic $SrMnO_{2.5}$ with electron energy loss spectroscopy. Journal of Applied Physics, 2010.**108**(12): p.124903.

8. Shahee, A., et al., Effect of oxygen off-stoichiometry on coupled structural and magnetic phase-transitions in $La_{0.15}Sr_{0.85}MnO_{3-\delta}$ (δ=0.02, 0.14). Solid State Communications, 2014.**177**: p.84-88.

9. Schumacher, D., et al., Inducing exchange bias in $La_{0.67}Sr_{0.33}MnO_{3-\delta}/SrTiO_3$ thin films by strain and oxygen deficiency. Physical Review B, 2013.**88**(14): p.144427.

10. Cao, L., Petracic, O., Zakalek, P., et al., Reversible Control of Physical Properties via an Oxygen-Vacancy-Driven Topotactic Transition in Epitaxial $La_{0.7}Sr_{0.3}MnO_{3-\delta}$ Thin Films.

Advanced Materials, 2019.**31**(7): p.1806183.

11. Cao, L., Controlling structural and physical properties of epitaxial transition metal oxide films through oxygen stoichiometry. PhD thesis, 2019, Forschungszentrum Jülich GmbH, RWTH Aachen.

12. Zhang, H., Influence of oxygen stoichiometry onto physical properties of $La_{0.7}Sr_{0.3}MnO_{3-\delta}$ powder and thin films. Master thesis, 2020, Forschungszentrum Jülich GmbH, RWTH Aachen.

13. Manca, N., Pellegrino, L., Marré, D., Reversible oxygen vacancies doping in $(La_{0.7}, Sr_{0.3})MnO_3$ microbridges by combined self-heating and electromigration. Applied Physics Letters, 2015.**106**(20): p.1-5.

14. Ge, C., et al., Metal-Insulator Transition Induced by Oxygen Vacancies from Electrochemical Reaction in Ionic Liquid-Gated Manganite Films. Advanced Materials Interfaces, 2015.**2**(17): p.1-6.

15. Lee, T. K., Jung, J. H., Irreversible Change of Electric Conduction in Ionic-Liquid-Gated $(La,Sr)MnO_3$ Thin Films. Journal of the Korean Physical Society, 2016.**69**(7): p.1263–1266.

16. Lu, N., et al., Electric-field control of tri-state phase transformation with a selective dual-ion switch. Nature, 2017.**546**(7656): p.124-128.

17. Tilley, R.J.D., Perovskites: Structure-Property Relationships. 2016: John Wiley & Sons.

18. Tan, H. T., Sun, W., et al., 2D Transition Metal Oxides/Hydroxides for Energy-Storage Applications. ChemNanoMat, 2016.**2(**7): p.562-577.

19. Kalinin, S. V., Spaldin, N. A., Functional Ion Defects in Transition Metal Oxides. Science, 2013.**341**(6148): p.858-859.

20. Meyer, J., et al., Transition Metal Oxides for Organic Electronics: Energetics, Device Physics and Applications. Advanced Materials, 2012.**24**(40): p.5408-5427.

21. Hemberger, J., et al., Structural, magnetic, and electrical properties of single-crystalline $La_{1-x}Sr_xMnO_3$ ($0.4 < x < 0.85$). Physical Review B, 2002.**66**(9): p.1-8.

22. Paraskevopoulos, M., et al., Magnetic properties and the phase diagram of $La_{1-x}Sr_xMnO_3$ for $x \leq 0.2$. J. Phys.: Condens. Matter, 2000.**12**: p.3993-4011.

23. Endoh, Y., et al., Transition between Two Ferromagnetic States Driven by Orbital Ordering in $La_{0.88}Sr_{0.12}MnO_3$. Physical Review Letter, 1999.**82**(21): p.4328-4331.

24. Moritomo, Y., et al., Antiferromagnetic metallic state in the heavily doped region of perovskite manganites. Physical Review B, 1998.**58**(9): p.5544-5549.

25. Mai Hussein Abdalla Hamed, Interface Functionalization of Magnetic Oxide $Fe_3O_4/SrTiO_3$ Heterostructures. PhD thesis, 2021, Forschungszentrum Jülich GmbH.

26. Blundell, S., et al., Magnetism in condensed matter. 2001: Oxford University Press.

27. Woodward, P. M., et al., Influence of Cation Size on the Structural Features of $Ln_{1/2}A1_{1/2}MnO_3$ Perovskites at Room Temperature. Chemistry of Materials, 1998.**10**(11): p.3652-3665.

28. Stokes, H. T., Howard, C. J., Group-Theoretical Analysis of Octahedral Tilting in Perovskites. Acta Crystallographica Section B, 1998.**54**: p.782-789.

29. Reichelt, K., Nucleation and growth of thin films. Vacuum, 1988. **38**(12): p.1083-1099.

30. Venables, J.A., Atomic processes in crystal growth. Surface Science, 1994. **299-300**: p. 798-817.

31. Angst, M., et al., Scattering! Soft, Functional and Quantum Materials. 50th IFF Spring School. 2019, Forschungszentrum Jülich GmbH.

32. Brückel, T., et al., Neutron Scattering. Laboratory Course, 2015: Forschungszentrum Jülich GmbH.

33. Faley, M., et al., High oxygen pressure deposition and patterning methods for metal oxide heterostructures. Poster, 2012, Forschungszentrum Jülich GmbH.

34. Waschk, M., Interface phenomena in $La_{1/3}Sr_{2/3}FeO_3/La_{2/3}Sr_{1/3}MnO_3$ heterostructures and a quest for p-electron magnetism. PhD Thesis, 2017, Forschungszentrum Jülich GmbH, RWTH Aachen.

35. Schmitz, M., Strain and electric field mediated manipulation of magnetism in $La_{(1-x)}Sr_xMnO_3/BaTiO_3$ heterostructures. PhD Thesis, 2015, Forschungszentrum Jülich GmbH, RWTH Aachen.

36. Wang, W., GAN CHARACTRIZATION BY X-RAY TECHNIQUES. Master thesis, 2015, University of Houston.

37. Voigtländer, B., et al., Scanning Probe Microscopy. 2015: Springer.

38. Lagar, J. H., Raborar, M. G. C., Material contrast identification and compositional contrast mapping using backscattered electron imaging. Proceedings of the 20th IEEE International Symposium on the Physical and Failure Analysis of Integrated Circuits (IPFA), 2013: p. 464-469.

39. Zakalek, P., Magnetic Interface Effects in Thin Film Heterostructures. PhD Thesis, 2015, Forschungszentrum Jülich GmbH, RWTH Aachen.

40. Koon, D. W., Knickerbocker, C. J., What do you measure when you measure resistivity? Review of Scientific Instruments, 1992.**63**(1): p.207-210.

41. Quantum Design, Physical Property Measurement System: User's Manual (Quantum Design, Inc., San Diego, CA, 2002).

42. Mayer, M., Rutherford Backscattering Spectrometry (RBS). Lectures, 2003, Max-Planck-Institut für Plasmaphysik, EURATOM Association, Garching, Germany.

43. De Groot, F. M. F., X-ray absorption and dichroism of transition metals and their compounds. Journal of Electron Spectroscopy and Related Phenomena, 1994.**67**: p.529-626.

44. Thole, B. T., van der Laan, G., Branching ratio in x-ray absorption spectroscopy. Physical Review B, 1998.**38**(5): p.3158-3171.

45. Li, Q., et al., Quantitative probe of the transition metal redox in battery electrodes through soft x-ray absorption spectroscopy. Journal of Physics D, 2016.**49**(41): p.413003.

46. Qiao, R., et al., Spectroscopic fingerprints of valence and spin states in manganese oxides and fluorides. Current Applied Physics, 2013.**13**(3): p.544-548.

47. Frati, F., Hunault, M., de Groot, F., Oxygen K-edge X-ray Absorption Spectra. Chemical Reviews, 2020.**120**(9): p.4056-4110.

48. Deng, J., Large lattice mismatch effects on the epitaxial growth and magnetic properties of FePt films. Journal of Magnetism and Magnetic Materials, 2018.**446**: p.125-134.

49. Adamo, C., Enhanced electrical and magnetic properties in $La_{0.7}Sr_{0.3}MnO_3$ thin films deposited on $CaTiO_3$-buffered silicon substrates. APL Materials, 2015.**3**(6): p.062504.

50. Eckstei, W., Sputtering Yields. 2007: Springer.

51. Nishimura, T., et al., Structure change of TiO_2-terminated $SrTiO_3$ (001) surfaces by annealing in O_2 atmosphere and ultrahigh vacuum. Surface Science, 1999.**421**: p.273-278.

52. Zhang, H., Influence of oxygen stoichiometry onto physical properties of complex oxide thin films. Project thesis, 2020, Forschungszentrum Jülich GmbH, RWTH Aachen.

53. Gulbransen, E. A., Wysong, W. S., Thin Oxide Films on Aluminum. J. Phys. Chem., 1947.**51**(5): p.1087-1103.

54. Smeltzer, W. W., Oxidation of Aluminum in the Temperature Range 400°-600°C. Journal of The Electrochemical Society, 1956.**103**(4): p.209-214.

55. Börgers, J. M., et al., Faster Diffusion of Oxygen Along Dislocations in $(La,Sr)MnO_{3+\delta}$ Is a Space-Charge Phenomenon. Advanced Functional Materials, 2021.**31**(51): 2105647.

56. Cao, L., et al., Migration Kinetics of Surface Ions in Oxygen-Deficient Perovskite During Topotactic Transitions. Small, 2021.**17**(51): p.2104356.

57. Meyer, R., Szot, K., Waser, R., Restructuring the surface region of donor doped $SrTiO_3$ single crystals under oxidizing conditions. Ferroelectrics, 1999.**224**(1): p.323-329.

58. Cao, L., et al., Metal–Insulator Transition via Ion Irradiation in Epitaxial $La_{0.7}Sr_{0.3}MnO_{3-\delta}$ Thin Films. Physica Status Solidi - Rapid Research Letters, 2021.**15**(11): p.1-5.

59. Wang, Y., et al., Ionic Liquid Gating and Phase Transition Induced Semiconducting to Metallic Transition in $La_{0.67}Sr_{0.33}MnO_3/BaTiO_3$ Heterostructures. ACS Applied Materials and Interfaces, 2020.**12**(38): p.43257-43265.

60. Zhao, S., et al., Quantitative Determination on Ionic-Liquid-Gating Control of Interfacial Magnetism. Advanced Materials, 2017.**29**(17): p.1606478.

61. Herklotz, A., et al., Reversible Control of Interfacial Magnetism through Ionic-Liquid-Assisted Polarization Switching. Nano Letters, 2017.**17**(3): p.1665-1669.

62. Mefford, J. T., et al., Anion charge storage through oxygen intercalation in $LaMnO_3$ perovskite pseudocapacitor electrodes. Nature Materials, 2014.**13**(7): p.726-732.

63. Iizumi, M., et al., Structure of magnetite (Fe_3O_4) below the Verwey transition temperature. Acta Cryst.B, 1982.**38**: p.2121-2133.

Acknowledgements

List of Abbreviations

AFM	Antiferromagnetic
AFM	Atomic Force Microscopy
BM	Brownmillerite
CID	Charge-Injection-Device
CVD	Chemical Vapor Deposition
EDL	Electric Double Layer
EDX	Energy-Dispersive X-ray spectroscopy
E-PV	Expanded Perovskite phase
FC	Field Cooling
FM	Ferromagnetic
HBM	Hydrogenated Brownmillerite
HOPSD	High Oxygen Pressure Sputter Deposition
I	Insulating
ICP-OES	Inductively Coupled Plasma Optical Emission Spectroscopy
ILG	Ionic Liquid Gating
LSAT	$(LaAlO_3)_{0.3}(Sr_2AlTaO_6)_{0.7}$
LSMO	$La_{0.7}Sr_{0.3}MnO_{3-\delta}$
M	Metallic
MBE	Molecular-Beam Epitaxy
MFC	Mass Flow Controller
Nb-STO	Nb-doped $SrTiO_3$
ND	Neutron Diffraction
O	Octahedron
O$_h$	Octahedral site
PA	Paramagnetic
PLD	Pulsed Laser Deposition
PPMS	Physical Properties Measurement System
PV	Perovskite
PVD	Physical Vapor Deposition
RBS	Rutherford Backscattering Spectrometry
RF	Radio Frequency
RSM	Reciprocal Space Mapping
SEM	Scanning Electron Microscopy
SLD	Scattering Length Density

STO	$SrTiO_3$
SQUID	Superconducting Quantum Interference Device
T	Tetrahedron
T$_d$	Tetrahedral site
XRD	X-ray Diffraction
XRR	X-ray Reflectivity
ZFC	Zero-Field Cooling
VSM	Vibrating-Sample Magnetometer
XAS	X-ray Absorption Spectroscopy
XPS	X-ray Photoelectron Spectroscopy